Technical Physics Letters, Vol. 28, No. 8, 2002, pp. 621–624. Translated from Pis'ma v Zhurnal Tekhnicheskoĭ Fiziki, Vol. 28, No. 15, 2002, pp. 1–9.
Original Russian Text Copyright © 2002 by Kudryavtsev, Tsendin.

Cathode Boundary Conditions for Fluid Model Discharges on the Right-Hand Branch of the Paschen Curve

A. A. Kudryavtsev[a],* and L. D. Tsendin[b]
[a] *St. Petersburg State University, St. Petersburg, Russia*
** e-mail: akud@ak2138.spb.edu*
[b] *St. Petersburg State Technical University, St. Petersburg, Russia*

Received February 7, 2002

Abstract—It is shown that a fluid description of discharges on the right-hand branch of the Paschen curve must take into account a change in the effective secondary emission coefficient γ_{eff} of the cathode, which is related to the electron backscattering effect. Simple kinetic expressions for γ_{eff} are obtained which indicate that the effective secondary emission is determined by the initial energy of emitted electrons and by the applied field amplitude. *© 2002 MAIK "Nauka/Interperiodica".*

Breakdowns corresponding to the right-hand branch of the Paschen curve ($pd > 1$–5 Torr cm) take place at low field strengths and are characterized by strong exponential field dependence $\alpha/p = Ae^{-Bp/E}$. In this regime, electrons are in equilibrium with the external field and the ionization can be characterized by the Townsend coefficient $\alpha(E/p)$ dependent on the local field strength. Such systems can be described within the framework of a fluid model according to which the electron ensemble is replaced by an average electron possessing a mean energy of $3T_e/2$, a drift velocity of $V_{ed} = b_eE$, and a diffusion coefficient of $D_e = b_eT_e/e$.

The fluid model (and various combinations with other approaches, called hybrid models) are frequently employed for modeling transient discharges (e.g., in PDPs—plasma display panels), in which the applied voltage drops after breakdown and the local approximation remains valid during the whole discharge process (see, e.g., [1–8]). The cathode boundary condition is usually taken in the form of the Townsend relation between the electron and ion currents,

$$j_e(0, t) = \gamma_{\mathrm{eff}} j_i(0, t), \tag{1}$$

where γ_{eff} is the second Townsend coefficient reflecting the contributions of various processes to the secondary electron emission from the cathode.

The quantities entering into relation (1) cannot be calculated within the framework of the fluid model and have to be determined from a microscopic theory. Otherwise, the values of γ_{eff} must be determined from experimental data for each particular system of gas and electrode material. Since the coefficient γ_{eff} depends rather strongly on the parameter E/p, this dependence has to be taken into account in the description of nonstationary discharges. This approach is most consistently developed by Phelps and Petrovic in [9], where the γ_{eff} values (called the apparent secondary electron emission coefficient) for Ar are determined and tabulated based on a thorough analysis of experimental results.

In order to theoretically determine a relation between the apparent coefficient γ_{eff} entering into the boundary condition (1) and the "true" coefficient γ characterizing the process of electron emission from a cathode surface, it is necessary to solve a kinetic problem. It was demonstrated in the early work by Thomson [10] that, if the boundary condition for $j_e(0, t)$ is selected in the form $j_e(0, t) = n_eV_{ed} + n_eV/4$ with V representing the chaotic velocity of electrons (this form was also employed in [1–5], the electron escape factor f_{es} in the relation $\gamma_{\mathrm{eff}} = f_{es}\gamma$ is

$$f_{es} = 1/(1 + V/4V_{ed}) = 1/(1 + 3\lambda_T/2\lambda). \tag{2}$$

Here, $\lambda_T = T_e/eE$ is a characteristic distance for establishing the electron drift velocity (or the electron energy relaxation pathlength [11]). As can be seen, for $V_{ed} \ll V$, most of the emitted electrons will return to the cathode, this fraction being dependent on the parameter E/p.

The problem was most thoroughly considered in [12, 13] using kinetic equations written in the same form (see Eq. (9) below) based on a nonlocal approximation [11] (see [12, Eq. (2)] and [13, Eq. (12)]). Once the cross sections of nonelastic processes with the threshold ε^* were also described in [12, 13] using the same linear approximation, the resulting formulas (see [12, Eq. (6)] and [13, Eq. (24)]) are fully identical. Taking into account that the initial energies ε_e of emitted electrons are usually low (on the order of several electronvolts), the analysis in [12, 13] was restricted to the case of $\varepsilon_e \ll \varepsilon^*$. The fraction of fast electrons with $\varepsilon > \varepsilon^*$ under these conditions is small. However, expressions for the electron energy distribution function (EDF) in this energy range are rather complicated. As a result, even the case of a monoenergetic electron source leads to rather cumbersome final expressions [12, 13] which are difficult to interpret, although the contribution of this EDF part can be significant only for a gas mixture containing a small additive of a readily ionizable component.

In this communication, we report on simple kinetic expressions obtained for γ_{eff} on the right-hand branch of the Paschen curve, which generalize the results obtained in [12, 13] and simplify their interpretation. It is shown that attempts at calculating γ_{eff} within the framework of a fluid approach (fluid model) are unpromising.

Indeed, within the framework of the fluid approximation, the continuity equation for the electron emission in a slowly varying field has the form

$$D_e n_e'' - V_{ed} n_e' + \nu_i n_e = 0, \tag{3}$$

where the first term takes into account the diffusion of electrons, since the role of this factor near the cathode can be significant [10]. Denoting the characteristic parameters by $\lambda_T = T_e/eE$ and $\alpha = \nu_i/V_{ed}$, a solution to Eq. (3) for a nonzero boundary electron density $n_e(0) = n_{e0}$ can be written as follows:

$$\begin{gathered} n_e(x) = n_{e0}\exp(x/2\lambda_T) \\ \times \sinh\left((L-x)\sqrt{1-4\alpha\lambda_T}/2\lambda_T\right)/\sinh\left(L\sqrt{1-4\alpha\lambda_T}/2\lambda_T\right). \end{gathered} \tag{4}$$

Taking into account that the gap L is several times greater than the ionization length α^{-1} and that $\alpha\lambda_T \ll 1$ on the right-hand branch of the Paschen curve, we expand expression (4) into series in this small parameter and obtain the well-known Townsend law

$$n_e(x) = n_{e0}\exp(\alpha x), \quad j_e(x) = j_{e0}\exp(\alpha x). \tag{5}$$

Accordingly, the resulting electron flux from the cathode,

$$\begin{aligned} j_{e0} &= j_e(0) = -D_e n_e' + V_{ed} n_e \\ &= -V_{ed}\alpha\lambda_T n_{e0} + V_{ed} n_{e0} \approx V_{ed} n_{e0}, \end{aligned} \tag{6}$$

is determined predominantly by the electron drift component. In other words, the role of diffusion for $L \gg \lambda_T$ is relatively small and an allowance for this factor does not significantly modify the classical Townsend formula (5) for the electron current density in the discharge gap.

The simplest way of taking into account the kinetic character of the problem is the well-known mean free path approximation [14]. According to this, the electron flux is described as the difference $j_e(0) = j_{e+}(0) - j_{e-}(0)$ of the partial fluxes directed from (+) and toward (–) the cathode (see, e.g. [14]):

$$\begin{aligned} j_{e+}(0) &= \frac{n_{e0}V}{4} + \left(\frac{-D_e n_e'}{2} + V_{ed} n_e\right), \\ j_{e-}(0) &= \frac{n_{e0}V}{4} - \frac{-D_e n_e'}{2}. \end{aligned} \tag{7}$$

The boundary condition on the cathode is determined as

$$j_{e+}(0) = j_{e0} = \gamma j_i(0). \tag{8}$$

Substituting formulas (4)–(6) into this relation, we obtain the escape factor f_{es} in the form (2) coinciding with the expression derived by Thompson [10]. Within the framework of this approximation, attempts at further refining the boundary conditions [15, 16] seem to be unpromising.

Since the fluid model proper (including the concept of V_{ed}) is applicable only for distances of $x > \lambda_T$ from the discharge gap boundary, a more consistent kinetic analysis should be conducted in order to describe in more detail the dynamics of development of the flux of electrons drifting from the cathode. Below we present a simple and physically clear description of this process based on an approach developed previously [11].

A kinetic equation for the isotropic part of the EDF in terms of the coordinate x and total electron energy $\varepsilon = mV^2/2 - eEx$ for an inelastic energy balance in the electric field ($eE\lambda > \varepsilon_1\sqrt{2m/M}$) takes the following form [11]:

$$\begin{gathered} \frac{\partial}{\partial x}\left(\frac{(\varepsilon + eEx)}{3N\sigma(\varepsilon + eEx)}\frac{\partial f_0(\varepsilon, x)}{\partial x}\right) \\ = N\sigma^*(\varepsilon + eEx) f_0(\varepsilon, x)(\varepsilon + eEx). \end{gathered} \tag{9}$$

Here, σ and σ^* are the elastic and inelastic scattering cross sections, respectively, which are functions of the kinetic energy $w = \varepsilon + eEx$; $\lambda = 1/N\sigma$ is the electron mean free path.

The character of the motion of electrons with the initial velocity ε is illustrated in the figure. For $\varepsilon < \varepsilon^*$, the kinetic energy of electrons within a distance of $x_1(\varepsilon) = (\varepsilon^* - \varepsilon)/eE$ is below ε^* and the particles move with conservation of the total energy ε. Since $\sigma^* = 0$, the differential flux

$$\begin{aligned} \Phi(\varepsilon) &= \frac{2(\varepsilon + eEx)}{3m} f_1(\varepsilon, x) \\ &= \frac{2(\varepsilon + eEx)}{3mN\sigma(\varepsilon + eEx)}\frac{\partial f_0(\varepsilon, x)}{\partial x} \end{aligned} \tag{10}$$

is conserved as well. In the region of $x > x_1(\varepsilon)$, the electrons undergo inelastic collisions which result in an abrupt loss of the excitation energy ε^* with jumping down to the lower energy step $\varepsilon = -eEx$ (see figure). Only these electrons are then "picked up" by the field and carried toward the anode, rather than returned to the cathode (in contrast to electrons in the upper half-plane $\varepsilon > 0$, which return to the cathode). Under the conditions of applicability of the two-term EDF expansion ($\sigma \gg \sigma^*$), the characteristic spatial ($\lambda_\varepsilon^* = \sqrt{\lambda\lambda^*/3}$) and energy ($T^* = eE\lambda_\varepsilon^*$) scales of the EDF decay for $\varepsilon > \varepsilon^*$ are small as compared to $\lambda_\varepsilon = \varepsilon_1/eE$ and ε_1, respectively. For this reason, the EDF (exhibiting a sharp decay above the threshold ε^*) can be determined using the so-called "black wall" model. According to this, a zero boundary condition is imposed at an energy of $\varepsilon^* + T^*$ corresponding to the distance $x_1(\varepsilon) + \lambda_\varepsilon^*$ (see figure) [11].

The solution (9) can be represented as

$$f_0(\varepsilon, x)/\int\limits_x^{x_1(\varepsilon)} \frac{\sigma(\varepsilon + Ex)dx}{(\varepsilon + Ex)} = f_0(\varepsilon, 0)/\int\limits_0^{x_1(\varepsilon)} \frac{\sigma(\varepsilon + eEx)dx}{(\varepsilon + eEx)} = \Phi(\varepsilon), \tag{11}$$

where $x_1(\varepsilon) = (\varepsilon^* + T^* - \varepsilon)/eE = \lambda_\varepsilon + \lambda_\varepsilon^* - \varepsilon/eE$. As noted above, since $\lambda_\varepsilon \gg \lambda_\varepsilon^*$, the contribution of fast electrons with $\varepsilon > \varepsilon^*$ both to the current and to the density is small (being on the order of $\lambda_\varepsilon^*/\lambda_\varepsilon \ll 1$). According to the Marshak conditions [17] for the EDF at the wall (cf. Eq. (7)),

$$j_+ = f_0/4 + f_1/2, \quad j_- = f_0/4 - f_1/2, \tag{12}$$

we obtain the following boundary condition on the cathode (cf. Eq. (8)):

$$j_+(\varepsilon, 0) = j_0(\varepsilon), \tag{13}$$

where $j_0(\varepsilon)$ is the flux of electrons emitted from the cathode.

Substituting the EDF (10) into formulas (12), we obtain an expression for the partial (i.e., corresponding to a monoenergetic electron sources on the cathode) escape factor $f_{es}(\varepsilon)$:

$$\frac{1}{f_{es}(\varepsilon)} = \frac{\gamma(\varepsilon)}{\gamma_{eff}(\varepsilon)} = \frac{1}{2} + \frac{\varepsilon}{4}\int\limits_0^{x_1(\varepsilon)} \frac{N\sigma(\varepsilon + eEx)dx}{(\varepsilon + eEx)}. \tag{14}$$

The solution acquires the simplest form when the integrand is such that $2(\varepsilon + eEx)/mN\sigma(\varepsilon + eEx) \approx \text{const}$, which is approximately valid for the Ramsauer gases (Ar, Kr, Xe). In this case, Eq. (11) yields an EDF linearly decreasing along the coordinate,

$$f_0(\varepsilon, x) = f_0(\varepsilon, 0)(1 - eEx/(\varepsilon^* + T^* - \varepsilon)), \tag{15}$$

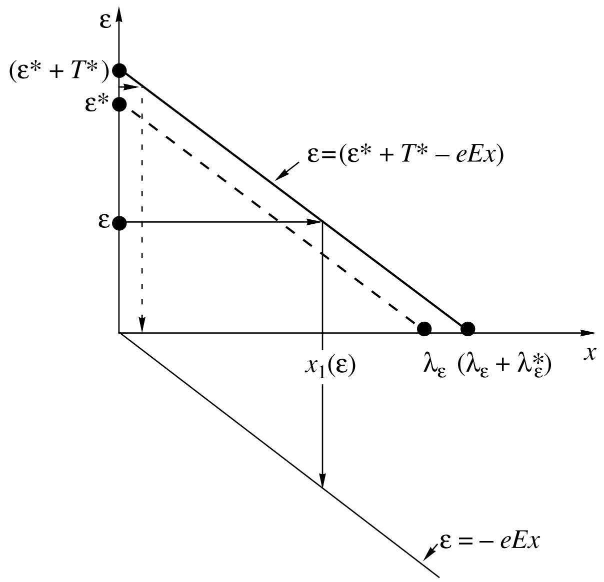

Figure.

while f_{es} determined from relation (14) coincides with that given by expression (2) with $\lambda_T = x_1(\varepsilon) = \lambda_\varepsilon + \lambda_\varepsilon^* - \varepsilon/eE$.

Using Eqs. (12)–(14), one can readily derive a general expression for f_{es} valid in the case of arbitrary source energy dependence $f_0(\varepsilon, 0)$ and elastic collision frequencies $\sigma(\varepsilon + eEx)$:

$$\frac{1}{f_{es}} = \frac{\gamma}{\gamma_{eff}} = \frac{1}{2} + \frac{\int\limits_0^{\varepsilon_1 + T^*} f_0(\varepsilon, 0)\sqrt{\varepsilon}d\varepsilon}{4\int\limits_0^{\varepsilon_1 + T^*} \dfrac{f_0(\varepsilon, 0)d\varepsilon}{\sqrt{\varepsilon}\int\limits_0^{x_1(\varepsilon)} \dfrac{N\sigma(\varepsilon + eEx)dx}{(\varepsilon + eEx)}}}. \tag{16}$$

This expression can be recommended for calculating $\gamma_{eff}(E/p)$ from the known true coefficient γ.

As a rule, the $f_0(\varepsilon, 0)$ values for emitted electrons are more or less constant in the energy interval from 0 to ε_e, where $\varepsilon_e = \varepsilon_i - 2e\varphi$ (for the potential ion-induced emission) or $\varepsilon_e = \varepsilon^* - e\varphi$ (for the emission induced by metastable atoms), ε_i being the ionization potential and $e\varphi$, the electron work function [16]. In this case, expression (16) can be simplified by assuming that $f_0(\varepsilon, 0)$ is energy-independent for $\varepsilon \le \varepsilon_e$, that is, $f_0(\varepsilon, 0) = 3n_{e0}/2\varepsilon_e^{3/2} = \text{const}$.

In a single-component medium, we have $\varepsilon_e < \varepsilon^*$ and, hence, f_{es} from (16) approximately coincides with (2) for $\lambda_T \approx \lambda_\varepsilon$. In particular, for $f_0(\varepsilon, 0) = 3n_{e0}/2\varepsilon_e^{3/2} = \text{const}$ and $2(\varepsilon + eEx)/mN\sigma(\varepsilon + eEx) \approx \text{const}$, expression (16) yields (2) with $\lambda_T \approx \varepsilon_e^2/(6eE\varepsilon_1 \ln((\sqrt{\varepsilon^*} + \sqrt{\varepsilon_e})/(\sqrt{\varepsilon^*} - \sqrt{\varepsilon_e})) \approx \lambda_\varepsilon$. In the case of gas mixtures with significantly different ε_i values and cathodes with small $e\varphi$ (e.g., He, Ne + Xe with MgO cathodes used in PDPs [1–10]), we can expect that $\varepsilon_e > \varepsilon^*$. Indeed, for the secondary electron emission induced by ions and metastable atoms of He or Ne with ε_i(He) = 24.6 eV and ε_i(Ne) = 21.6 eV, the energy ε_e will exceed the excitation threshold for Xe (ε^* = 8.3 eV). Therefore, a part of the emitted electrons with the energies $\varepsilon_e - \varepsilon^*$ will contribute to escape factor (2) with length λ_T represented by $\lambda_\varepsilon^* < \lambda_\varepsilon$ (the trajectory of such electrons in the phase plane (ε, x) is depicted by the dashed line in the figure) rather than by λ_ε. This is probably one of the factors explaining improvement of the discharge characteristics in PDP cells employing Xe mixtures with He, Ne buffers.

Thus, most of the emitted electrons with $\lambda_\varepsilon \gg \lambda$ will return to the cathode and the effective secondary emission coefficient will decrease. In order to render γ_{eff} sufficiently close to the true γ value, we must formally obey the condition $\lambda_\varepsilon - \varepsilon^*/eE \approx 1$. This implies that the electric field must be sufficiently strong to impart electrons an energy on the order of ε^* within a distance about one mean free path length. In this case, the “black wall” approximation used above fails to be valid, the inelastic processes can be treated as quasi-elastic, and the EDF decay at $\varepsilon > \varepsilon^*$ is formally determined by the value of $T_h^* = T^*\lambda_\varepsilon^*/\lambda_\varepsilon$ rather than by T^*. Unfortunately, under these conditions, the above considerations based on the two-term EDF expansion, as well as the concept of the local coefficient $\alpha(E/p)$, become inapplicable. Such fields correspond to saturation of the exponential dependence of $\alpha(E/p)$ and the transition to conditions of the left-hand branch of the Paschen curve. In order to be picked up by the field and carried toward the anode on the right-hand branch of the Paschen curve, an electron must travel a distance of $x_1(\varepsilon_e) \approx (\varepsilon^* + T^* - \varepsilon_e)/eE = \lambda_\varepsilon + \lambda_\varepsilon^* - \varepsilon_e/eE$. For electrons with small initial energies ε_e, this distance amounts to $x_1 \approx \lambda_\varepsilon + \lambda_\varepsilon^*$, whereas for large energies $\varepsilon_e \approx \varepsilon^*$, $x_1 \approx \lambda_\varepsilon^* \ll \lambda_\varepsilon$. Therefore, an increase in γ_{eff} at a given E/p in this case can be provided only by increasing the initial energy ε_e of the emitted electrons.

Thus, it has been established that a fluid model of discharge on the right-hand branch of the Paschen curve must take into account a change in the effective secondary emission coefficient γ_{eff} of the cathode, which is related to the electron backscattering effect. The γ_{eff} value depends predominantly on the initial energy of emitted electrons and on the applied field amplitude.

Acknowledgments. One of the authors (L.D.Ts.) is grateful for support from the Russian Foundation for Basic Research (project no. 01-02-16874) and NATO (grant SfR 974354).

REFERENCES

1. J. Meunier, Ph. Belenguer, and J. P. Boeuf, J. Appl. Phys. **78**, 731 (1995).
2. J. P. Boeuf, C. Punset, A. Hirech, and H. Doyeux, J. Phys. IV **7**, C4-3 (1997).
3. R. Veerasingam, R. B. Campbell, and R. T. McGrath, Plasma Sources Sci. Technol. **6**, 157 (1997).
4. H. S. Jeong, B. J. Shin, and K. W. Whang, IEEE Trans. Plasma Sci. **27**, 171 (1999).
5. S. Rauf and M. J. Kushner, J. Appl. Phys. **85**, 3460 (1999).
6. Y. K. Shin, C. H. Shon, W. Kim, and J. K. Lee, IEEE Trans. Plasma Sci. **27**, 1366 (1999).
7. A. Oda, Y. Sakai, H. Akashi, and H. Sugawara, J. Phys. D **32**, 2726 (1999).
8. Y. Ikeda, J. P. Verboncoeur, P. J. Christenson, and C. K. Birdsall, J. Appl. Phys. **86**, 2431 (1999).
9. A. V. Phelps and Z. Petrovic, Plasma Sources Sci. Technol. **8**, R21 (1999).
10. J. J. Thomson, *Conduction of Electricity through Gases* (Cambridge Univ. Press, Cambridge, 1928).
11. L. D. Tsendin, Fiz. Plazmy **8**, 169 (1982) [Sov. J. Plasma Phys. **8**, 96 (1982)]; Fiz. Plazmy **8**, 400 (1982) [Sov. J. Plasma Phys. **8**, 228 (1982)].
12. V. A. Shveigert, High Temp. **27**, 195 (1989).
13. V. P. Nagorny and P. J. Drallos, Plasma Sources Sci. Technol. **6**, 212 (1997).
14. E. W. McDaniel, *Collision Phenomena in Ionized Gases* (Wiley, New York, 1964).
15. G. J. M. Hagelaar, G. M. W. Kroesen, U. van Slooten, and H. Schreuders, J. Appl. Phys. **88**, 2252 (2000).
16. G. J. M. Hagelaar, F. J. de Hoog, and G. M. W. Kroesen, Phys. Rev. E **62**, 1452 (2000).
17. R. E. Marshak, Rev. Mod. Phys. **19**, 185 (1947).

Translated by P. Pozdeev

Technical Physics Letters, Vol. 28, No. 8, 2002, pp. 625–627. Translated from Pis'ma v Zhurnal Tekhnicheskoĭ Fiziki, Vol. 28, No. 15, 2002, pp. 10–16.
Original Russian Text Copyright © 2002 by Ushakov, Terent'ev, Yafarov.

Photoelectric Properties of Planar Structures with Double Schottky Barrier Treated in a High-Vacuum Microwave Discharge

N. M. Ushakov, S. A. Terent'ev, and R. K. Yafarov

Saratov Branch, Institute of Radio Engineering and Electronics, Russian Academy of Sciences, Saratov, Russia
e-mail: nmu@mail.saratov.ru

Received February 20, 2002

Abstract—The state of the surface of *n*-GaAs crystals upon high-vacuum microwave plasmachemical (HVMWPC) etching in various gas mixtures and the influence of the semiconductor surface condition on the photoelectric characteristics of related metal–semiconductor–metal structures with double Schottky barrier (MSMDSB structures) are investigated. Dependence of the HVMWPC etching rate of the GaAs surface on the gas mixture composition and substrate temperature is determined. It is shown that the HVMWPC etching regime strongly influences the photoelectric properties of MSMDSB structures: the treatment can lead to either growth or drop in photosensitivity of the samples. Optimum etching regimes are established for which good semiconductor surface quality and high photosensitivity of the MSMDSB structures are retained at a high etching rate. © *2002 MAIK "Nauka/Interperiodica".*

Planar semiconductor heterostructures with double Schottky barrier represent surface barrier structures with a working photosensitive area at both interelectrode gaps [1, 2]. The condition of the semiconductor surface upon special pretreatment significantly influences the process of photoelectric conversion in these structures [3]. Large areas of the periodic metal–semiconductor–metal (MSM) structures increase the detector sensitivity to optical signals, but lead to problems caused by relatively high stray currents. Traditional methods of eliminating stray currents are based on technologies of forming either doped storage rings at the metal–semiconductor interface or mesastructures. The latter method, involving no additional operations related to doping of the semiconductor surface, is preferred for the open surface-barrier MSM structures.

A promising technology for processing semiconductor surfaces and creating mesastructures is offered by the method of high-vacuum microwave plasmachemical (HVMWPC) dry etching [4, 5]. Using this technique, the surface of a semiconductor structure with a metallization pattern can be processed in the final technological stage in very mild regimes at reduced working gas pressures. This provides for the required anisotropy of etching and ensures high quality of the processed surface. The main requirement for a working gas used for the HVMWPC etching is that the plasma would feature the production of active particles forming volatile compounds with the material processed.

For gallium arsenide (GaAs), this requirement is satisfied only by chlorine-containing gas mixtures, which provide for the formation of volatile compounds with both components of the semiconductor material. Since the temperature of the transition to a gas phase is about 200°C for $GaCl_3$ and 131°C for $AsCl_3$, the etching process has to be conducted at a sufficiently high substrate temperature. In order to increase the efficiency of the etching process, an accelerating potential U (ranging from 50 to 200 V) was applied to the substrate holder. This factor significantly increases the etching rate. The HVMWPC etching in pure CCl_4 is accompanied by an intensive deposition of carbon onto the substrate surface. This was eliminated by adding oxygen to the working gas.

Figure 1a shows experimental plots of the GaAs etching rate versus percentage oxygen content in the CCl_4–O_2 mixture at a pressure of 8×10^{-2} Pa and various accelerating voltages. The most effective etching is observed in the gas mixtures containing 20–40% O_2. The etching rate is also significantly influenced by the substrate temperature, the effect being most pronounced below 200°C. Figure 1b presents experimental plots of the GaAs etching rate versus temperature for the process in a CCl_4–20% O_2 mixture at a total gas pressure of 0.1 Pa and various accelerating voltages. As can be seen, the process at U = 50–100 V begins at 130°C, while an increase in the bias voltage to 150 V reduces the etching onset temperature to 100°C. As the temperature increases to 200°C, the etching rate exhibits a linear growth for all accelerating voltages studied, while further increase in the temperature changes the etching rate rather insignificantly.

Thus, for CCl_4 as the working gas, the optimum process is conducted in a CCl_4–20% O_2 mixture at a tem-

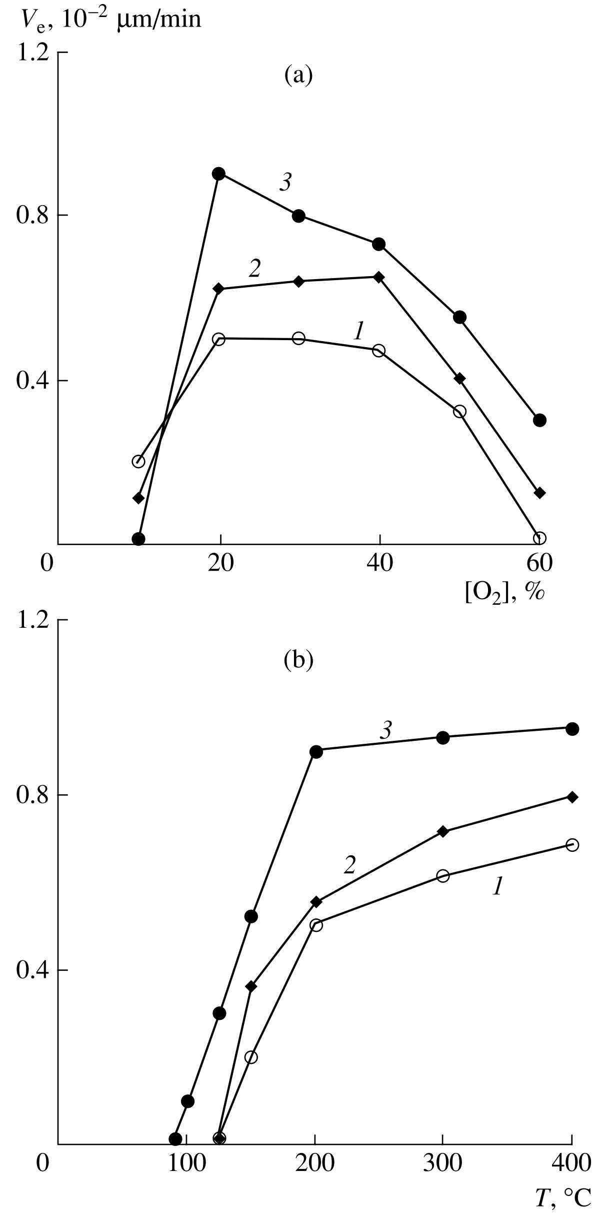

Fig. 1. Experimental plots of the *n*-GaAs etching rate V_e versus (a) percentage oxygen content [O$_2$] in the CCl_4–O_2 mixture and (b) substrate temperature *T* for the process conducted in the CCl_4–O_2 (5 : 1) mixture at a total gas pressure of ~0.1 Pa, a microwave power of 375 W, and various accelerating voltages *U* = 70 (*1*), 100 (*2*), and 150 V (*3*).

perature of 200–220°C. The MSM structures treated under these conditions in a mild regime (*U* = 50–100 V) exhibited a good quality of the processed surface, but the mesastructure relief height did not exceed 0.1–0.2 μm because of a low rate of GaAs etching. The results of photoelectric measurements on the samples processed in the indicated regime showed that the photocurrent increases two to three times as compared to analogous structures not subjected to HVMWPC etching.

In order to obtain mesastructures with grooves deeper than 0.5 μm, it is necessary to provide for etching at a higher rate as compared to that possible with the CCl_4–O_2 mixture. This can be achieved by using a modified gas mixture: HCl–CCl_4–O_2. The additive of HCl increases the concentration of chlorine radicals in the plasma, while CCl_4 effectively removes intrinsic oxide from the material surface. The structure and quality of the surface of GaAs samples upon HVMWPC etching at *U* = 50–100 V in the HCl–CCl_4–O_2 mixture were studied by high-energy electron diffraction in an EMR-100 electronograph and by method of carbon replicas in a PEM-100 transmission electron microscope. The initial (untreated) sample surface was coated with a thin amorphous layer through which reflections from single-crystalline GaAs could be observed. After the HVMWPC etching at *U* = 100 V, the sample surface exhibited a clear diffraction pattern of single crystal GaAs. The sample obtained upon the treatment at *U* = 50 V showed generally good surface quality with small etch pits. As the bias voltage is increased to 100 V, the etch pits disappear, leaving a high-quality GaAs surface. The optimum regime of HVMWPC etching for *n*-GaAs in an HCl–CCl_4–O_2 gas mixture corresponds to a substrate temperature of 200°C and an accelerating voltage in an interval from 70 to 100 V. This regime provides for both high etching rate and good quality of the surface of processed samples.

Figure 2 shows plots of the photoresponse U_{ph} versus electric bias voltage U_b measured for an interdigital MSM mesastructure (a = 5 μm, d = 10 μm, h = 100 μm, N = 10). The data are presented for three samples upon HVMWPC etching in an HCl–CCl_4–O_2 (2 : 2 : 1) mixture at different accelerating voltages: 50, 100, and 150 V (curves *1–3*, respectively). The photoelectric measurements were performed at a wavelength of 860 nm, a load resistance of 1 kΩ, and an incident light power of 1 μW. The photosensitivity of a sample processed at *U* = 150 V was on the level of 0.3–0.4 A/W, which corresponds to typical data reported for such structures. The photosensitivity of samples treated at an accelerating voltage of 50 and 100 V exceeded 0.4 A/W. A maximum photoresponse (~1 A/W) was observed for the sample etched at 100 V. This result is indicative of the switching of an internal photoelectric gain due to a change in the concentration of charge-carrier capture and production centers in the surface layer of the semiconductor. Variations in the gas mixture composition may lead to a decrease in photosensitivity of the MSM structures studied. In particular, an increase in the HCl content in the HCl–CCl_4–O_2 mixture led to enhanced etching of the oxide layer accompanied by the formation of centers of the nonequilibrium carrier recombination. For example, upon etching in the HCl–CCl_4–O_2 (4 : 2 : 1) mixture, the photosensitivity decreased by a factor of 1.5–2 (from 0.3 to 0.1–0.15 A/W).

Thus, the dry processing of GaAs by HVMWPC etching provides for an effective and fine method of modification of the semiconductor surface. The method requires selecting optimum composition of the gas

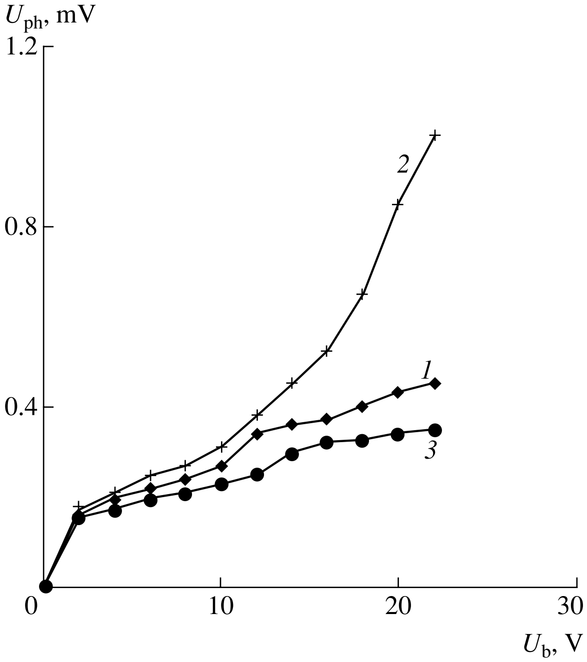

Fig. 2. Experimental plots of the photoresponse U_{ph} in an interdigital *n*-GaAs based MSM mesastructure versus interelectrode bias voltage U_b for three samples upon HVM-WPC etching in an HCl–CCl$_4$–O$_2$ (2 : 2 : 1) mixture at different accelerating voltages: (*1*) 70; (*2*) 100; (*3*) 150 V.

mixture and accelerating voltage in the reactor. For *n*-GaAs ($N_d = 10^{14}$–5×10^{15} cm^{-3}), the optimum HVM-WPC etching conditions are provided by an HCl–CCl$_4$–O$_2$ (2 : 2 : 1) mixture at an accelerating voltage of 90–100 V.

REFERENCES

1. N. M. Ushakov and V. I. Petrosyan, RF Patent No. 1800506, MKI H01 L 31/07, No. 4942723/25 (1991), Byull. Izobret. **9**, 4 (1993).
2. N. M. Ushakov and V. I. Petrosyan, Pis'ma Zh. Tekh. Fiz. **22** (14), 60 (1996) [Tech. Phys. Lett. **22**, 563 (1996)].
3. S. A. Terent'ev, N. M. Ushakov, A. N. Solodkiĭ, and V. I. Petrosyan, in *Proceedings of the 2nd All-Union Conference on Photoelectric Phenomena in Semiconductors, 1991*, pp. 23–25.
4. R. K. Yafarov and S. A. Terent'ev, USSR Inventor's Certificate No. 1807533 (1992).
5. A. S. Ignat'ev, S. A. Terent'ev, and R. K. Yafarov, Mikroélektronika, No. 4, 14 (1993).

Translated by P. Pozdeev

Technical Physics Letters, Vol. 28, No. 8, 2002, pp. 628–630. Translated from Pis'ma v Zhurnal Tekhnicheskoĭ Fiziki, Vol. 28, No. 15, 2002, pp. 17–23.
Original Russian Text Copyright © 2002 by Kulikov, Lesnyh, Trushin, Weber, Humer, Bittner, Sternberg.

The Effect of Neutron Irradiation on the Curie–Weiss Temperature of an Antiferroelectric Lead Zirconate Film

D. V. Kulikov[a], D. A. Lesnyh[a], Yu. V. Trushin[a,]*, H. W. Weber[b], K. Humer[b], R. Bittner[b], and A. R. Sternberg[c]

[a] *Ioffe Physicotechnical Institute, Russian Academy of Sciences, St. Petersburg, 194021 Russia*
** e-mail: trushin@theory.ioffe.rssi.ru*
[b] *Atomic Institute of Austrian Universities, Vienna, Austria*
[c] *Institute of Solid State Physics, University of Latvia, Riga, Latvia*

Received February 7, 2002

Abstract—A physical model describing variations of the Curie–Weiss temperature of an antiferroelectric lead zirconate ($PbZrO_3$) film under neutron irradiation is proposed. According to this model, a relative change in the Curie–Weiss temperature is proportional to the square of the total neutron dose. Theoretical estimates are in good agreement with experimental data. © *2002 MAIK "Nauka/Interperiodica".*

Thin ferroelectric and antiferroelectric films are promising materials for bolometric detectors [1–4]. One of the most important characteristics of a bolometer is the temperature dependence of the dielectric permittivity of a sensor material. In some applications, the instruments have to operate under conditions of a considerable radiation background and in a range of temperatures at which the material occurs in a paraelectric phase. Under the action of radiation, the dielectric permittivity may also exhibit a change which would result in decreasing the accuracy of bolometric measurements. Thus, it is necessary to study behavior of the dielectric permittivity of the film materials for bolometric sensors under the action of radiation.

Here we report on the results of investigation of the effect of neutron irradiation on the Curie–Weiss temperature of thin antiferroelectric lead zirconate ($PbZrO_3$) films.

The neutron irradiation of lead zirconate films was performed in a nuclear reactor of the Atomic Institute of Austrian Universities (Vienna). The samples were irradiated to different total neutron doses ($\Phi = 5 \times 10^{21}$ or 10^{22} m^{-2}). The dielectric constants of antiferroelectric $PbZrO_3$ films were studied as functions of the temperature before and after the exposure.

Figure 1 shows the experimental plots of ε versus temperature T for irradiated and unirradiated $PbZrO_3$ films. An analysis of the experimental results showed that the dielectric constant varies strictly in accordance with the Curie–Weiss law for paraelectrics:

$$\varepsilon = \frac{T_{CW}}{T - T_0}, \tag{1}$$

where T_{CW} is the Curie–Weiss constant and T_0 is the Curie–Weiss temperature. Processing of the experimental $\varepsilon(T)$ curves obtained for the samples before and after exposure showed that irradiation leads to a decrease in the Curie–Weiss temperature,

$$\Delta T_0 = T_0^{\text{irr}} - T_0^{\text{unirr}}, \tag{2}$$

where T_0^{irr} and T_0^{unirr} are the Curie–Weiss temperatures of the irradiated and unirradiated sample, respectively.

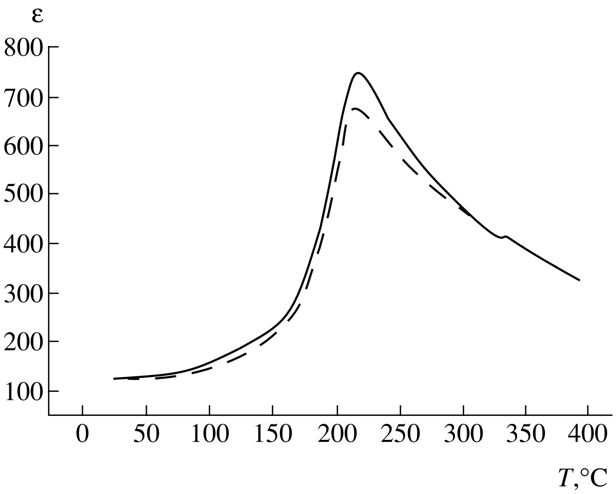

Fig. 1. Experimental plots of the dielectric constant ε versus temperature T for $PbZrO_3$ films measured before neutron irradiation (solid curve) and after exposure to a total dose of 10^{22} m^{-2}.

According to a microscopic theory of ferroelectrics [5], the Curie–Weiss temperature is described by the formula

$$T_0 = \frac{B}{a}\langle P_0^2\rangle, \tag{3}$$

where a and B are constants (entering into an expansion of the thermodynamic potential) and $\langle P_0^2\rangle$ is the space-average zero-temperature polarization square.

As demonstrated in [6], the Curie–Weiss temperature of a ferroelectric film bearing a charge distributed over the sample volume decreases as described by the formula

$$\Delta T_0 = -\frac{3B}{a}\langle P_b^2\rangle, \tag{4}$$

(note that $\Delta T_0 < 0$), where $\langle P_b^2\rangle$ is the space-average square polarization due to the spatially distributed charge.

Dividing expression (4) by formula (3), we determine a relative change in the Curie–Weiss temperature:

$$\gamma = -\frac{\Delta T_0}{T_0} = \frac{3\langle P_b^2\rangle}{\langle P_0^2\rangle}. \tag{5}$$

Using the results reported in [6], the value of γ defined in (5) can be estimated as

$$\gamma \approx \left(C_{ch}\frac{d_{ch}}{d_{dis}}\right)^2, \tag{6}$$

where C_{ch} is the relative density of the distributed charge, d_{ch} is the charged layer thickness, and d_{dis} is the average displacement of ions in the ferroelectric phase (usually amounting to a few tenths of an Ångström; for estimation, we take $d_{dis} \approx 0.03$ nm).

The charged centers (defects) can be of various types (impurities, interstitials, vacancies). Containing a large number of such defects, irradiated films must exhibit a decrease in the Curie–Weiss temperature T_0—and this is in fact observed. By processing the experimental results, we estimated a relative decrease in the Curie–Weiss temperature as $\gamma \approx 0.01$–0.1 for the samples irradiated to different doses (the exact values are presented by points in Fig. 2).

From an analysis of formula (6), one may conclude that there are two limiting cases of charge distribution in the film, whereby (i) only thin layers near electrodes are charged and (ii) the charge is distributed over the entire film volume. Let us estimate the charge density according to (6) in both limiting cases, taking $\gamma = 0.1$. In the first case, assuming the thickness of charged layers d_{ch} being on the order of several tens of nanometers (for a total film thickness of 1000 nm), we estimate the relative charge density as $C_{ch} \sim 10^{-4}$. This coincides in the order of magnitude with the concentration of point defects in lead zirconate irradiated in a reactor [3, 4]. In the second limiting case, when the charged layer thickness d_{ch} is equal to the film thickness, the relative charge density is $C_{ch} \sim 10^{-5}$.

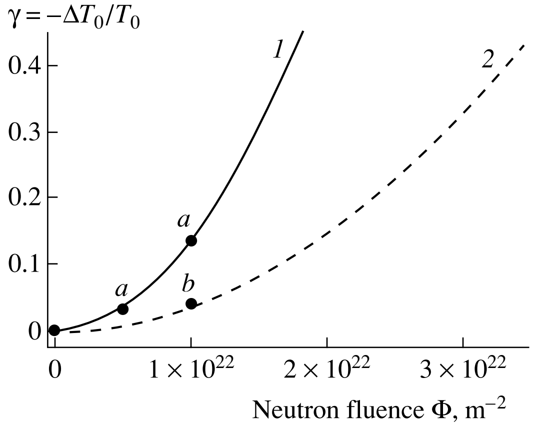

Fig. 2. Plots of the relative decrease $\gamma = K\Phi^2$ in the Curie–Weiss temperature versus neutron fluence Φ for antiferroelectric $PbZrO_3$ films. Points represent experimental data for annealed (*a*) and unannealed (*b*) samples. Curves show the results of calculations by formula $\gamma = K\Phi^2$ (8) with $K = 1.36 \times 10^{-45}$ m^4 (*1*) and $K = 3.6 \times 10^{-46}$ m^4 (*2*) corresponding to higher and lower charge densities in the films, respectively.

Real cases may represent intermediate variants, whereby the charge is distributed over the whole volume, while thin near-electrode layers can still be charged in a special manner. We may suggest that the second limiting case is more preferred for antiferroelectric materials such as lead zirconate. Indeed, dipole moments of the neighboring crystal cells in this antiferroelectric compound are oriented in the opposite directions [5] and, hence, the average electric field in the crystal is approximately zero. For this reason, a large number of charged defects are retained in the bulk, rather than displaced to the domain boundaries or to the surface. Thus, charges may be expected to spread almost uniformly over the film volume because defects in the neutron-irradiated samples are uniformly generated over the entire material.

At low neutron fluences Φ, the charge density (defect concentration) must be proportional to the total irradiation dose:

$$C_{ch} = \alpha\Phi, \tag{7}$$

where α is a proportionality factor. Therefore, a relative decrease in the Curie–Weiss temperature (γ) must change with the neutron dose according to a quadratic law (see formula (6)):

$$\gamma \approx \left(C_{\mathrm{ch}}\frac{d_{\mathrm{ch}}}{d_{\mathrm{dis}}}\right)^2 = \left(\frac{d_{\mathrm{ch}}}{d_{\mathrm{dis}}}\right)^2\alpha^2\Phi^2 = K\Phi^2, \qquad (8)$$

where $K = \left(\frac{d_{\mathrm{ch}}}{d_{\mathrm{dis}}}\right)^2\alpha^2$ is the coefficient of proportionality. Upon processing experimental data on the dielectric constant of neutron-irradiated lead zirconate films (see Fig. 2), we determined the relative decrease in the Curie–Weiss temperature for the two neutron doses studied: $\Phi = 5 \times 10^{21}$ m^{-2} (one sample) and 10^{22} m^{-2} (two samples). In one of the two samples irradiated to a large neutron dose (10^{22} m^{-2}), which was not annealed prior to the exposure, the decrease in the Curie–Weiss temperature T_0 was relatively small. In the other (preliminarily annealed) sample, the T_0 value decreased rather significantly.

Substituting the experimental values of γ and the corresponding neutron fluences into Eq. (8), we determine the proportionality coefficient $K \approx 1.36 \times 10^{-45}$ m^4 (using this value and taking d_{ch} = 1000 nm and $d_{\mathrm{dis}} \approx$ 0.03 nm, we can also estimate the proportionality factor in formula (7) as $\alpha \approx 1.16 \times 10^{-27}$ m^2). Figure 2 shows a theoretical curve of $\gamma(\Phi)$ (curve *1*) constructed by substituting this K value into formula (8). As can be seen, the two experimental values of γ corresponding to different neutron doses (points *a*) agree well with the theoretical curve, whereas the third γ value (point *b* shifted toward the abscissa axis) exhibits no such agreement. The latter sample (not annealed prior to the exposure) contains a large number of structural imperfections (impurities and/or other defects), which can serve as the charge recombination centers. Therefore, the charge density is smaller in the unannealed sample than in the film exposed after annealing (which removes all such recombination centers). Indeed, upon decreasing the proportionality factor between charge density and neutron fluence to $\alpha \approx 6 \times 10^{-28}$ m^2 (which is equivalent to decreasing the charge density at the same neutron dose), the proportionality coefficient K becomes equal to 3.6×10^{-46} m^4. The theoretical curve of $\gamma(\Phi)$ constructed using this K value in formula (8) agrees well with the experimental value of γ for the unannealed sample (Fig. 2, curve *2*). Thus, a relative decrease γ in the Curie–Weiss temperature T_0 is greater for the annealed sample than for the unannealed one.

One may expect that $\gamma(\Phi)$ will deviate from the quadratic law at high neutron doses, since the cascade regions begin to overlap and the charge recombination becomes more intensive. For this reason, the charge density must be proportional to the neutron fluence in a power below unity. Therefore, the relative decrease γ in the Curie–Weiss temperature must change slower as compared to the quadratic law and, at a very large irradiation dose, the $\gamma(\Phi)$ curve may exhibit saturation.

We presented the results of experimental and theoretical investigation of the influence of a neutron radiation upon the behavior of dielectric permittivity of antiferroelectric $PbZrO_3$ films. It was demonstrated that the Curie–Weiss temperature in the neutron-irradiated material decreases in proportion to the squared neutron dose. This behavior can be explained by the production of charged defect distributed over the film volume.

Acknowledgments. This work was supported in part by the EURATOM–OEAW Association, the Austrian Academy of Sciences, the Russian Foundation for Basic Research (projects nos. 99-02-17990 and 00-15-96812), and the Ministry of Education of the Russian Federation (project no. E00-3.4-93).

REFERENCES

1. M. Di Maio, PhD Thesis (RWTH, Aachen, 1999).
2. R. Bittner, K. Humer, H. W. Weber, *et al.*, in *Proceedings of ISIF, Colorado Springs, USA, 2001.*
3. D. V. Kulikov, Yu. V. Trushin, V. S. Kharlamov, *et al.*, Proc. SPIE **4348**, 264 (2001).
4. D. V. Kulikov, D. A. Lesnykh, Yu. V. Trushin, *et al.*, Pis'ma Zh. Tekh. Fiz. **27** (8), 19 (2001) [Tech. Phys. Lett. **27**, 316 (2001)].
5. B. A. Strukov and A. P. Levanyuk, *Ferroelectric Phenomena in Crystals* (Springer-Verlag, Berlin, 1998).
6. A. M. Bratkovsky and A. P. Levanyuk, Phys. Rev. B **61** (22), 15042 (2000).

Translated by P. Pozdeev

Technical Physics Letters, Vol. 28, No. 8, 2002, pp. 631–634. Translated from Pis'ma v Zhurnal Tekhnicheskoĭ Fiziki, Vol. 28, No. 15, 2002, pp. 24–32.
Original Russian Text Copyright © 2002 by Gurin, Shlyapin, Sabitov.

Variation of the Electroluminescence Spectra of ZnS:Mn Thin-Film Emitters Depending on the Excitation Level

N. T. Gurin, A. V. Shlyapin, and O. Yu. Sabitov
Ul'yanovsk State University, Ul'yanovsk, Russia
e-mail: soy@sv.uven.ru

Received January 29, 2002

Abstract—The electroluminescence (EL) spectra of ZnS:Mn thin-film emitters measured in various regions of the luminance wave exhibit, besides the bands characteristic of the intracenter emission from Mn^{2+} ions, additional EL bands peaked at ~530 and ~655 nm, which are probably related to the trapping of free electrons on deep centers formed by the sulfur vacancies V_S^{2+} and V_S^{+}. These traps may lead to the formation of a negative bulk charge in a near-cathode region, inducing a decrease in the growth rate (or even a drop) of current through the phosphor, as well as a decay of instantaneous luminance. *© 2002 MAIK "Nauka/Interperiodica".*

The emission spectra of ZnS:Mn electroluminescent thin-film (ELTF) emitters with a Mn concentration not exceeding 0.5–1.0 wt %, measured in a continuous regime using sinusoidal or pulsed excitation voltage, usually exhibit a single band with a maximum at λ_m = 580–585 nm [1, 2]. An increase in the Mn concentration leads to the appearance of additional bands at ~650, 739, 775, and 935 nm [1, 2], while the structures grown at a substrate temperature of about 200°C exhibit an additional emission peak at λ_m = 610 nm attributed to the complexes of manganese ions Mn^{2+} with sulfur vacancies [2–4]. In some cases, there was also a weak broad band of blue emission from zinc vacancies forming levels ~1 eV above the valence band top of ZnS:Mn [5–7]. The spectrum of ZnS:Mn crystals with small Mn^{2+} concentration (5×10^{-4} wt %) annealed in air exhibits, in addition to a yellow emission band from Mn^{2+}, a blue (self-induced) emission band at λ_m = 480 nm [8].

However, the available data do not allow us to judge variations in the ELTF emitter spectrum in connection with the kinetics of current passing in the phosphor and to various regions of the luminance wave. These restrictions are related to the fact that the spectra are usually measured for average values of ELTF emitter luminance in a continuous excitation regime, when a pause between adjacent pulses of the excitation voltage is insufficient for the neutralization of bulk charges in the near-cathode and near-anode regions of the phosphor [9].

This paper reports on the results of investigation of the electroluminescence (EL) spectra in relation to the kinetics of current passing in the phosphor layer. The spectra were measured in various regions of the luminance wave corresponding to different excitation levels. The neighboring luminance waves were not overlapping and a pause between the adjacent excitation voltage pulses was sufficient for neutralization of the bulk charge in the phosphor.

The experiments were performed on ELTF emitters with a MISIM type structure, where M layers represent a lower transparent 0.2-μm-thick SnO_2-based electrode deposited onto a glass substrate and the upper nontransparent thin-film Al electrode with a thickness of 0.15 μm and a diameter of 1.5 mm; S is the 0.54-μm-thick electroluminescent ZnS:Mn (0.5 wt %) layer, and I are the 0.15-μm-thick insulating ZrO_2–Y_2O_3 (13 wt %) layers. The ZnS:Mn phosphor layer was obtained by thermal evaporation in a quasi-closed volume in vacuum and by deposition onto a substrate heated to 250°C, followed by annealing for 1 h at 250°C. The upper nontransparent metal electrode was also obtained by thermal deposition in vacuum, while thin insulating layers were prepared using the electron-beam deposition technique.

We have experimentally studied luminance waves, representing the time variation of the instantaneous luminance L_λ at a given wavelength, using ELTF emitters excited with alternating-sign voltage pulses of a triangular shape. The excitation signal was supplied from a G6-34 generator equipped with an additional shaping amplifier and controlled by a G5-89 master generator. The maximum pulse amplitude was V_m = 160 V at a nonlinearity coefficient not exceeding 2%. In a single-start regime, the excitation voltage $V(t)$ represented a train of two-period triangular pulses with a repetition rate of 10 Hz. In the first half-period, either a positive or negative excitation half-wave can be applied to the upper electrode, which is referred to as the +Al and –Al

1063-7850/02/2808-0631$22.00 © 2002 MAIK "Nauka/Interperiodica"

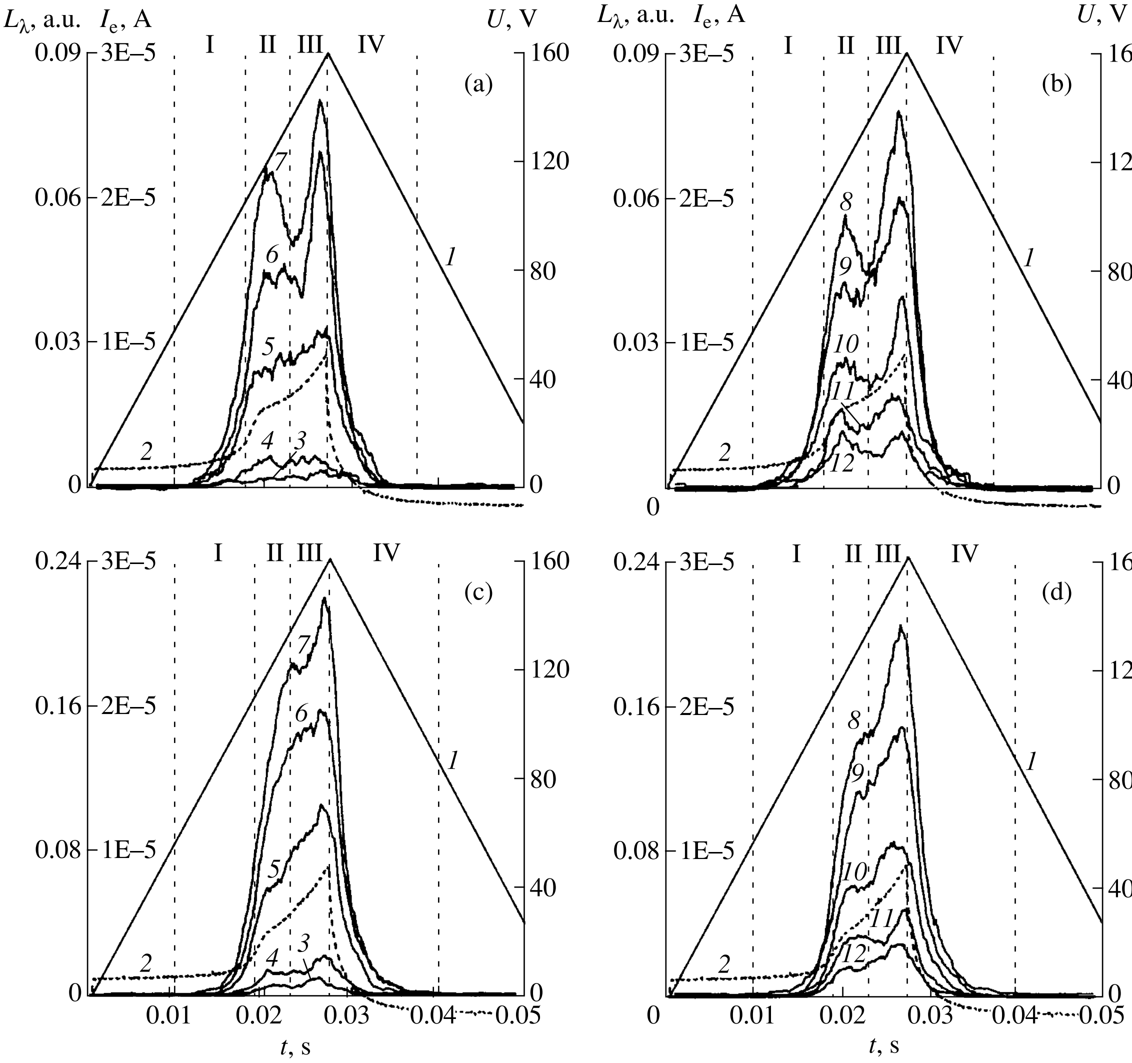

Fig. 1. The plots of (*1*) excitation voltage $V(t)$, (*2*) emitter current $I_e(t)$, and (*3–12*) partial emission spectra $L_\lambda(t)$ measured at (a, c) λ = 530 (*3*), 540 (*4*), 560 (*5*), 570 (*6*), 580 nm (*7*) and (b, d) λ = 590 (*8*), 600 (*9*), 610 (*10*), 630 (*11*), 650 nm (*12*) in the (a, b) –Al and (c, d) +Al regimes. I–IV are the luminance wave regions in which the $L_n(\lambda)$ spectra were measured.

regime, respectively. The time interval between single excitation cycles was T_s = 10 s. The emitter current I_e was measured in a 10 kΩ resistor connected in series to the emitter structure (the voltage drop on this resistor did not exceed 0.5% of V_m). The output radiation corresponding to the first luminance wave was transmitted through a MUM-2 monochromator (spectral uncertainty, 0.5 nm; linear dispersion, 4.8 nm/mm; slit width, 3 mm) in order to increase the sensitivity of detection and was measured with a FEU-79 photoelectron multiplier tube. The measurements were performed in a wavelength range from 400 to 750 nm at a 5-nm step.

The patterns of excitation voltage $V(t)$, ELTF emitter current $I_e(t)$, and luminance waves $L_\lambda(t)$ were recorded with the aid of a two-channel storage oscillograph of the S9-16 type linked via an interface to a personal computer. The system ensured measurement and storage of 2048 experimental points at a preset discretization period in each channel and 256 levels of amplitude quantization. The data were mathematically processed and graphically displayed using the application program packages MAPLE V (Release 4, Version 4.00b) and GRAPHER (Version 1.06, 2-D Graphing System). The experimental plots were approximated by curves drawn using TableCurve 2D (Version 2.03) program.

The average partial luminance at a given wavelength λ in a selected region n (n = I–IV) of the luminance wave was determined by the Talbot law for a flashing radiation source

$$L_n = \frac{1}{t_2 - t_1}\int_{t_1}^{t_2} L_\lambda(t)dt, \qquad (1)$$

where t_1 and t_2 are the time instants corresponding to

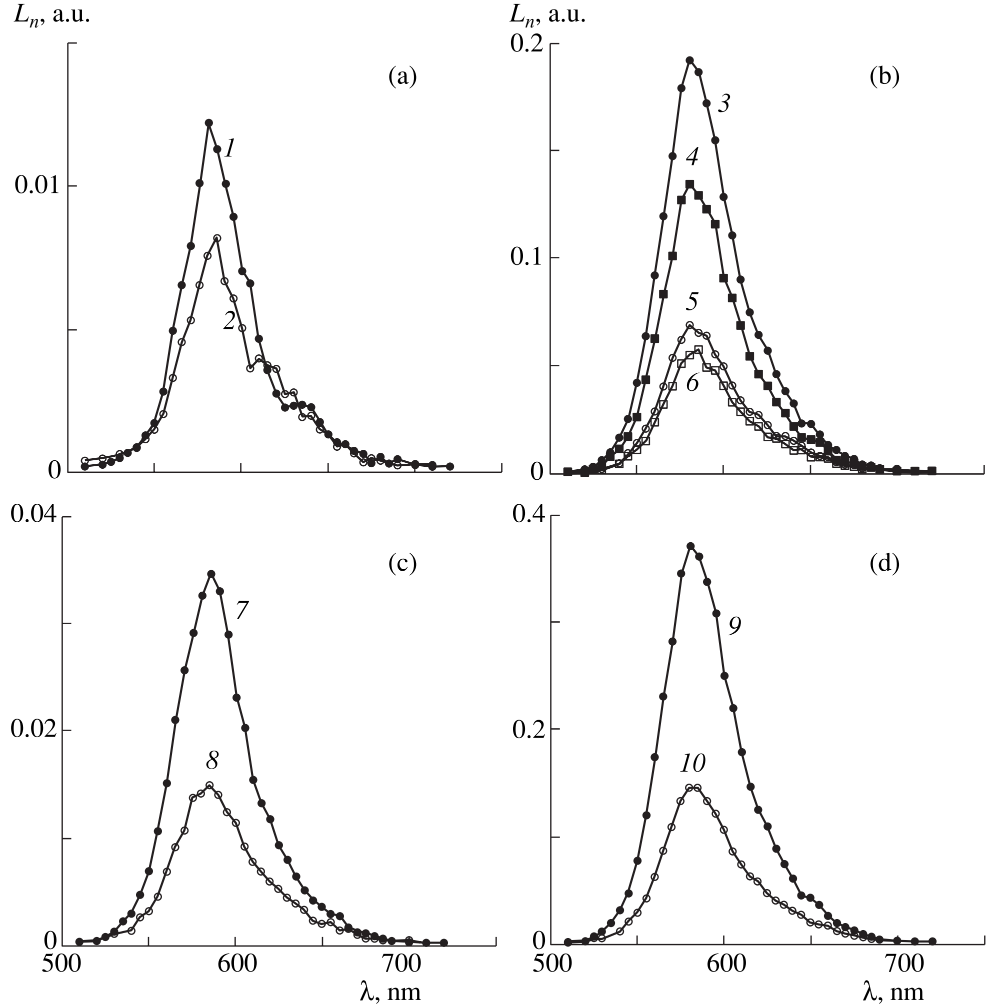

Fig. 2. The spectra of (a–c) emission intensity $L_n(\lambda)$ in various luminance wave regions (see Fig. 1) and (d) total EL intensity $L(\lambda)$ measured in (*1*, *3*, *4*, *7*, *9*) +Al and (*2*, *5*, *6*, *8*, *10*) –Al regimes: (*1*, *2*) region I; (*3*, *5*) region III; (*4*, *6*) region II; (*7*, *8*) region IV; (*9*, *10*) total spectra.

the beginning and end of the *n*th region (n = I–IV) of the luminance wave (see Fig. 1). The functions $L_n(\lambda)$ determine the emission spectra in the corresponding regions I–IV. The total EL spectrum was determined by summing the $L_n(\lambda)$ components as

$$L(\lambda) = \sum_n L_n(\lambda). \qquad (2)$$

As can be seen from Fig. 1, the shapes of emitter currents $I_e(t)$ and partial luminance waves $L_\lambda(t)$ significantly differ for the +Al and –Al regimes (as described in [9–11]) and vary depending on λ. Region I of the luminance wave corresponds to the "fast" portion of the $I_e(t)$ buildup (Fig. 1, curve *2*) provided that the excitation voltage exceeds the EL onset threshold of the given ELTF emitter [9–11]; regions II and III correspond to the "slow" portion of the $I_e(t)$ growth [9–11], the boundary between these regions corresponding approximately to the point of minimum $I_e(t)$ slope; and region IV corresponds to the decay portions of both $I_e(t)$ and $L(t)$ curves.

The spectral characteristics $L_n(\lambda)$ are also significantly different in various regions I–IV and for the +Al and –Al regimes (especially in region I) (Fig. 2). These distinctions are as follows:

(i) The main maximum in the EL spectrum for all regions I–IV and for both +Al and –Al regimes occurs at $\lambda_{m1} \approx 580$ nm, but the spectrum is complicated and comprises several overlapping bands peaked at $\lambda_{m2} \sim 560$ nm, $\lambda_{m3} \sim 600$ nm, $\lambda_{m4} \sim 610$–615 nm, $\lambda_{m5} \sim 635$ nm, and $\lambda_{m6} \sim 655$ nm (for both ±Al regimes); in the –Al variant, the spectra measured in all regions I–IV contain an additional band in the region of $\lambda = 510$–540 nm, which peaked approximately at $\lambda_{m7} \sim 530$ nm.

(ii) The relative intensity of the EL band at λ_{m3} increases for regions II and III (Fig. 2b), while that of the bands at λ_{m2}, λ_{m4}, and λ_{m5} decreases in regions II–IV (Figs. 2b and 2c).

(iii) The EL band at λ_{m6} ~ 655 nm is more pronounced in regions II–IV, especially in the +Al variant.

(iv) In the total EL spectrum $L(\lambda)$ (Fig. 2d), the manifestations of all bands except that at λ_{m6} are leveled and the spectrum acquires a shape typical of the emission from Mn^{2+} centers with the main maximum at ~ 585 nm [1–4].

(v) The EL spectra obtained in a similar manner for luminance waves corresponding to the second half-period of excitation pulses also exhibit a smooth shape with the main peak at ~ 585 nm and an additional maximum at λ_{m6} for regions I–III.

The above results can be interpreted as follows. According to [12, 13], the bands at λ_m = 557, 578, 600, 616, and 637 nm belong to the emission from Mn^{2+} ions and reflect various positions of these ions in a real crystal lattice of ZnS. The band at λ_m ~ 610 nm can be also attributed to the complex centers formed by Mn^{2+} ions and sulfur vacancies [2–4].

The band at $\lambda_{m7} \approx 530$ nm can be due to a recombination radiation accompanying the trapping of free electrons on deep centers representing the doubly ionized sulfur vacancies V_S^{2+} (situated ~1.3 eV above the valence band top [2, 14]). The fact that this band is observed only in the –Al regime is related to features of the ZnS:Mn film technology, whereby a part of the ZnS layer, adjacent to the upper Al electrode, is depleted of sulfur. As a result, V_S^{2+} vacancies may appear in this region under equilibrium conditions. A part of the free electrons, injected into the conduction band by tunneling emission from the surface states of the cathodic insulator–semiconductor interface, are trapped in the near-cathode region by V_S^{2+} centers possessing large electron capture cross sections.

The band at λ_{m6} ~ 655 nm is close to the signal at λ_m = 650 nm reported in [15] and can be assigned to the recombination emission accompanying the trapping of free electrons (in all regions I–IV) on deep centers with an energy of ~1.9 eV below the conduction band bottom. According to [16], these centers are probably related to singly ionized sulfur vacancies V_S^+. Such structural defects, representing together with zinc vacancies V_{Zn}^- the main types of defects for the given technology of ZnS:Mn layers [14], are uniformly distributed in the depth of the phosphor layer.

The trapping of electrons on deep centers related to V_S^{2+} and V_S^+ in the near-cathode region leads to the formation of a negative bulk charge in this region, which is probably one of the factors responsible for a decrease in the growth rate (or even a drop) of the current $I_e(t)$ and luminance $L_\lambda(t)$ in region II (Fig. 2) [9–11]. Note that the bands at λ_{m6} and λ_{m7} are not manifested in the emission spectra measured under usual conditions with continuous excitation, since the characteristic time of neutralization of the bulk negative charge in the near-cathode region amounts to 30–100 s [9].

The emission decay time of the luminance waves $L_\lambda(t)$ in region IV (Fig. 1) estimated assuming exponential behavior for the bands at λ_{m1}–λ_{m5} is τ = 1.6–2.0 ms, which is characteristic of the intracenter emission from Mn^{2+} ions (for the given Mn concentration in ZnS). For the bands at λ_{m6} and λ_{m7}, the total luminance decay time amounts to 7–9 ms.

REFERENCES

1. *Electroluminescent Sources of Light*, Ed. by I. K. Vereshchagin (Énergoatomizdat, Moscow, 1990).
2. A. N. Gruzintsev, Doctoral Dissertation (Chernogolovka, 1997).
3. A. N. Gruzintsev, Mikroélektronika **28** (2), 126 (1999).
4. A. N. Georgobiani, A. N. Gruzintsev, Xu Xurong, and Lou Zidong, Neorg. Mater. **35** (12), 1429 (1999).
5. W. E. Howard, O. Sahni, and P. M. Alt, J. Appl. Phys. **53** (1), 639 (1982).
6. K.-W. Yang, S. Owen, and T. John, IEEE Trans. Electron Devices **ED-30** (5), 452 (1983).
7. A. A. Douglas, J. F. Wager, D. C. Morton, *et al.*, J. Appl. Phys. **73** (1), 296 (1993).
8. M. F. Bulanyĭ, B. A. Polezhaev, and T. A. Prokof’ev, Zh. Tekh. Fiz. **67** (10), 132 (1997) [Tech. Phys. **42**, 1229 (1997)].
9. N. T. Gurin, O. Yu. Sabitov, and A. V. Shlyapin, Zh. Tekh. Fiz. **71** (8), 48 (2001) [Tech. Phys. **46**, 977 (2001)].
10. N. T. Gurin, O. Yu. Sabitov, and A. V. Shlyapin, Pis’ma Zh. Tekh. Fiz. **27** (22), 52 (2001) [Tech. Phys. Lett. **27**, 956 (2001)].
11. N. T. Gurin, A. V. Shlyapin, and O. Yu. Sabitov, Zh. Tekh. Fiz. **72** (2), 74 (2002) [Tech. Phys. **47**, 215 (2002)].
12. M. F. Bulanyĭ, B. A. Polezhaev, and T. A. Prokof’ev, Fiz. Tekh. Poluprovodn. (St. Petersburg) **32** (6), 673 (1998) [Semiconductors **32**, 603 (1998)].
13. M. F. Bulanyĭ, A. V. Kovalenko, and B. A. Polezhaev, in *Proceedings of the International Conference on Luminescence, Moscow, 2001* (Fiz. Inst. Ross. Akad. Nauk, Moscow, 2001), p. 98.
14. *Physics of II-VI Semiconductor Compounds*, Ed. by A. N. Georgobiani and M. K. Sheĭnkman (Nauka, Moscow, 1986).
15. D. D. Thong and O. Goede, Phys. Status Solidi B **120**, K145 (1983).
16. A. N. Krasnov, R. C. Baycar, and P. G. Hofstra, J. Cryst. Growth **194**, 53 (1998).

Translated by P. Pozdeev

Technical Physics Letters, Vol. 28, No. 8, 2002, pp. 635–636. Translated from Pis'ma v Zhurnal Tekhnicheskoĭ Fiziki, Vol. 28, No. 15, 2002, pp. 33–36.
Original Russian Text Copyright © 2002 by Poklonski, Mityanok, Vyrko.

The Rameau–Shockley Relation for an *RCL* Circuit

N. A. Poklonski, V. V. Mityanok, and S. A. Vyrko
Belarussian State University, Minsk, Belarus
e-mail: Poklonski@bsu.by

Received March 5, 2002

Abstract—The current induced by a point particle flying through a flat capacitor, entering into a circuit comprising parallel *RL* and *RC* chains connected to a measuring ampermeter, is calculated. It is shown that, for the circuit parameters obeying the condition $RC = L/R$, the induced current is directly proportional to the time of charge motion between the capacitor plates (so that the current pulse exhibits a triangular shape). *© 2002 MAIK “Nauka/Interperiodica”.*

The Rameau–Shockley relation (theorem) reads as follows (see [1, 2] and references therein): a point charge Q moving at a constant velocity v perpendicularly to the plates of a flat capacitor induces in an external short-circuit chain (possessing neither inductance nor active resistance) a rectangular current pulse with the amplitude

$$I = \frac{Qv}{b}, \tag{1}$$

where b is the distance between plates; the current pulse duration is equal to b/v, the charge time-of-flight between the capacitor plates.

Formula (1) was generalized [2] to the case of a circuit comprising a capacitor (with a capacitance C) connected in series to a resistor (with a resistance R), whereby the current induced in the external chain varies as

$$I = \frac{Qv}{b}\left[1 - \exp\left(-\frac{t}{RC}\right)\right], \tag{2}$$

where $0 \le t \le b/v$.

We aimed at further generalizing the results [2] to the case of a circuit including, in addition to the capacitor and resistor, a coil possessing an inductance L (see figure). As can be seen, in the limit of $R_2 \longrightarrow \infty$ and $L \longrightarrow 0$, this circuit reduces to that considered in [2].

A charge Q flying at a constant velocity v between the capacitor plates induces a current I_1 in the RC chain and a current I_2 in the LC chain, the corresponding potentials being $\varphi_1 = I_1R_1$ and $\varphi_2 = I_2R_2$. The RC chain obeys the relation [3]

$$C\left(\frac{d\varphi}{dt} - \frac{d\varphi_1}{dt}\right) = I_1 = \frac{Qv}{b}\left[1 - \exp\left(-\frac{t}{R_1C}\right)\right], \tag{3}$$

where the current I_1 is determined by formula (2). Using relation (3) and taking into account that $\varphi_1 = I_1R_1$, we obtain

$$\begin{aligned}\varphi &= \varphi_1 + \frac{Qv}{Cb}\int\left[1 - \exp\left(-\frac{t}{R_1C}\right)\right]dt \\ &= R_1\frac{Qv}{b} + \frac{Qv}{Cb}t + A,\end{aligned} \tag{4}$$

where A is an integration constant. For the constant A in formula (4) selected so that $\varphi = 0$ at $t = 0$, the circuit potential varies as

$$\varphi = \frac{Qvt}{Cb}, \tag{5}$$

where $0 \le t \le b/v$.

For the LC chain (see figure), formula (5) yields [3]

$$L\frac{dI_2}{dt} = \varphi - \varphi_2 = \frac{Qvt}{Cb} - I_2R_2. \tag{6}$$

A solution to this equation will be found in the form of

$$I_2 = B(t)\exp(-tR_2/L). \tag{7}$$

Substituting expression (7) into Eq. (6), we obtain

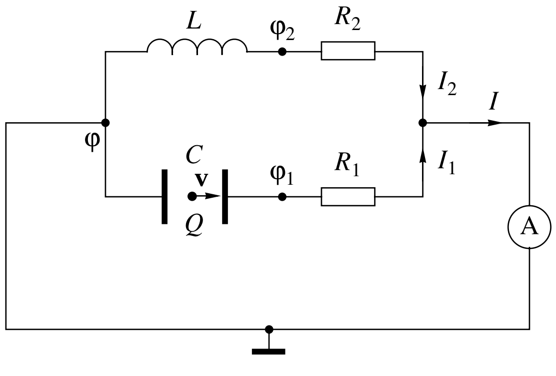

A diagram of currents induced in an *RCL* circuit by a charge Q moving perpendicularly to the plates of a flat capacitor.

$dB/dt = (Q\mathrm{v}t/LbC)\exp(tR_2/L)$, which can be integrated to yield

$$B = \frac{Q\mathrm{v}}{LCb}\left\{\frac{L}{R_2}t\exp(tR_2/L) - \frac{L^2}{R_2^2}\exp(tR_2/L) + K\right\}. \quad (8)$$

Here, $K = (L/R_2)^2$ is the integration constant, which can be determined from the initial condition that $I_2 = 0$ for $t = 0$. Substituting formula (8) into expression (7), we obtain

$$I_2 = \frac{Q\mathrm{v}}{LCb}\left\{\frac{L}{R_2}t - \frac{L^2}{R_2^2}(1 - \exp(-tR_2/L))\right\}. \quad (9)$$

Using relations (3) and (9), we determine the total current $I = I_1 + I_2$ in the chain (see figure):

$$I = \frac{Q\mathrm{v}}{b}\left[1 - \exp\left(-\frac{t}{R_1C}\right)\right] + \frac{Q\mathrm{v}}{LCb}\left\{\frac{L}{R_2}t - \frac{L^2}{R_2^2}(1 - \exp(-tR_2/L))\right\}. \quad (10)$$

For a circuit with the parameters obeying the relations $R_1 = R_2 = R$ and $RC = L/R$, formula (10) describes a triangular current pulse:

$$I = \frac{Q\mathrm{v}}{CbR}t, \quad (11)$$

where $0 \le t \le b/\mathrm{v}$. Note that, according to [4, 5], the resistance of a two-terminal element with $R_1 = R_2 = R$ and $RC = L/R$ (in a circuit with the ampermeter replaced by an ac field generator) is purely active and equals R irrespective of the generator frequency.

Thus, it was demonstrated that triangular pulses of induced current can be obtained in a circuit comprising parallel *RC* and *RL* chains with specially selected parameters. Such a circuit can increase the possibilities of particle detectors [6–9].

REFERENCES

1. P. De Visschere, Solid-State Electron. **33** (4), 455 (1990).
2. A. N. Inovenkov, O. V. Konstantinov, and V. I. Pirogov, Zh. Tekh. Fiz. **63** (9), 1 (1993) [Tech. Phys. **38**, 739 (1993)].
3. I. E. Tamm, *Principles of the Theory of Electricity* (Nauka, Moscow, 1989).
4. L. A. Vaĭnshteĭn, Usp. Fiz. Nauk **118** (2), 339 (1976) [Sov. Phys. Usp. **19**, 189 (1976)].
5. Yu. S. Barash and V. L. Ginzburg, Usp. Fiz. Nauk **118** (3), 523 (1976) [Sov. Phys. Usp. **19**, 263 (1976)].
6. Yu. K. Akimov, O. V. Ignat'ev, A. I. Kalinin, and V. F. Kushniruk, *Semiconductor Detectors in Experimental Physics* (Énergoatomizdat, Moscow, 1989).
7. V. K. Lyapidevskiĭ and V. B. Perezhogin, Prib. Tekh. Éksp., No. 2, 24 (1990).
8. M. P. Lorikyan, Usp. Fiz. Nauk **165** (11), 1323 (1995) [Phys. Usp. **38**, 1271 (1995)].
9. V. N. Tsytovich and J. Winter, Usp. Fiz. Nauk **168** (8), 899 (1998) [Phys. Usp. **41**, 815 (1998)].

Translated by P. Pozdeev

Technical Physics Letters, Vol. 28, No. 8, 2002, pp. 637–639. Translated from Pis'ma v Zhurnal Tekhnicheskoĭ Fiziki, Vol. 28, No. 15, 2002, pp. 37–42.
Original Russian Text Copyright © 2002 by Tkachenko.

On the Homogeneity of a Conductor Heated by Electric Current Pulse

S. I. Tkachenko

Institute for High Energy Densities, Associated Institute for High Temperatures, Russian Academy of Sciences, Moscow, Russia

e-mail: svt@iht.mpei.ac.ru

Received March 5, 2002

Abstract—A simple criterion is suggested for selecting a proper regime of electric explosion of a thin cylindrical conductor heated by a high-power current pulse. The selected regime ensures homogeneous heating of the conductor, which is necessary for investigating various physical processes and studying thermal and electrical properties of liquid (including refractory) metals at high temperatures. *© 2002 MAIK "Nauka/Interperiodica".*

The electric explosion of conductors is widely used for the investigation of thermodynamic and electrical properties of substances at high temperatures up to $T \sim$ 1–10 kK. However, certain features related to the interpretation of experimental data obtained by this method require elucidation and discussion.

In particular, refractory metals at high temperatures developed in such experiments occur in a solid or liquid state. The optical thickness of solid tungsten in the visible spectral range is $l_{\text{opt}} \sim 10$ nm [1] and, even at a twofold expansion observed in the experiments (see, e.g. [2]), increases rather insignificantly. Therefore, optical methods cannot be used for studying the distribution of parameters over a sample volume and provide information only on integral characteristics such as the heating current $I(t)$, voltage drop $U(t)$, and expanding conductor radius $a(t)$ (t is the heating time). Accordingly, we can determine the average values of density,

$$\rho(t) = \rho_0[a_0/a(t)]^2,$$

conductivity,

$$\sigma(t) = I(t)l[\pi a^2(t)U(t)]^{-1},$$

and specific deposited energy,

$$h(t) = m^{-1}\int_0^t I(\tau)U(\tau)d\tau + h_0;$$

where ρ_0, a_0, h_0, and m are initial values of the density, radius, specific enthalpy, and mass of the wire sample. Since the sample temperature is determined by measuring radiation emitted from the sample surface, it is necessary to assume that the material is homogeneous over the volume. Then we can consider the above values as temperature-dependent properties of the material $\rho(T)$, $\sigma(T)$, and $h(T)$. In this case, we can also calculate a specific heat capacity as

$$c(T) = U(t)I(t)m^{-1}(dT/dt)^{-1}.$$

Thus, the assumption of homogeneity is a key point in interpreting the experimental data. According to [3], the pattern observed for a heating time τ_l exceeding the characteristic time of magnetohydrodynamic (MHD) instability development τ_{MHD} by a factor of 3–4 is characterized by clearly distinguishable axially symmetric regions with periodic breaks of the wire. Therefore, regimes providing for a spatially homogeneous heating are restricted to a time of $\tau_l < \tau_{\text{MHD}}$.

The results of calculations for tungsten (W) and tantalum (Ta) wires heated by current pulses with an amplitude of $I \sim 15$ kA are presented in the table. The skin layer thickness δ_s in all these regimes exceeds the initial wire radius by one order of magnitude. The regimes differ from one another by the values of parameters, including the initial radius a_0, maximum current density j_{m}, and the characteristic times τ_{MHD} and τ_l. Note that τ_l was calculated as the time required to heat a liquid conductor from the melting point T_{m0} to a temperature of $T = T_{\text{m0}} + \Delta T$ ($\Delta T = 3$ kK for Ta and 2 kK for W wires).

The regimes in the table are divided into two groups obeying the condition (1) $\tau_l < \tau_{\text{MHD}}$ and (2) $\tau_l > \tau_{\text{MHD}}$. The spatial homogeneity is retained for the regimes of group 1 and can be lost in group 2. In particular, the regimes with smaller initial radii should be preferred for experimental investigations of the properties of liquid metals.

A threshold current density for which $\tau_l = \tau_{\mathrm{MHD}}$ can be calculated using the relation

$$j_t \sim \frac{1}{2}\sqrt{\rho_0\mu\mu_0}\,c\sigma\Delta T(\rho_f/\rho_0)^2,$$

where σ is the electric conductivity, $\mu\mu_0$ is the magnetic permeability, and ρ_0 and ρ_f are the initial and final densities. Since the last relationship includes only quantities characterizing the initial and final states of the substance, we may calculate the threshold value j_t for each particular metal. For the degree of heating employed in our study, these values are 40 GA/m^2 for Ta and 50 GA/m^2 for W. Using these values, we can estimate the time of homogeneous heating of a liquid metal conductor ($\tau_l \sim 5$ μs).

Then we analyzed the effect of energy losses via radiation and evaporation from the surface on the degree of radial inhomogeneity. For this purpose, we modeled the process of energy transfer in a thin surface layer of the sample. It was assumed that the layer thickness d_s is much smaller than the wire radius ($d_s \ll a_0$). In this case, the energy balance equation (in the Cartesian coordinates) can be written as

$$c\rho\frac{\partial T}{\partial t} = \frac{\partial}{\partial x}\left[\kappa\frac{\partial T}{\partial x}\right] + \frac{j^2}{\sigma},$$

with the boundary conditions taking into account the evaporation and radiation from the surface:

$$\kappa\frac{\partial T}{\partial x}\bigg|_{x=a} = -\rho v_{\mathrm{b}}(\Lambda - a_{\mathrm{k}}RT_{\mathrm{w}}) - \varepsilon_r\sigma_{\mathrm{SB}}T_{\mathrm{w}}^4.$$

Here, κ is the thermal conductivity, Λ is the specific heat of evaporation, ε_r is the emittance, a_{k} is a dimensionless constant ($a_{\mathrm{k}} = 0.77$ for the evaporation into vacuum, and 0.5, for that into a medium characterized by a high counterpressure [4]), σ_{SB} is the Stefan–Boltzmann constant, T_{w} is the wire surface temperature, R is the gas constant, $v_{\mathrm{b}} = v_0\exp(-\Lambda/RT_{\mathrm{w}})$ is the evaporation wave velocity, and v_0 is the sound velocity.

The properties of a liquid metal were described using the equation of state of a low-compressible medium

$$\rho = \rho_{\mathrm{m0}}[1 - \alpha(T - T_{\mathrm{m0}})],$$

while the electric conductivity was determined by a semiempirical formula [5]

$$\sigma = \frac{\sigma_{\mathrm{m0}}}{1 + \beta(T - T_{\mathrm{m0}})},$$

where ρ_{m0} and σ_{m0} are the density and electric conductivity of a liquid phase at the melting temperature, α is the coefficient of thermal expansion, and β is the temperature coefficient of electric conductivity. The thermal conductivity was calculated by the Wiedemann–Franz law $\kappa = k_{\mathrm{WF}}T\sigma$, k_{WF} being the corresponding constant factor.

The sample temperature is usually measured by an optical pyrometer. In order to evaluate the effect of surface losses on the results of temperature measurements, it is necessary to provide for a surface resolution smaller than the optical thickness. On the other hand, the region of modeling should be sufficiently large to allow for the thermal conductivity effect to be taken into consideration. In other words, the size of the object modeled must be greater than $\delta_T \sim \sqrt{\kappa\tau_l(c\rho)^{-1}}$, but the external cell should be smaller than the optical thickness l_{opt}. Under our experimental conditions, $\delta_T \gg l_{\mathrm{opt}}$ and both requirements can be satisfied using a nonuniform lattice.

The results of modeling are presented in Figs. 1 and 2. As can be seen from these data, the surface processes may influence the accuracy of measurements. For current densities $j < j_t$, this effect is especially pronounced beginning with $T \sim 8$ kK. For example, the bulk and surface temperatures at $T \sim 8$ kK reaches ~2% and increases with temperature, reaching ~25% at 10 kK. It should be noted that a difference in temperature related to radiative losses does not exceed 1–1.5% up to $T \sim 11$ kK. The accuracy of the density measurements is affected by the surface losses to a much lower

Characteristic parameters for the electric explosion of conductors

Parameter	Group 1						Group 2			
a_0, mm	0.15		0.175		0.25		0.5		0.7	
j_{m}, GA/m^2	210		150		76		19		10	
Metal	W	Ta	W	Ta	W	Ta	W	Ta	W	Ta
τ_{MHD}, μs	1.3	1.1	1.8	1.5	4	3	15	13	29	25
τ_l, μs	0.3	0.2	0.5	0.4	2.2	1.7	36	23	140	90

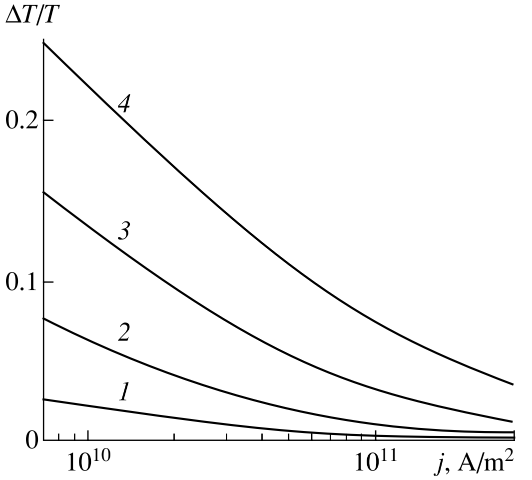

Fig. 1. Plots of the relative difference between surface and bulk temperatures versus current density for a metal wire heated to various temperatures T = 7 (*1*), 8 (*2*), 9 (*3*), and 10 kK (*4*).

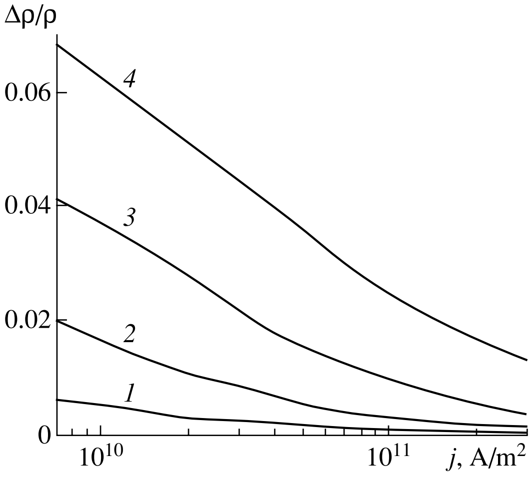

Fig. 2. Plots of the relative difference between surface and bulk material densities versus current density for a metal wire heated to various temperatures T = 7 (*1*), 8 (*2*), 9 (*3*), and 10 kK (*4*).

extent (Fig. 2), since the external (less heated) layer is very thin.

If the sample temperature is understated, the uncertainty of the temperature measurements may significantly influence the values of parameters at the critical point: the critical temperatures and densities may be considerably understated as well.

In selecting the regime of a sample heating by a high-power current pulse, it is necessary to provide for a current density much greater than j_t in order to eliminate the development of MHD instability in the course of experiments used to determine the properties of liquid substances.

The sample temperature measured by optical methods must be corrected for the surface energy losses at $T > 8$ kK. Note that evaporation from the sample surface can be suppressed by using transparent plates (see, e.g., [6]), but then the influence of such plates on the results of measurements becomes an open question.

Acknowledgments. This study was supported by the Russian Foundation for Basic Research.

REFERENCES

1. *Handbook of Optical Constants of Solids*, Ed. by E. D. Palik (Academic, New York, 1985).
2. S. V. Koval’, N. I. Kuskova, and S. I. Tkachenko, Teplofiz. Vys. Temp. **35** (6), 876 (1997).
3. K. B. Abramova, N. A. Zlatin, and B. P. Peregud, Zh. Éksp. Teor. Fiz. **69** (6), 2007 (1975) [Sov. Phys. JETP **42**, 1019 (1975)].
4. S. I. Anisimov, Ya. A. Imas, G. S. Romanov, and Yu. V. Khodyko, *Effect of High-Power Radiation on Metals* (Nauka, Moscow, 1970).
5. H. Knoepfel, *Pulsed High Magnetic Fields* (North-Holland, Amsterdam, 1970; Mir, Moscow, 1972).
6. V. N. Korobenko and A. I. Savvatimskiĭ, Teplofiz. Vys. Temp. **36**, 725 (1998).

Translated by P. Pozdeev

Technical Physics Letters, Vol. 28, No. 8, 2002, pp. 640–641. Translated from Pis'ma v Zhurnal Tekhnicheskoĭ Fiziki, Vol. 28, No. 15, 2002, pp. 43–47.
Original Russian Text Copyright © 2002 by Mukha, Surkaev.

Studying the Effect of Nonlinearity of Interacting Acoustic Shock Waves

Yu. P. Mukha and A. L. Surkaev
Volzhskiĭ Polytechnical Institute, Branch of the Volgograd State Technical University, Volzhskiĭ, Russia
e-mail: vfaculty@volpi.ru

Received February 18, 2002

Abstract—Nonlinear effects arising during the interaction of two identical acoustic shock waves in a condensed medium are studied for the waves generated by the electric explosion of two metallic conductors in a cylindrical chamber. *© 2002 MAIK "Nauka/Interperiodica".*

The phenomenon of electric discharge in condensed media has been extensively studied (see, e.g., [1, 2]). As is known, the electric explosion of a metal conductor leads to excitation of acoustic shock waves in the surrounding condensed medium.

Our aim was to study nonlinear processes arising during the interaction of two identical acoustic shock waves generated in a condensed medium by the electric explosion of two metallic conductors. This paper is a continuation of our previous communication [3] where we presented the results of an experimental investigation of the interaction of two identical acoustic shock waves. The pressure was measured by a piezotransducer [4] fixed to the wall of a cylindrical explosion chamber.

In the general case, the hydrodynamic equations are nonlinear [5]. In an approximated description, a pressure wave of finite amplitude can be represented as a sum of two terms—the wave with a small amplitude p' (corresponding to the linearized equations) and the quadratic correction p'':

$$p = p' + p''. \tag{1}$$

The plane wave in Lagrange coordinates is described by the equation

$$p'_{tt} - c_0^2 p'_{\zeta\zeta} = 0. \tag{2}$$

Here and below, letter subscripts denote the corresponding derivatives. The second-order pressure term obeys a nonlinear equation

$$p''_{tt} - c_0^2 p''_{\zeta\zeta} = G(p'^2)_{tt}, \tag{3}$$

where G is the coefficient of nonlinearity given by the formula

$$G = \frac{1}{\rho_0 c_0^2}\left[1 + \frac{1}{2}\rho_0\left(\frac{dc^2}{dp}\right)_0\right] \tag{4}$$

(zero subscript at the derivative indicates that the value refers to $p = 0$).

Based on the experimental results obtained in [3] and those reported by other researchers, one may conclude that the pressure is described by an exponential function of time. We suggest using the following analytical expression:

$$p(t) = a\left(t - \frac{\zeta}{c_0}\right)^b e^{c\left(t - \frac{\zeta}{c_0}\right)}, \tag{5}$$

where ζ is a coordinate and a, b, and c are coefficients which will be determined by fitting to an experimental curve. At a point with the zero coordinate, the pressure varies as

$$p(t) = at^b e^{ct}. \tag{6}$$

Figure 1 presents the experimental plot and the analytical curve of the pressure as a function of time, from which we obtained $a = 3.7 \times 10^{12}$ Pa/s, $b = 0.99$, and $c = -0.1 \times 10^5$ s^{-1}. From the areas under curves, the relative error was estimated as $\delta = 8.5\%$.

A nonlinear interaction of two plane waves violates the principle of superposition valid in the linear case. A quadratic correction can be presented as

$$p'' = \frac{1}{2}Gt(p_1'^2)_t + \frac{1}{2}Gt(p_2'^2)_t + Gt(p_1'p_2')_t, \tag{7}$$

where subscripts 1 and 2 refer to the corresponding wave. The simultaneous explosion of two identical conductors in a cylindrical chamber gives rise to two identical acoustic shock waves. Using Eq. (1) and the condition of equivalence of the two waves, the resulting pressure wave with a quadratic correction term is as follows:

$$p = 2p' + 2Gt(p'^2)_t. \tag{8}$$

Written in the Tait form [6], the equation of state for

1063-7850/02/2808-0640$22.00 © 2002 MAIK "Nauka/Interperiodica"

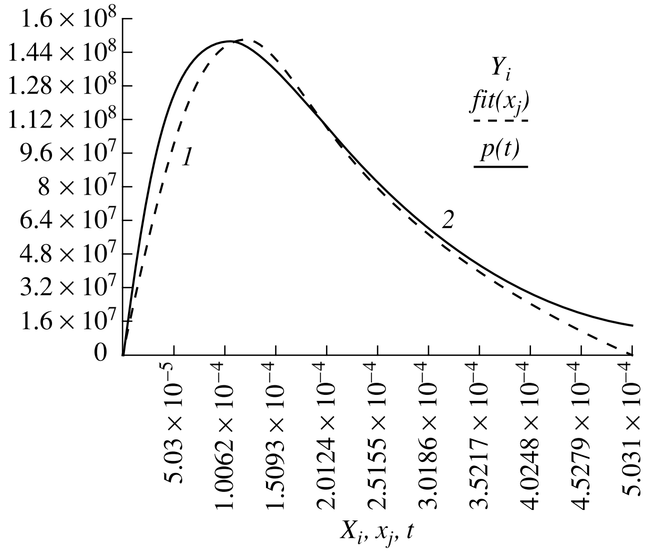

Fig. 1. Time variation of the pressure in the incident acoustic shock wave: (*1*) experiment; (*2*) theoretical analytical curve.

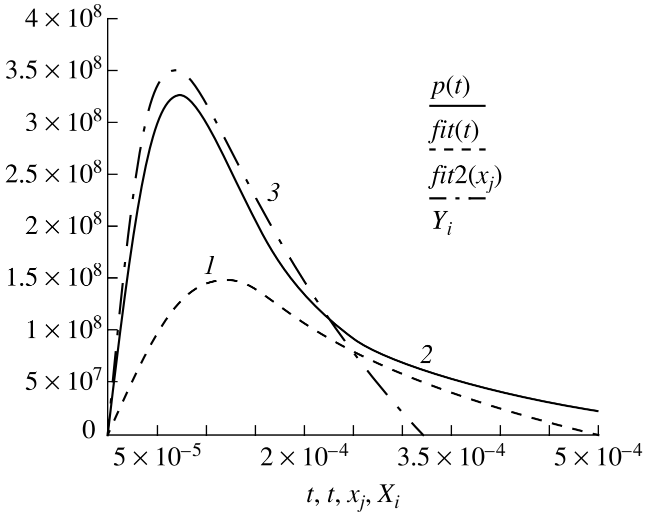

Fig. 2. Time variation of the pressure during the interaction of two acoustic shock waves: (*1*) experimental curve for the incident wave; (*2*) theoretical analytical curve for the resulting wave; (*3*) experimental curve for the resulting wave.

a condensed medium is

$$p = B\left[\left(\frac{\rho}{\rho_0}\right)^n - 1\right], \tag{9}$$

where ρ and ρ_0 are the densities of the medium in the excited and equilibrium states, respectively, and the coefficients are $B = 3.045 \times 10^8$ Pa and $n = 7.15$.

Using expression (8) and taking into account formulas (4) and (6) and the relation $c^2 = \partial p/\partial\rho$, we arrive at a final equation describing the pressure in an acoustic shock wave in the system studied:

$$p(t) = 2at^b e^{ct} + \frac{4(b+ct)}{\rho_0 c_0^2}\left[1 + \frac{n(n-1)B}{2\rho_0 c_0^2}\right]a^2 t^{2b} e^{2ct}. \tag{10}$$

In the experiments, the shock waves in a cylindrical chamber were excited by the electric explosion of two copper wires with a diameter of $d = 1.2 \times 10^{-3}$ m and a length of 2.5 cm, which were connected in series and arranged on the chamber axis at a distance of $L = 30 \times 10^{-2}$ m from each other. The initial voltage of the storage bank was $U_0 = 4.0 \times 10^3$ V.

Considering a wave of the form presented by Eq. (6), we determined the time variation of the resulting pressure developed by the interacting acoustic shock waves with an allowance for the quadratic nonlinearity (Fig. 2). As can be seen, the theoretical results (curve *2*) agree well with the experimental data (curve *3*): uncertainty of the calculated wave amplitude relative to the experimental value does not exceed $\delta_1 = 8\%$.

REFERENCES

1. E. V. Krivitskiĭ, *Dynamics of Electric Explosion in Liquid* (Naukova Dumka, Kiev, 1986).
2. V. A. Burtsev, *Electric Explosion of Conductors and Their Application* (Nauka, Moscow, 1990).
3. A. L. Surkaev, V. G. Kul'kov, and G. N. Talyzov, Pis'ma Zh. Tekh. Fiz. **27** (12), 6 (2001) [Tech. Phys. Lett. **27**, 487 (2001)].
4. A. L. Surkaev, V. G. Kul'kov, and G. N. Talyzov, in *Proceedings of the XXX Ural Workshop "Heterogeneous Structures," Yekaterinburg, 2000,* p. 91.
5. M. A. Isakovich, *General Acoustics* (Nauka, Moscow, 1973).
6. Yu. S. Yakovlev, *Hydrodynamics of Explosion* (Sudpromgiz, Moscow, 1961).

Translated by P. Pozdeev

Technical Physics Letters, Vol. 28, No. 8, 2002, pp. 642–644. Translated from Pis'ma v Zhurnal Tekhnicheskoĭ Fiziki, Vol. 28, No. 15, 2002, pp. 48–54.
Original Russian Text Copyright © 2002 by Stepanov, Bour, Reinholdt, Kreibig.

The Formation of Hydrogenated Yttrium Nanoparticles

A. L. Stepanov[a,b,*], G. Bour[a], A. Reinholdt[a], and U. Kreibig[a]
[a] *Institute of Physics 1, Aachen Technical University, 52056 Aachen, Germany*
[b] *Kazan Physicotechnical Institute, Russian Academy of Sciences, Kazan, Tatarstan, 420029 Russia*
* *e-mail: stepanov@physik.rwth-aachen.de*

Received February 11, 2002

Abstract—Nanoparticles of yttrium (Y) and YH_{3-x} (with the composition varying from $x < 1$ to $x \ll 1$) and the chemical reactions of these particles with hydrogen ($YH_2 \longleftrightarrow YH_3$) were studied. Yttrium nanoparticles with an average size of ~25 nm were synthesized by method of laser ablation in an argon atmosphere. The particles deposited onto quartz substrates were exposed to H_2 at room temperature and various pressures. The phase composition of the hydrogenated nanoparticles was determined by optical density measurements *in situ*. In the initial stage (low H_2 pressures), the interaction of yttrium with hydrogen leads to the formation of stable metal-like YH_2 dihydride nanoparticles. As the hydrogen pressure increases, the YH_2 particles transform into dielectric nanoparticles with the composition YH_{3-x}. The reaction $YH_2 \longleftrightarrow YH_3$, corresponding to the metal–dielectric phase transition in the nanoparticles, is reversible with respect to the H_2 pressure in the gas phase. *© 2002 MAIK "Nauka/Interperiodica".*

Occupying an intermediate position between molecular forms and bulk materials, nanoparticles (or clusters) are of interest for many fields of basic science and in numerous applications. Of special importance are problems related to variation of the physicochemical properties of particles with increasing number of atoms and/or to the influence of the interface between a nanoparticle and the surrounding medium [1].

This investigation was aimed at the synthesis and characterization of nanosystems of a new type based on metallic yttrium nanoparticles. Such Y particles are difficult to obtain by traditional methods (including sputtering in vacuum, ion implantation, etc.) because of a relatively high melting temperature of yttrium (150°C) and an extremely high susceptibility of this metal to oxidation. Of special interest is a high activity of metallic yttrium with respect to molecular hydrogen, which was observed in bulk Y samples (see, e.g., [2, 3]). The unique properties of yttrium stimulated our work on the synthesis of Y nanoparticles and the study of the properties of hydrogenated nanoparticles.

Yttrium nanoparticles were synthesized in a high-vacuum setup of the Lucas type [4] capable of generating beams of clusters or nanoparticles. The system was upgraded and equipped with a pulsed Nd:YAG laser (Lumonics JK 702H) operating at a wavelength of 1.064 nm in the IR range. The nanoparticles were obtained by laser ablation of a bulk chemically pure yttrium target mounted in the source chamber of the high-vacuum setup filled with Ar to a pressure of 0.6 bar. The target was ablated by 500 identical laser pulses with an energy density of ~4.7 J/cm^2, a pulse duration of 1 ms, and a repetition frequency of 80 Hz. The beam of Y nanoparticles was directed to and deposited onto quartz substrates or thin carbon films. The latter samples were intended for investigation in a Philips EM 400T transmission electron microscope (TEM).

The as-deposited Y nanoparticles were exposed from 30 min to several hours to an H_2 atmosphere at room temperature and various pressures (from 3×10^{-6} to 5 mbar). In order to provide for the chemical reaction *in situ* between hydrogen atoms and Y nanoparticles in the vacuum chamber, the samples were coated (by the electron-beam deposition technique) with a thin Pd film (~0.3 nm thick) catalyzing the formation of atomic (H_1) species from molecular hydrogen (H_2) filling the chamber. The phase compositions of the hydrogenated nanoparticles were determined by measuring the optical density of samples *in situ*, which offers the most rapid nondestructive method [4]. These measurements were performed at room temperature in a wavelength range from 250 to 1000 nm using a single-beam optical fiber setup based on an MSC 400 (Karl Zeiss) spectrometer. The electric resistance of a sample composed of hydrogenated Y nanoparticles was also determined *in situ* by a standard four-point-probe technique using gold contacts spaced by 4.5 mm and a Keithley 236 ammeter capable of controlling currents in the range from femto- to nanoamperes at a voltage of 1 V.

Figure 1 shows a typical electron micrograph of Y nanoparticles. The average size of spherical particles was ~25 nm. As was experimentally established, the chemical reaction of Y nanoparticles with hydrogen did not lead to a significant change in the nanoparticle dimensions. Figure 2 presents the optical density spectra measured before and after the exposure of Y particles to an H_2 atmosphere. The presence of a thin Pd film did not influence the original optical spectra of Y nanoparticles. Previously, the types of crystal structures corresponding to yttrium metal and hydride phases were determined by the X-ray diffraction study of the surface of thick Y films hydrogenated in an H_2 atmosphere [5]. The same hydrogenated yttrium films were characterized by dielectric constants. These data, together with the optical constants borrowed from [6], were used previously for calculating the optical extinction spectra of Mie resonances [7] corresponding to Y and YH_{3-x} nanoparticles of various phase compositions (from $x < 1$ to $x \ll 1$) [4].

Based on the calculated data, the broad selective band observed in this study with a maximum at 370 nm (Fig. 2, curve *1*) can be attributed to Y nanoparticles. As is known [5], the exposure of thick Y films in H_2 at a low pressure (~10^{-5} mbar) leads to the appearance of particles of a new phase representing the yttrium hcp lattice with fcc interstitials filled by hydrogen atoms diffusing through the Pd film. This corresponds to the formation of yttrium dihydride (YH_2) with an fcc lattice. In agreement with our recent calculations [4], the very small particles of the YH_2 phase (see Fig. 2, curve *2*) are characterized by two separate optical resonance peaks (380 and 965 nm) which are significantly narrower than peaks in the spectra of Y particles. The YH_2 nanoparticles exhibit metallic properties and possess a stable structure. When the H_2 pressure decreases, the optical spectrum presented in Fig. 2 (curve *2*) remains unchanged, thus showing that the phase composition is not subjected to transformations. Similar to the case of bulk yttrium, the chemical reaction $Y \longleftrightarrow YH_2$ observed in the system studied is irreversible. The light reflection from deposited YH_2 particles is characterized by a characteristic metallic luster.

According to the results of investigations of the bulk yttrium films [5], an increase in the H_2 pressure (in our experiments, up to ~1 mbar) leads to a change in the phase composition of samples. This corresponds to the formation of yttrium dihydride nanoparticles of YH_{3-x} with the composition varying from $x < 1$ to $x \ll 1$ and a crystal structure comprising hydrogen atoms occupying interstitial positions in the hcp lattice of YH_2. This was accompanied by the loss of metallic luster in the light reflection picture. The optical density spectrum of $YH_{\sim 3}$ nanoparticles with an hcp structure (Fig. 2, curve *3*) is typical of a system of small dielectric particles [7], being characterized by the absence of selective bands in the visible range and by a monotonic growth of absorption in the UV range.

It was found that a special feature of the chemical reaction $YH_2 \longleftrightarrow YH_3$, corresponding to the metal–dielectric phase transition in the nanoparticles, is reversibility with respect to H_2 pressure at room temperature. This effect was manifested by reversible variation of the optical spectra in Fig. 2 (from curve *2* to *3* and vice versa) in response to the multiply repeated cycles of increasing and decreasing hydrogen pressure in the experimental setup. The phenomenon of reversible phase composition changes and the metal–dielectric phase transition in hydrogenated yttrium nanoparti-

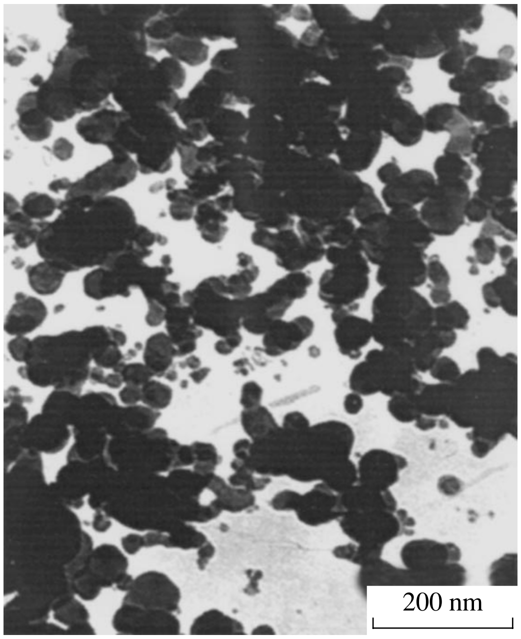

Fig. 1. TEM micrograph of as-synthesized yttrium nanoparticles.

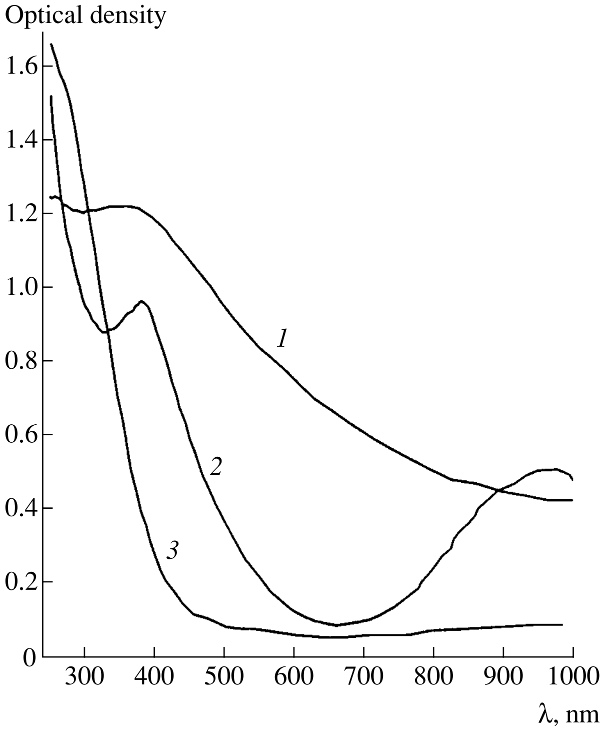

Fig. 2. Optical density spectra measured *in situ* from the samples of (*1*) Y, (*2*) YH_2, and (*3*) YH_3 nanoparticles.

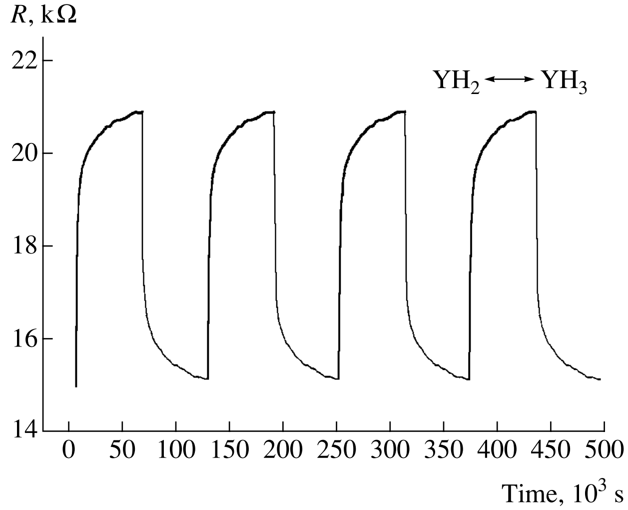

Fig. 3. Cyclic changes in the resistance of a sample containing Y nanoparticles in response to the hydrogen pressure variation: thick ascending curves correspond to an increase in the H_2 pressure (to 10 mbar); thin descending curves reflect subsequent evacuation of the working chamber (to 10^{-6} mbar).

cles in the hydrogen pressure cycles was also confirmed by the measurements of electric conductivity. As an example, Fig. 3 shows the cycles of increase in the resistance of a film of Y nanoparticles exposed to increasing hydrogen pressure, followed by recovery of the initial resistance level upon evacuation of the working chamber.

Thus, we have synthesized (by laser ablation) yttrium nanoparticles and experimentally investigated (by optical absorption spectroscopy) the effect of hydrogen pressure on the phase composition of hydrogenated yttrium particles. It was established that the chemical reaction $YH_2 \longleftrightarrow YH_3$ in the nanoparticles is reversible. This is a promising phenomenon from the standpoint of applied model investigations and the creation of optical and/or electrical hydrogen sensors, since the observed reversible phase transition is accompanied by transformation of the optical spectrum from the pattern of absorption to transparency in the visible rage and by variation of the electric conductivity. Composite materials containing nanoparticles possess important advantages over thick brittle films of yttrium [5]. The advantages include a more developed surface of nanoparticles (increasing the efficacy of interaction with hydrogen) and higher stability with respect to mechanical stresses and fracture. The latter is related to the fact that the $YH_2 \longleftrightarrow YH_3$ transition is accompanied by variation of the crystal lattice parameter to within 14%.

Acknowledgments. A.L.S is grateful to the Alexander Humboldt Foundation for the financial support of his work in Germany, and G.B. is grateful to the European Community for the grant from TMR CLUPOS.

This study was also supported by the Russian Foundation for Basic Research, project nos. 99-02-17767 and 00-15-96615.

REFERENCES

1. A. L. Stepanov and D. E. Hole, in *Resent Research and Developments in Applied Physics*, Ed. by Pandalai (Transworld Research Network, Kerala, 2001).
2. M. Gurvitch, L. Manchanda, and J. M. Gibson, Appl. Phys. Lett. **51**, 919 (1987).
3. J. N. Huiberts, R. Griessen, J. H. Rector, *et al.*, Nature **380**, 21 (1996).
4. G. Bour, A. Reinholdt, A. L. Stepanov, *et al.*, Eur. Phys. J. B **16**, 219 (2001).
5. J. N. Huiberts, J. H. Rector, R. J. Wijngaarden, *et al.*, J. Alloys Compd. **239**, 158 (1996).
6. M. Gartz and M. Quinten, Appl. Phys. B **73**, 327 (2001).
7. U. Kreibig and M. Vollmer, *Optical Properties of Metal Clusters* (Springer-Verlag, Berlin, 1995).

Translated by P. Pozdeev

Technical Physics Letters, Vol. 28, No. 8, 2002, pp. 645–647. Translated from Pis'ma v Zhurnal Tekhnicheskoĭ Fiziki, Vol. 28, No. 15, 2002, pp. 55–60.
Original Russian Text Copyright © 2002 by Kirichenko, Martynyuk, Motornenko, Skuratovskii, Suvorova.

A Spherical Microwave Discharge Induced at Atmospheric Pressure

A. Ya. Kirichenko, S. P. Martynyuk, A. P. Motornenko,
I. G. Skuratovskii, and O. A. Suvorova
Usikov Institute of Radiophysics and Electronics, National Academy of Sciences of Ukraine, Kharkov, Ukraine
e-mail: briz@ire.kharkov.ua

Received February 19, 2002

Abstract—A discharge induced at the end of an antenna in a flow of argon outgoing into the free space in a coaxial microwave plasmatron is described. Increased energy density supplied to the plasma leads to structuring of the microwave discharge. Effects of the antenna geometry, supplied power, and argon flow rate on the discharge structure are studied. *© 2002 MAIK "Nauka/Interperiodica".*

In recent years, the attention of researchers engaged in microwave discharges is drawn to the features of discharge structure formation. The main effort is devoted to establishing the conditions of existence and classification of the structures, monitoring the structure development in pulsed gas-discharge sources operating at medium and high gas pressures, and studying the physical mechanisms responsible for the particular structure formation [1–4].

The results of recent investigations [5, 6] showed that quite various structures may form in stationary discharges as well. A ball electrode microwave discharge [5], observed at the antenna end in a large-size metal discharge chamber filled with hydrogen at a pressure of 1–15 Torr, was formed under the action of 2.45-GHz microwave radiation with a power of up to 2.5 kW. A column microwave discharge (comprising one to seven filaments) [6] was observed at an argon pressure of 0.05–1 atm in a gas discharge tube in a waveguide excited at a continuous microwave power of 50–500 W at a frequency of 7 GHz.

It was established that, using a new variant of the well-known coaxial microwave plasmatron usually featuring a stationary torch discharge [7, 8], a structured discharge can be observed under certain conditions even at atmospheric pressure. Below we report on the results of the investigation of a microwave discharge induced at the end of a thin cylindrical antenna (representing a continuation of the internal conductor of a coaxial microwave plasmatron) in a flow of argon streamlining the antenna and freely outgoing into the surrounding space.

The experiments were performed with a microwave plasmatron pumped by a continuous 10-GHz magnetron with a power of up to 12 W, isolated from the plasma generator by a ferrite cicrculator [7, 8]. The plasmatron represented essentially a coaxial waveguide resonator loaded on a 10 × 23 mm rectangular waveguide. The waveguides were matched with the aid of a T-coupler and adjusted by selecting the position of a waveguide short-circuit plunger. Diameters of the inner and outer coaxial conductors were 4.3 and 10 mm, respectively. The coaxial section terminated with a gas nozzle. The gas (argon) was supplied to a discharge zone via the channel between conductors. The argon flow rate was controlled within 0.3–3 l/min. In contrast to the system used previously [7, 8], the internal conductor of the coaxial plasmatron ended with an antenna made of a copper wire with a diameter of 0.2–0.65 mm.

The microwave discharge was initiated at the end of the antenna by inducing a short spark between the inner and outer coaxial conductors. As a rule, a torch discharge appeared at the antenna end (sometimes resembling Saint Elmo's fire observed in a static field of atmospheric electricity), provided a certain level of the supplied microwave power and the argon flow rate. Figure 1a shows a photograph of the torch discharge induced at the antenna end for a supplied microwave power of P_0 = 5.3 W and an argon flow rate of v = 2 l/min. Three zones usually observed in a high-frequency torch could be readily distinguished in the discharge, including (i) a thin, bright, near-electrode zone; (ii) the central discharge column; and (iii) a less bright torch shell. The torch length could be controlled by changing the supplied power, gas flow rate, and the length of the antenna part protruding above the nozzle output cross section. Note that a torch of an analogous shape is usually formed as a continuation of the inner coaxial conductor even in the absence of the protruding antenna [7].

It was found that there are certain intervals of the supplied microwave power and argon flow rate in which the discharge exhibited structuring. Figures 1b–1d illustrate the effect of variable supplied microwave power on the discharge character observed for an argon flow

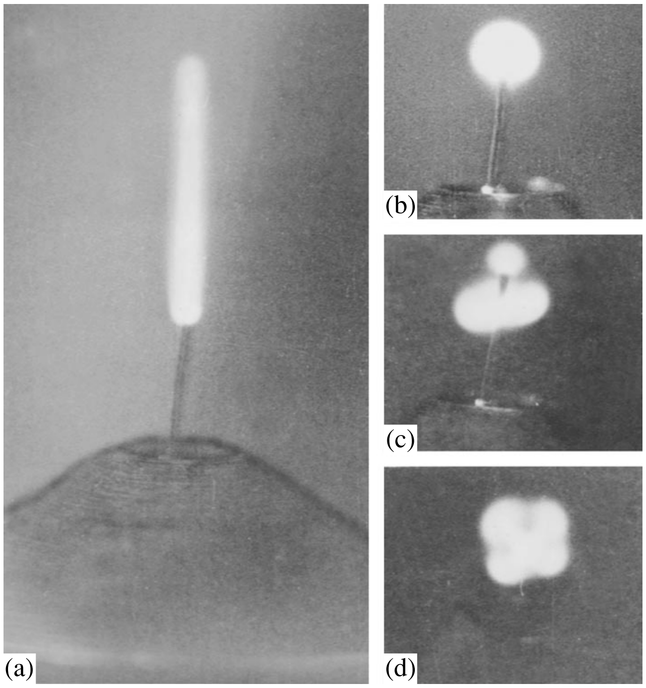

Fig. 1. Photographs illustrating the microwave discharge structures (see the text for explanations).

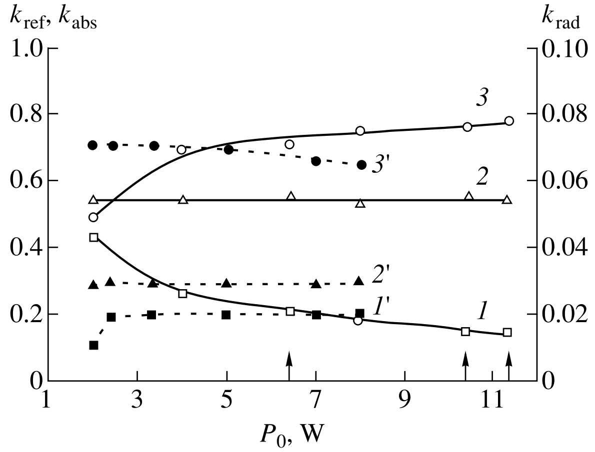

Fig. 2. Energy characteristics of the microwave discharge: the plots of (*1*, *1*') reflection coefficient k_{ref}; (*2*, *2*') radiation coefficient k_{rad}; and (*3*, *3*') absorption coefficient k_{abs} versus supplied microwave power P_0 for (*1*–*3*) a structured and (*1*'–*3*') usual torch discharge (see the text for explanations).

rate fixed at 0.5 l/min (all pictures are in the same scale). The photographs in Figs. 1a–1c were made with a camera oriented perpendicularly to the antenna axis, while in Fig. 1d the camera was inclined at 15° to this axis.

When the argon flow rate was reduced from 2 to 0.5 l/min, the length of the torch decreased as compared to that in Fig. 1a and eventually the discharge appeared as a small bright ball "pinned" on the antenna. As the supplied power is then also decreased, the ball diameter monotonically decreases until the discharge is quenched. If, on the contrary, the microwave power is increased from 5.3 to 6.4 W, the ball becomes more deeply pinned on the antenna, the end of which reaches the ball center (Fig. 1b).

On further increasing the power to P_0 = 10.4 W, the character of the discharge exhibits a jumplike change to acquire the structure depicted in Fig. 1c. Here, besides a ball discharge of decreased diameter pinned on the antenna end, a structured plasma formation appears closer to the nozzle output cross section. This new structure comprises several bright spheres arranged around the antenna, inscribed into a toroid with the axis coinciding with the antenna. The diameters of these spheres are somewhat smaller than that of the single ball in Fig. 1b. The distance from the additional spheres to the end ball increases with decreasing argon flow rate. As the supplied power keeps growing, the number of spheres inscribed in the toroid increases within the framework of a strictly symmetric pattern. As an example, Fig. 1d shows a plasma formation comprising four such spheres observed at a supplied power of 11.4 W.

The energy characteristics of a structured microwave discharge were studied using conventional microwave techniques (polarization attenuators, directed couplers, sectioned detectors, etc.). Figure 2 shows plots of the coefficients of reflection (k_{ref}), radiation (k_{rad}), and absorption (k_{abs}) versus supplied power P_0 for a structured discharge at an argon flow rate of 0.5 l/min (curves *1*–*3*, respectively). The arrows indicate the threshold values of P_0 corresponding to the discharge structures presented in Figs. 1b–1d. For comparison, the dashed curves *1*'–*3*' in Fig. 2 show analogous plots measured in a usual microwave plasmatron without a terminal antenna. On the side of large supplied powers, curves *1*'–*3*' are limited by the breakdown between inner and outer coaxial conductors.

The values of k_{rad} were determined using directivity patterns of the microwave plasmatrons with the antenna preliminarily measured without discharge and with a discharge under the conditions corresponding to Fig. 2. In all cases presented in Figs. 1b–1d, the directivity pattern remained virtually unchanged, resembling that of an asymmetric quaterwave dipole. The power balance was calculated with neglect of the ohmic losses in the resonator and antenna.

Based on the experimental data obtained, we may draw the following conclusions. Similarly to [6], where an increase in the supplied power led to an increase in the number of filaments in the discharge column, the microwave power growing in our system was accompanied by a jumplike increase in the number of spherical plasma formations. However, values of the reflection, radiation, and absorption coefficients changed rather slightly. In contrast to what was reported in [5], the size of plasma spheres in our case decreased with increasing power (see Fig. 1), which is probably related to the higher (atmospheric) gas pressure used in our experiments.

The absorption coefficient of our structured discharge (Fig. 2), while being on the same order of magnitude as that of a torch discharge in the usual plasmatron, slightly increases with the supplied power. Note that, although the presence of the end antenna increases the radiation coefficient by a factor of about three, this value is still small (below 6%).

It should be also noted that, according to our experimental observations, the characteristic microwave discharge shapes are retained upon changing the orientation of the "elmotron" nozzle axis (upward to downward) at a fixed pumping regime, which is evidence of an electrodynamic nature of the discharge structure formation.

According to Fig. 2, the absorption coefficients of the torch and spherical discharges approximately coincide. Then, using the recent data [9], we may conclude that the electron density established in the microwave elmotron discharge makes possible the surface wave formation. Our estimates showed that the electromagnetic energy density (per unit volume) in a spherical discharge may exceed that in the torch, while the discharge sphere radius approximately corresponds to the skin layer thickness. A qualitative agreement between our results and the data reported in [6] allows us to conclude, despite a difference between the discharge structures (filament versus sphere), that mechanisms of the discharge structure formation are similar, since the shape and dimensions of the plasma formations are determined by the maximum deposited microwave power.

REFERENCES

1. V. G. Brovkin and Yu. F. Kolesnichenko, Pis'ma Zh. Tekh. Fiz. **17** (1), 58 (1991) [Sov. Tech. Phys. Lett. **17**, 22 (1991)].
2. A. L. Vikharev, A. M. Gorbachev, A. V. Kim, *et al.*, Fiz. Plazmy **18** (8), 1064 (1992) [Sov. J. Plasma Phys. **18**, 554 (1992)].
3. L. P. Grachev, I. I. Esakov, G. I. Mishin, *et al.*, Zh. Tekh. Fiz. **64** (1), 74 (1994) [Tech. Phys. **39**, 40 (1994)].
4. L. P. Grachev, I. I. Esakov, G. I. Mishin, *et al.*, Zh. Tekh. Fiz. **66** (7), 32 (1996) [Tech. Phys. **41**, 652 (1996)].
5. L. Bardosh and Yu. A. Lebedev, Zh. Tekh. Fiz. **68** (12), 29 (1998) [Tech. Phys. **43**, 1428 (1998)].
6. A. A. Skovoroda and A. V. Zvonkov, Zh. Éksp. Teor. Fiz. **119** (1), 91 (2001) [JETP **92**, 78 (2001)].
7. S. P. Martynyuk, A. P. Motornenko, and A. Ya. Usikov, Dokl. Akad. Nauk Ukr. SSR, Ser. A, No. 8, 734 (1975).
8. S. P. Martynyuk and A. P. Motornenko, Dokl. Akad. Nauk Ukr. SSR, Ser. A, No. 2, 161 (1978).
9. A. P. Motornenko and K. Schunemann, Int. J. Electron. Commun. **55** (5), 337 (2001).

Translated by P. Pozdeev

Technical Physics Letters, Vol. 28, No. 8, 2002, pp. 648–651. Translated from Pis'ma v Zhurnal Tekhnicheskoĭ Fiziki, Vol. 28, No. 15, 2002, pp. 61–68.
Original Russian Text Copyright © 2002 by Koronovskiĭ, Khramov.

Variation of the Dependence of the Transient Process Duration on the Initial Conditions in Systems with Discrete Time

A. A. Koronovskiĭ[a],* and A. E. Khramov[b]
[a] *Saratov State University, Saratov, Russia*
** e-mail: alkor@cas.ssu.runnet.ru*
[b] *State Scientific Center "College," Saratov, Russia*

Received February 11, 2002

Abstract—Dependence of the transient process duration on the initial conditions is considered in one- and two-dimensional systems with discrete time, representing a logistic map and the Eno map, respectively. It is shown that dependence of the transient process duration on the initial conditions for a cycle of period 1 is determined by multiplicators of a stable immobile point. A change in the control parameters within the same dynamical regime results in bifurcation leading to a qualitative change in the above dependence. *© 2002 MAIK "Nauka/Interperiodica".*

In the past decades, considerable attention of researchers has been devoted to the investigation of nonlinear dynamical systems, both with discrete and continuous time. As a rule, the effort is concentrated on studying established regimes and on determining how one dynamical regime is changed by another in response to variations of the control parameters. At the same time, there are many phenomena related to the transient processes that frequently remain unstudied despite the fact that such processes can provide information about the whole system and about attractors realized in the phase space [1, 2].

Previously [3], we have studied transient processes in a one-dimensional (1D) system with discrete time, representing a logistic map:

$$x_{n+1} = f(x_n) = \lambda x_n(1 - x_n). \quad (1)$$

In particular, it was demonstrated that dependence of the transient process duration on the initial conditions $T_\varepsilon(x_0)$ for this logistic map qualitatively changes when the control parameter λ varies and one dynamical regime is changed by another. It was also shown that dependence of the transient process duration on the initial conditions obeys certain scaling laws.

In this study, we will consider the mechanisms leading to a qualitative change in the type of dependence of the transient process duration on the initial conditions in the case when the control parameters of a system vary within the framework of the same dynamical regime. The investigation is performed for a logistic map (1), which is a standard object of nonlinear dynamics, and the Eno map [4, 5],

$$\begin{aligned} x_{n+1} &= \lambda x_n(1 - x_n) + b y_n, \\ y_{n+1} &= x_n, \end{aligned} \quad (2)$$

which transforms into a logistic map for $b = 0$. The transient processes in systems (1) and (2) were studied in the simplest regime offered by a stable cycle of period 1. In other words, the control parameters were varied in such a manner that all observations were referred to this dynamic regime, in which the behavior of system (2) corresponds to an immobile stable point (x^0, y^0), $x^0 = y^0 = (\lambda + b - 1)/\lambda$, and the behavior of map (1), to an immobile stable point $x^0 = (\lambda - 1)/\lambda$.

Dependence of the transient process duration on the initial conditions, $T_\varepsilon(x_0)$ in the logistic map (1) and $T_\varepsilon(x_0, y_0)$ in the Eno map (2), was determined for the given initial conditions and preset accuracy ε using the same method as in [3]. First, an attractor realized in the system was determined for a fixed set of the control parameters by $N = 6500$ iterations of an arbitrary initial point, after which it was assumed that the imaging point attained the attractor. Then, the obtained sequence ($\{x_n\}|_{n=0}^{N}$ and $\{x_n, y_n\}|_{n=0}^{N}$ for maps (1) and (2), respectively) was analyzed beginning with $n = N - 1$, $N - 2$, … in order to determine the period of the regime (stable point, 2-cycle, 4-cycle, etc.). Finally, by sequentially trying all possible initial conditions with a certain partition step, an interval of the discrete time necessary for the imaging point to attain the attractor with an accuracy ε was determined for each initial condition.

The results of this investigation showed that dependence of the transient process duration on the initial conditions $T_\varepsilon(x_0)$ for the logistic map exhibits a qualitative change when the control parameter λ varies even within the framework of the same dynamical regime. Figures 1a and 1b show the behavior of the transient process duration $T_\varepsilon(x_0)$ for two values of the control parameter: $\lambda = 1.2$ and 2.8, respectively. The system behavior in both cases corresponds to the immobile stable point $x_0 = (\lambda - 1)/\lambda$. A change in type of the function $T_\varepsilon(x_0)$ takes place when the control parameter λ passes

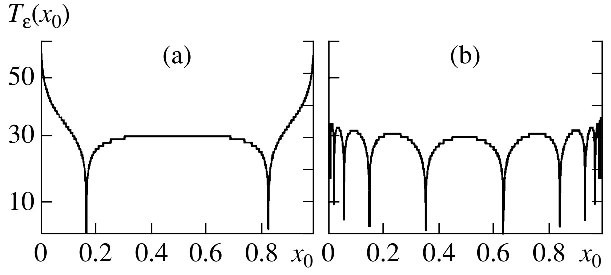

Fig. 1. Plots of the transient process duration $T_\varepsilon(x_0)$ as a function of the initial conditions for a cycle of period 1 of the logistic map (1) for two values of the control parameter: $\lambda = 1.2$ (a) and 2.8 (b).

through the value $\lambda_m = 2$, where the cycle of period 1 possesses maximum stability and the corresponding multiplicator is $\mu = 0$. For $\lambda < \lambda_m$, the function $T_\varepsilon(x_0)$ exhibits two local minima, while for $\lambda > \lambda_m$, the number of such local minima becomes infinite (Fig. 1).

A mechanism of this change in the type of dependence of the transient process duration on the initial conditions is related to the appearance of two sequences of points, $\{x_i^{(0)}\}\big|_{i=1}^{\infty}$ and $\{x_i^{(1)}\}\big|_{i=1}^{\infty}$, which are imaged after a finite number of iterations by an immobile stable point x^0 such that

$$x^0 = f(x_1^{(0)}) = f(f(x_2^{(0)})) = f(f(x_2^{(1)})) \\ = \ldots = f^{(n)}(x_n^{(0)}) = f^{(n)}(x_n^{(1)}). \tag{3}$$

These sequences converge to the points on the boundaries of the basin of attraction for the given attractor, $x_{gr0} = 0$ and $x_{gr1} = 1$, respectively, and each point in the sequence corresponds to a local minimum in the dependence of the transient process duration on the initial conditions (see also [3]). These sequences arise for $\lambda > \lambda_m$ and are related to the irreversibility of map (1).

As noted above, the Eno map (2) transforms for $b = 0$ into the logistic map (1). Therefore, the Eno map with $b = 0$ and $\lambda = 1$–3 must exhibit, within the framework of a stable cycle of period 1, a change in the type of dependence of the transient process duration on the initial conditions $T_\varepsilon(x_0, y_0)$, as is characteristic of the logistic map. In this case, the corresponding dependence $T_\varepsilon(x_0)$ for the logistic map is simply translated along the y axis so that the local minima in the dependence of the transient process duration on the initial conditions pass by the lines parallel to the y axis on the

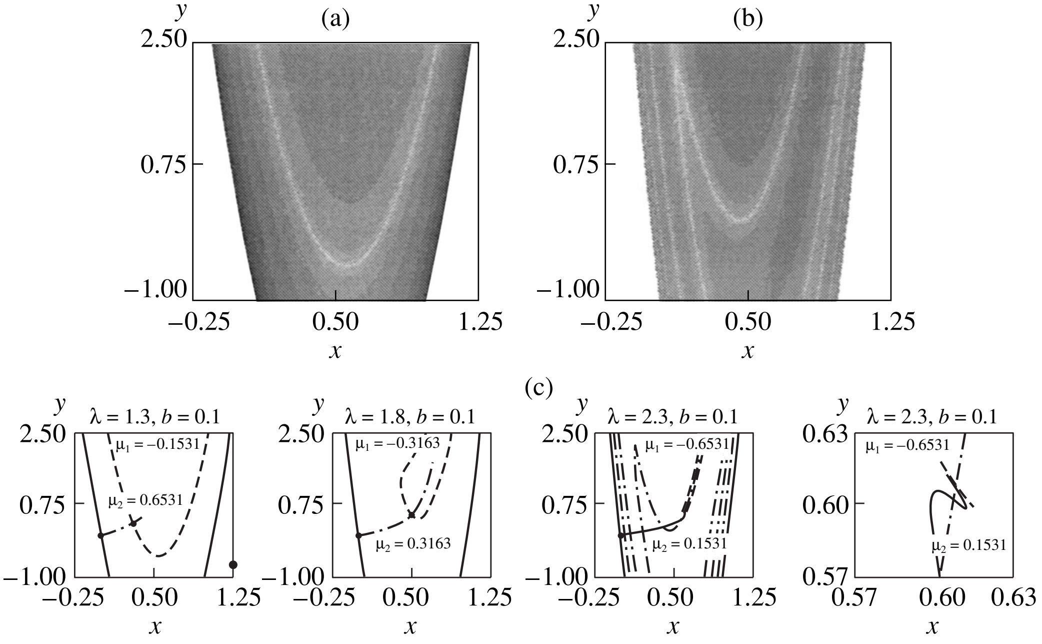

Fig. 2. (a, b) Projection of the surface $T_\varepsilon(x_0, y_0)$, representing the transient process duration as a function of the initial conditions, on the plane of possible states (x, y) for the Eno map with $b = 0.1$ and $\lambda = 1.3$ and 2.3, respectively. Variations in the transient process duration are reflected by the gray color gradations: from white (corresponding to $T = 0$) to black (corresponding to $T = 50$ units of discrete time). The light-gray shade outside the basin of attraction of the attractor (x^0, y^0) corresponds to the initial conditions with an attractor at infinity. (c) Schematic diagrams showing stable manifolds of the attractor point (x^0, y^0) and the stable and unstable manifolds of the unstable point (0, 0) for a fixed value of the control parameter ($b = 0.1$) and different values of the parameter λ. For the point (x^0, y^0), stable manifolds are depicted by the dashed curve for a negative multiplicator μ_1 and by the dot-dash curve for a positive multiplicator μ_2 (the values of μ_1 and μ_2 are indicated at the curves). Solid curves show the manifolds for the unstable point (0, 0). The last diagram shows a magnified fragment of the previous diagram, refining the behavior of the unstable manifold of the point (0, 0) in the vicinity of the attractor (x^0, y^0).

plane of the initial conditions (x_0, y_0). This phenomenon is also observed in the Eno map for the values of the control parameter b close (but not equal) to zero (Fig. 2). The appearance of a nonzero term by_n in Eq. (2) results in that the lines corresponding to minima of the $T_\varepsilon(x_0, y_0)$ function are no longer parallel.

At the same time, it is not possible to explain the mechanism of complication of the dependence of the transient process duration on the initial conditions $T_\varepsilon(x_0, y_0)$ in the same way as was done above for the logistic map. This is related, first, to the fact that the Eno map with $b \neq 0$ is reversible and, hence, there are no points imaged by an immobile point (x^0, y^0) after a finite number of iterations.[1] However, it was precisely the existence of such points that accounted for the appearance of the infinite number of local minima of the $T_\varepsilon(x_0)$ function for the logistic map.

Second, in the Eno map with $b \neq 0$, the multiplicators $\mu_{1,2}$ of an immobile point (x^0, y^0) do not take zero values and, accordingly, the Eno map (with $b \neq 0$) possesses no cycles of maximum stability. However, the bifurcation in dependence of the transient process duration $T_\varepsilon(x_0)$ on the initial conditions for the logistic map was related precisely to the cycle of maximum stability. Therefore, the Eno map leads to the problem of finding a bifurcation line on the plane of control parameters (λ, b), the crossing of which results in complication of the shape of the $T_\varepsilon(x_0, y_0)$ function.

Let us compare the projection of the $T_\varepsilon(x_0, y_0)$ surface onto the plane of initial conditions (x_0, y_0) to the arrangement of stable manifolds of a stable immobile point (x^0, y^0). Such manifolds play an important role, for example, in the formation of boundaries of the basins of attraction for attractors [6, 7]. This comparative analysis shows that the points of initial conditions for which the transient process duration is minimum coincide with the points of one of the manifolds. A stable immobile point (x^0, y^0) is characterized by the multiplicators $\mu_1 = (2 - 2b - \lambda - \sqrt{4b + (-2 + 2b + \lambda)^2})/2$ and $\mu_2 = (2 - 2b - \lambda + \sqrt{4b + (-2 + 2b + \lambda)^2})/2$, as well as by the corresponding eigenvectors $\mathbf{e}_1 = (2 - 2b - \lambda - \sqrt{4b + (-2 + 2b + \lambda)^2})/2$ and $\mathbf{e}_2 = (2 - 2b - \lambda + \sqrt{4b + (-2 + 2b + \lambda)^2})/2$.

Minimum values of the function $T_\varepsilon(x_0, y_0)$ are attained at that manifold of the point (x^0, y^0) which corresponds to the minimum value of multiplicator. This manifold provides for the most rapid approach of the imaging point to the attractor. Variation of the control parameter λ from 0.9 to 2.7 at a fixed value of the control parameter $b = 0.1$ (whereby behavior of the system corresponds to a stable cycle of period 1) leads to a gradual decrease of the value of the positive multiplicator μ_2 and an increase in the absolute value of the negative multiplicator μ_1. For $b = 0.1$ and $\lambda < \lambda_{eq} = 1.8$, the system is characterized by $|\mu_1| < |\mu_2|$ and, accordingly, the minima in the dependence of the transient process duration on the initial conditions (represented by light bands in Fig. 2a) correspond to a manifold characterized by the negative multiplicator μ_1. At $\lambda = \lambda_{eq} = 1.8$, the multiplicators are equal $(|\mu_1| = |\mu_2|)$ and the two manifolds become "equivalent." For $\lambda > \lambda_{eq} = 1.8$, we obtain $|\mu_2| < |\mu_1|$ and the manifold change in their roles: the light bands of minimum values of the transient process durations correspond to the manifold characterized by a positive multiplicator μ_2 (Fig. 2b).

Thus, the control parameters $b = 0.1$, $\lambda = 1.8$ correspond to a situation when the stable manifolds of an immobile stable point (x^0, y^0) "change their roles." However, the same values of the control parameters correspond to another important event, involving an unstable manifold of the unstable point (0, 0). Note that a stable manifold of this point, characterized by the multiplicator $\mu_1^{unst} = (\lambda - \sqrt{4b + \lambda^2})/2$ and the eigenvector $\mathbf{e}_1 = (\lambda - \sqrt{4b + \lambda^2})/2$, forms a boundary of the basin of attraction of the attractor (x^0, y^0). The unstable manifold of the point (0, 0) is characterized by the multiplicator $\mu_2^{unst} = (\lambda + \sqrt{4b + \lambda^2})/2$ and the eigenvector $\mathbf{e}_2 = (\lambda + \sqrt{4b + \lambda^2})/2$. Since any point occurring in a small vicinity of the unstable point (0, 0) but belonging to the basin of attraction of the attractor (x^0, y^0) must be attracted to the latter with time, the unstable manifold of the unstable point (0, 0) must terminate at the point (x^0, y^0) (or at least pass through this point).

As noted above, for $\lambda < \lambda_{eq} = 1.8$, the dominating role is played by a manifold corresponding to the negative multiplicator μ_1. It is this manifold on which the most rapid approach to the attractor takes place. Therefore, the unstable manifold of the point (0, 0) tends to the attractor along the second manifold of the point (x^0, y^0) characterized by the multiplicator μ_2 (Fig. 2c). When the control parameter λ exceeds the value λ_{eq}, the behavior of the unstable manifold of the point (0, 0) in the vicinity of the point (x^0, y^0) is determined by a manifold with the negative multiplicator μ_1. As a result, the unstable manifold of the point (0, 0) crosses an infinite number of times the stable manifold of (x^0, y^0) characterized by the positive multiplicator μ_2. Therefore, the stable manifold of the point (x^0, y^0) also crosses an infinite number of times the unstable manifold of (0, 0) in the vicinity of this point. This leads to the appearance of an infinite number of "depressions" on the $T_\varepsilon(x_0, y_0)$ surface.

Thus, under the condition $\mu_1 = -\mu_2$ (both μ_1 and μ_2 are real), the Eno map exhibits a bifurcation of manifold splitting. This leads to a qualitative change in the

---

[1] Naturally, except the point (x^0, y^0) itself.

dependence of the transient process duration on the initial conditions.

Acknowledgments. This study was supported by the Russian Foundation for Basic Research (project nos. 01-02-17392 and 00-15-96673) and by the Scientific-Education Center "Nonlinear Dynamics and Biophysics" at Saratov State University (Grant REC-006 from the US Civilian Research and Development Foundation for Independent States of the Former Soviet Union).

REFERENCES

1. É. V. Kal'yanov, Pis'ma Zh. Tekh. Fiz. **26** (15), 26 (2000) [Tech. Phys. Lett. **26**, 656 (2000)].
2. B. P. Bezruchko, T. V. Dikanev, and D. A. Smirnov, Phys. Rev. E **64**, 036210 (2001).
3. A. A. Koronovskiĭ, D. I. Trubetskov, A. E. Khramov, and A. E. Khramova, Dokl. Akad. Nauk (2002) (in press).
4. M. Henon, in *Strange Attractors: A Collection of Papers*, Ed. by Ya. G. Sinaĭ and L. P. Shil'nikov (Mir, Moscow, 1981), p. 152.
5. A. P. Kuznetsov, S. P. Kuznetsov, and I. R. Sataev, Phys. Lett. A **164**, 413 (1994).
6. C. Grebogi and E. Ott, Phys. Rev. Lett. **50** (13), 935 (1983).
7. C. Grebogi, E. Ott, and J. A. Yorke, Phys. Rev. Lett. **56** (10), 1011 (1986).

Translated by P. Pozdeev

Technical Physics Letters, Vol. 28, No. 8, 2002, pp. 652–656. Translated from Pis’ma v Zhurnal Tekhnicheskoĭ Fiziki, Vol. 28, No. 15, 2002, pp. 69–78.
Original Russian Text Copyright © 2002 by Gladkov.

On the Theory of Elastic Scattering of Electromagnetic Waves by Atoms

S. O. Gladkov
Semenov Institute of Chemical General Physics, Russian Academy of Sciences, Moscow, Russia
e-mail: SGlad@newmail.ru

Received January 18, 2002

Abstract—A Hamiltonian describing the elastic interaction of electromagnetic radiation (EMR) with an atom is obtained using the invariant theory of perturbations in the limit of EMR wavelengths λ significantly exceeding the atom size a_0. An exact expression for the interaction amplitude is obtained, and the probability of EMR scattering on the atom is calculated. It is established that the scattering probability at large λ is proportional to the squared frequency of monochromatic EMR. It is shown that, in the limit of large wavelengths, the formula $h \sim (\omega/c)^4 v_0$ for the extinction coefficient is inapplicable and the relation $h = A\omega^2$ becomes valid, where A is a definite coefficient. *© 2002 MAIK “Nauka/Interperiodica”.*

Problems related to the interaction of a substance with electromagnetic radiation (EMR) were considered in a large number of original papers and monographs. This letter addresses a problem which is closest to the material presented in the monograph [1] and papers [2–8] devoted to various aspects of the action of strong electromagnetic fields inducing internal energy transitions in atoms. Such interactions are usually called inelastic, although, from the standpoint of a photon with the wave vector conserved upon scattering, the process can be also considered as elastic.

Let us consider the elastic scattering of a photon on an atom in the case when the interaction is not accompanied by internal transitions in the atom. In principle, this problem may appear as very similar to that of the light scattering from a finely dispersed phase in the case when a monochromatic light wavelength λ is significantly greater than the particle size d. However, despite being qualitatively similar, the two problems exhibit a very important quantitative difference.

The matter is that, as the scattered light wavelength increases, a mechanism of the EMR–atom interaction mediated by shortwave photons belonging to the far UV range begins to operate. Calculations show that the scattering probability in this case is proportional to the square of the incident photon frequency ω. It should be recalled that, for the light scattering from macroscopic particles, the analogous probability (characterized by the extinction coefficient h related to the scattering frequency $1/\tau$ via the product hc, c being the speed of light) is proportional to ω^4. Such a strong difference in behavior is explained by the purely electromagnetic nature of the EMR–atom interaction, involving fast photon exchange between the atom and the longwave EMR quanta. The two cases of light scattering are qualitatively different in the nature of the interaction: for the macroscopic scattering particles, the extinction coefficient is calculated with neglect of the microscopic structure of a particle (which leads eventually to the fourth power of frequency); on the contrary, an exact description of the EMR–atom interaction developed below takes into account the internal structure of the scatterer.

The problem will be solved using methods of the invariant theory of perturbations. First, let us describe the interaction between an atom and the electromagnetic field as

$$H_{\text{int}} = -(1/c)\int \mathbf{j}\mathbf{A}d^3x. \tag{1}$$

The current density in the atom is determined as (see [9])

$$\mathbf{j} = -(ie\hbar/2m)(\psi^*\nabla\psi - \psi\nabla\psi^*), \tag{2}$$

where e is the electron charge, m is the electron mass, $\psi = \psi(\mathbf{x}_1, \mathbf{x}_2, \ldots, \mathbf{x}_Z)$ is the wave function of the atom, and Z is the number of electrons in the atom (atomic number).

The photon wave function operator is introduced by the formula

$$\mathbf{A} = (2\pi\hbar c/V)^{1/2}\sum_{\mathbf{k},\alpha}\mathbf{e}_\alpha k^{-1/2}(c^{+}_{\mathbf{k}\alpha}e^{-i\omega t} + c^{-}_{\mathbf{k}\alpha}e^{i\omega t})e^{i\mathbf{k}\mathbf{x}}, \tag{3}$$

where $\mathbf{e}_\alpha$ is the photon polarization vector, $\omega = ck$ is the photon frequency (dispersion relation), c is the speed of light in vacuum, V is the volume of space in which the photon exists, and $c^{+}_{\mathbf{k}\alpha}$ and $c^{-}_{\mathbf{k}\alpha}$ are the operators of production and annihilation, respectively, of a photon with a wave vector $\mathbf{k}$ and polarization $\mathbf{e}_\alpha$.

Let us divide operator **A** into two parts,

$$\mathbf{A} = \mathbf{A}_0 + \mathbf{A}_1, \tag{4}$$

where

$$\begin{gathered}\mathbf{A}_0 = (2\pi\hbar c/V)^{1/2} \\ \times \sum_{0 \le k \le q/b} \mathbf{e}_\alpha k^{-1/2}(c^{+}_{\mathbf{k}\alpha}e^{-i\omega t} + c^{-}_{\mathbf{k}\alpha}e^{i\omega t})e^{i\mathbf{kx}},\end{gathered} \tag{5}$$

$$\begin{gathered}\mathbf{A}_1 = (2\pi\hbar c/V)^{1/2} \\ \times \sum_{q/b \le k \le q} \mathbf{e}_\alpha k^{-1/2}(c^{+}_{\mathbf{k}\alpha}e^{-i\omega t} + c^{-}_{\mathbf{k}\alpha}e^{i\omega t})e^{i\mathbf{kx}},\end{gathered} \tag{6}$$

q is the limiting photon wavenumber on the electromagnetic scale (approximately 10^{13} cm^{-1}), and b is a factor greater than unity.

Using the interaction function (1), the S matrix can be written in the following form [10]:

$$S = T\exp\{-i\int H_{\text{int}}(t)dt\}, \tag{7}$$

where T is the operator of ordering with respect to time, beginning with the maximum.

Obviously, the effect under consideration can be manifested only in the fourth-order perturbation theory. Therefore, expanding expression (7) into a series and retaining terms up to the order of H^4_{int}, we can write

$$\begin{gathered}S^{(4)} = (1/4!)T\iiiint H_{\text{int}}(t_1) \\ \times H_{\text{int}}(t_2)H_{\text{int}}(t_3)H_{\text{int}}(t_4)\prod_{s=1}^{4} dt_s.\end{gathered} \tag{8}$$

The interaction under consideration will be determined as

$$V = -i\hbar \lim_{t\to\infty}(S^{(4)}/t). \tag{9}$$

Substituting expressions (1), (5), and (6) into (8) and taking into account only pairwise operators $\mathbf{A}_0$ and $\mathbf{A}_1$, we obtain

$$\begin{gathered}S^{(4)} = (1/4c^4\hbar^4)T\int\Pi dt_s\int\Pi d^3x_s j_i(\mathbf{x}_1)j_k(\mathbf{x}_2)j_l(\mathbf{x}_3)j_n(\mathbf{x}_4) \\ \times A_{0i}(\mathbf{x}_1, t_1)A_{0k}(\mathbf{x}_2, t_2)A_{1l}(\mathbf{x}_3, t_3)A_{1n}(\mathbf{x}_4, t_4),\end{gathered} \tag{10}$$

where $i, k, l, n = 1, 2, 3$ (repeated indices imply summation); in writing this expression, we can take into account that there are six identical terms and replace 4! by 4.

First, let us average $S^{(4)}$ over the "fast" photon subsystem and use expression (6). The first step yields the photon Green's function

$$D_{ln}(\mathbf{x}_3, \mathbf{x}_4, t_3, t_4) = \langle T|A_{1l}(\mathbf{x}_3, t_3)A_{1n}(\mathbf{x}_4, t_4)|\rangle, \tag{11}$$

where the angle brackets denote averaging over the ground state of the shortwave photons. Substituting expression (6), we obtain

$$\begin{gathered}D_{ln}(\mathbf{x}_3, \mathbf{x}_4, t_3, t_4) = (2\pi\hbar c/V)\sum e'_{l\alpha}e''_{n\alpha}(k_3k_4)^{-1/2} \\ \times \exp(i\mathbf{k}_3\mathbf{x}_3 - i\mathbf{k}_4\mathbf{x}_4)[\langle T|c^{+}(k_3, t_3)c(k_4, t_4)|\rangle \\ + \langle T|c(k_4, t_4)c^{+}(k_3, t_3)|\rangle].\end{gathered} \tag{12}$$

The operators $\overset{+}{c}_k(t)$ and $c_k(t)$ are taken in the interaction representation, so that $\overset{+}{c}_k(t) = \overset{+}{c}_k e^{-i\omega t}$ and $c_k(t) = c_k e^{i\omega t}$, and a nonzero value of the D_{ln} function is attained only for $\mathbf{k}_3 = \mathbf{k}_4$ and $\mathbf{e}'_\alpha = \mathbf{e}''_\alpha$. It should be recalled that $\langle|\overset{+}{c}_k c_k|\rangle = 0$ and $\langle|c_k\overset{+}{c}_k|\rangle = 1$. Averaging expression (12) over polarization directions yields the factor $\langle e_{l\alpha}e_{n\alpha}\rangle = \delta_{ln}/3$, and we arrive at an intermediate result:

$$\begin{gathered}D_{ln}(\mathbf{x}_3, \mathbf{x}_4, t_3, t_4) = (2\pi\hbar c/3V)\delta_{ln} \\ \times \sum_{q/b \le k \le q} k_3^{-1}\exp[i\mathbf{k}_3(\mathbf{x}_3 - \mathbf{x}_4) - i\omega_3(t_3 - t_4)].\end{gathered} \tag{13}$$

Now, according to expression (10), we have to perform integration with respect to t_3 and t_4. Introducing the new variables $t = 1/2(t_3 + t_4)$ and $\tau = t_3 - t_4$, we obtain

$$\begin{gathered}\int_0^\infty dt_3\int_0^\infty dt_4\exp[-i\omega_3(t_3 - t_4)] \\ = \int_0^t dt\int_0^\infty d\tau\exp(-i\omega_3\tau) = t/i\omega_3.\end{gathered}$$

Taking the integrals with respect to t_1 and t_2 (which yields $1/\omega_1\omega_2$), we obtain the following expression for the interaction defined by (9):

$$\begin{gathered}V = -(\pi^2/3c^5V^2\hbar)\sum_{0 \le k', k'' \le q/b} e'_ie''_j\overset{+}{c}_{k'}c_{k''}(k'k'')^{-3/2} \\ \times \sum_{q/b \le k_3 \le q} f(k_1, k_2, k_3)/k_3^2,\end{gathered} \tag{14}$$

where

$$\begin{gathered}f(k_1, k_2, k_3) = \int\Pi d^3x_s j_{1i}j_{2s}j_{3l}j_{4l} \\ \times \exp\{i\mathbf{k}_3(\mathbf{x}_3 - \mathbf{x}_4) + i\mathbf{k}_1\mathbf{x}_1 - i\mathbf{k}_2\mathbf{x}_2\}.\end{gathered} \tag{15}$$

Taking into account that the integration in formula (15) is performed over the region of localization of the atomic wave function (the linear size of which is on the order of the atomic size a_0) where the wave vectors k_3 are large, we may conclude that $\exp\{i\mathbf{k}_3(\mathbf{x}_3 - \mathbf{x}_4)\}$ is a rapidly oscillating factor. However, integrating with respect to d^3x_1 and d^3x_2 and taking into account the condition $|k_1|$, $|k_2| < q/b$, we can assume that $\exp(i\mathbf{k}_1\mathbf{x}_1 - i\mathbf{k}_2\mathbf{x}_2) \approx 1$. Using this assumption and substituting expression (2) into formula (15) for the function f, we arrive at the following expression:

$$f(k_1, k_2, k_3) \approx f(k_3) \\ = (e\hbar/2m)^4\left[\int(\psi^*\nabla\psi - \psi\nabla\psi^*)d^3\mathbf{x}\right]^2 \\ \times\left|\int(\psi^*\nabla\psi - \psi\nabla\psi^*)\exp(i\mathbf{k}_3\mathbf{x})d^3\mathbf{x}\right|^2. \tag{16}$$

In order to evaluate the function f given by expression (16), we must integrate the wave function of an atom containing Z electrons over the whole configuration space. This implies that $d^3\mathbf{x} = \Pi d^3x_s$, where $s \in [1, Z]$. Therefore,

$$\int(\psi^*\nabla\psi - \psi\nabla\psi^*)d^3\mathbf{x} = \int\sum[\psi^*(\{\mathbf{x}_i\})\nabla_i\psi(\{\mathbf{x}_i\}) \\ - \psi(\{\mathbf{x}_i\})\nabla_i\psi^*(\{\mathbf{x}_i\})]\Pi d^3x_s, \tag{17}$$

where $\{\mathbf{x}_i\} = \mathbf{x}_1, \mathbf{x}_2, \mathbf{x}_3, \ldots, \mathbf{x}_Z$. By the physical meaning of expression (17), we can assume that the average electron momentum in the atom is $\langle|\mathbf{P}|\rangle = \hbar|\int(\psi^*\nabla\psi - \psi\nabla\psi^*)d^3\mathbf{x}|$, where $\mathbf{P} = \sum\mathbf{p}_s$. The square of the average momentum can be considered as approximately equal to the average atomic energy $\langle E\rangle$ multiplied by $2m$. Denoting $|\int(\psi^*\nabla\psi - \psi\nabla\psi^*)d^3\mathbf{x}|^2 = 8m\langle E\rangle/\hbar^2$, we obtain

$$V = \frac{\pi^2\langle E\rangle e^4\hbar}{6m^3c^5V^2a_0^2}\sum_{q/b \le k_3 \le q}\frac{F(k_3)}{k_3^2}\sum_{0 \le k', k'' \le q/b}\frac{\mathbf{e}'\mathbf{e}''c^+_{k'}c_{k''}}{(k'k'')^{3/2}}, \tag{18}$$

where F is the new dimensionless function defined as $F(k) = a_0^2|\int(\psi^*\nabla\psi - \psi\nabla\psi^*)\exp(i\mathbf{k}_3\mathbf{x})|^2$.

Formula (18) is more conveniently written using an integral with respect to k instead of the sum taken over wave vectors, which can be done by introducing the photon density of states. Replacing the term $\sum(\ldots)$ by the integral $V\int(\ldots)d^3k/(2\pi)^3 = (V/2\pi^2)\int(\ldots)k^2dk$, we obtain

$$V = -\frac{\langle E\rangle e^4\hbar}{24\pi^2m^3c^5a_0^2}\sum_{q/b \le k_3 \le q}\frac{F(k_3)}{k_3^2} \\ \times\iint\varphi(k', k'')c^+_{k'}c_{k''}dk'dk'', \tag{19}$$

where

$$\varphi(k', k'') = \mathbf{e}'\mathbf{e}''(k'k'')^{1/2}. \tag{20}$$

Finally, we have to evaluate the sum over k_3. This is conveniently performed upon replacing the sum over k_3 by an integral with respect to the energy for high-frequency photons and introducing the photon density of states as $\sum(\ldots) = (2\pi/\Delta E)\int(\ldots)d\varepsilon_3/2\pi$, where ΔE is a certain energy scatter and $d\varepsilon_3 = \hbar c dk_3$. As a result, we obtain

$$\sum F(k_3)/k_3^2 = 2\pi[(\hbar c)^2/\Delta E] \\ \times\iiint[F(\varepsilon_3, \mathbf{n})/\varepsilon_3^2](d\varepsilon_3/2\pi)(dO/4\pi),$$

where dO is the solid angle element (usually expressed as $\sin\theta d\theta d\varphi$).

Introducing the average value of F with respect to the angular variables, $\langle F(\varepsilon_3)\rangle = (1/4\pi)\int_0^\pi\int_0^{2\pi}F(\varepsilon_3, \mathbf{n})dO$, and taking into account (20), we can rewrite expression (19) as

$$V = \iint\phi(\varepsilon', \varepsilon'')c^+_{\varepsilon'}c_{\varepsilon''}d\varepsilon'd\varepsilon''/(2\pi)^2, \tag{21}$$

where $\phi(\varepsilon', \varepsilon'')$ is the amplitude of the elastic scattering of a low-frequency EMR on an atom in the range of large wavelengths ($\lambda \gg a_0$):

$$\phi(\varepsilon', \varepsilon'') = -\frac{4\pi^3\langle E\rangle e^4(\mathbf{e}'\mathbf{e}'')(\varepsilon'\varepsilon'')^{1/2}R(q)}{3m^3c^6a_0^2\Delta E}, \tag{22}$$

and

$$R(q) = \int_{\hbar cq/b}^{\hbar cq}\langle F(\varepsilon)\rangle(d\varepsilon/2\pi\varepsilon^2). \tag{23}$$

Thus, we have solved the first part of the problem and determined a Hamiltonian for the interaction of a low-frequency EMR with an atom in the form of Eq. (21).

Now let us evaluate the probability of scattering per unit time for a flux of photons on an ensemble of atoms representing a rarefied medium, assuming that the interatomic distances are large as compared to the photon free path length and the scattering events on each atom are independent (no interference). In order to calculate the value of $1/\tau$ as a function of ε, it is convenient to use the following approach. Denoting the density of energy states by $\nu(\varepsilon)$, we can write the scattering amplitude (22) as a sum over ε' and ε'':

$$V = \sum\phi(\varepsilon', \varepsilon'')/\nu(\varepsilon')\nu(\varepsilon'')c^+_{\varepsilon'}c_{\varepsilon''}. \tag{24}$$

Introducing a distribution function for the ensemble of photons as $f_\varepsilon = \langle c^+_\varepsilon c_\varepsilon\rangle$, where the angle brackets denote averaging over a nonequilibrium state of the photons, the collision integral in the Born approximation can be written as (see, e.g. monographs [11–15]) $L\{f_\varepsilon\} = (2\pi/\hbar)\sum\overline{|\phi(\varepsilon, \varepsilon')|}^2/\nu^2(\varepsilon')\nu^2(\varepsilon)(f_{\varepsilon'} - f_\varepsilon)\delta(\varepsilon - \varepsilon')$, where the upper bar denotes averaging over the photon polarization directions and the sum is taken over the virtual states ε'. From this, it follows immediately that the relaxation time can be estimated by the formula

$$1/\tau(\varepsilon) = (2\pi/\hbar) \times \sum |\phi(\varepsilon, \varepsilon')|^2/\nu^2(\varepsilon')\nu^2(\varepsilon)\delta(\varepsilon-\varepsilon'). \tag{25}$$

Passing again from the sum to an integral with respect to ε' according to the rule $\sum(\ldots) = \int \nu(\varepsilon)(\ldots)d\varepsilon/2\pi$, accomplishing simple integration, and substituting an explicit expression for the scattering amplitude (22), we eventually arrive at

$$1/\tau(\varepsilon) = (4\pi^3/9)^2(e^2/a_0mc^2)^4 \times(\langle E\rangle/mc^2)^2\varepsilon^2R(q)/\Delta E^2\nu^3(\varepsilon)\hbar^3. \tag{26}$$

In order to estimate the relaxation time τ(ε), let us take $F(\varepsilon) \approx 2\pi$ and $R(q) \approx b/\hbar cq$ (for the condition $b \gg 1$). Then, assuming that the densities of states of the low-frequency and high-frequency photons are equal, that is, $\nu(\varepsilon) = 1/\Delta E$ where $\varepsilon = \hbar\omega$, we finally obtain

$$1/\tau(\omega) = b^2(4\pi^3/9)^2(e^2/a_0mc^2)^4 \times(\langle E\rangle/mc^2)^2(\omega/cq)^2(\Delta E/\hbar). \tag{27}$$

Taking $\omega = 10^{12}$ s^{-1}, $b = 10^5$, $\Delta E = \hbar cq/b = 10^{-9}$ erg, $a_0 = 10^{-8}$ cm, $q = 10^{13}$ cm^{-1}, and $\langle E\rangle = Z^2me^4/\hbar^2 = 10^{-9}$ erg, we obtain $1/\tau(\omega) = 10^{-2}$ s^{-1} (note that h at this frequency is still smaller). As expected, the estimate shows evidence of a rather weak scattering of monochromatic photons on atoms and seems to be quite reasonable if we recall the well-known fact of receiving radio signals from space, which arrive from radiation sources occurring in very distant regions of the Universe.

Evaluating the dependence of the extinction coefficient on the EMR frequency according to the formula $h = z\nu(\omega/c)^4$ (see [16]), where ν is the volume of a scattering particle and z is a numerical factor, we arrive at an obvious conclusion: in the region of radio and microwave frequencies, the mechanism corresponding to Eqs. (26) and (27) dominates over the "h-mechanism" (it should be recalled that the extinction coefficient h is related to the relaxation time τ simply as $h = 1/c\tau$).

Now we are convinced that, in the region of low frequencies, $1/\tau(\omega) > 1/\tau = hc$. Note that this inequality is already valid in the frequency range $\omega < (Ac/\nu)^{1/2}$, where $A = b^2(4\pi^3/9)^2(e^2/a_0mc^2)^4(\langle E\rangle/mc^2)^2(\Delta E/q^2\hbar)$, which corresponds to frequencies in the microwave range and below. If the scattering particle has a spherical shape with the volume $\nu_0 = (4\pi/3)a_0^3$, we can readily estimate the "crossover" frequency corresponding to equal reciprocal times:

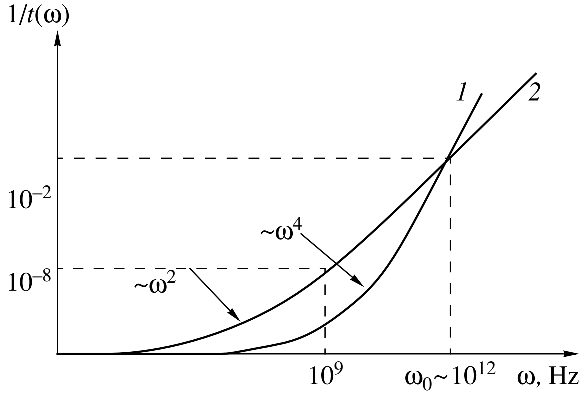

Schematic diagram illustrating the frequency dependence of the reciprocal scattering time according to (*1*) the Rayleigh law and (*2*) the mechanism predicted in this paper, according to which 1/τ is proportional to ω^4 in the region of sufficiently small frequencies of the monochromatic radiation (corresponding to the range of wavelengths about hundreds of meters and above). The crossover frequency $\omega_0 = (Ac/\nu)^{1/2}$ is considered in the text.

$$\omega_0 = b(4\pi^3/3)(Z^2e^2/mc^2a_0)^2 \times(\langle E\rangle/mc^2)(3\Delta Ec/\hbar q^2a_0^3)^{1/2}. \tag{28}$$

For the values of parameters indicated above, $\omega_0 \approx 10^{12}$ s^{-1}. The qualitative and quantitative differences between the Rayleigh scattering and the mechanism considered in this paper are illustrated in the figure.

Thus, the main conclusion is that there exists a limit of applicability of the formula for the extinction coefficient: below a certain limiting frequency, the interaction of EMR with an atom is described by relationship (27), according to which the scattering probability is proportional to ω^2 (rather than to ω^4).

REFERENCES

1. N. B. Delone and V. P. Kraĭnov, *Atom in a Strong Light Field* (Énergoatomizdat, Moscow, 1984).
2. F. V. Bunkin and A. M. Prokhorov, Zh. Éksp. Teor. Fiz. **46** (3), 1090 (1964) [Sov. Phys. JETP **19**, 739 (1964)].
3. M. Gavrila, Phys. Rev. **164** (1), 147 (1967).
4. S. Stendholm, Phys. Rep. **6** (1), 1 (1973).
5. Ya. B. Zel'dovich, Usp. Fiz. Nauk **110** (2), 139 (1973) [Sov. Phys. Usp. **16**, 427 (1973)].
6. D. F. Zaretskiĭ and V. P. Kraĭnov, Zh. Éksp. Teor. Fiz. **66** (2), 537 (1974) [Sov. Phys. JETP **39**, 257 (1974)].
7. V. V. Suran and I. P. Zapesochnyĭ, Pis'ma Zh. Tekh. Fiz. **1** (21), 973 (1975) [Sov. Tech. Phys. Lett. **1**, 420 (1975)].

8. N. B. Delone, V. A. Kovarskiĭ, A. V. Maslov, and N. F. Perel’man, Usp. Fiz. Nauk **131** (4), 617 (1980) [Sov. Phys. Usp. **23**, 472 (1980)].
9. L. D. Landau and E. M. Lifshitz, *Course of Theoretical Physics*, Vol. 3: *Quantum Mechanics: Non-Relativistic Theory* (Nauka, Moscow, 1974; Pergamon, New York, 1977).
10. V. B. Berestetskii, E. M. Lifshitz, and L. P. Pitaevskii, *Course of Theoretical Physics*, Vol. 4: *Quantum Electrodynamics* (Nauka, Moscow, 1980; Pergamon, Oxford, 1982).
11. A. I. Akhiezer, V. G. Bar’yakhtar, and S. V. Peletminskii, *Spin Waves* (Nauka, Moscow, 1967; North-Holland, Amsterdam, 1968).
12. B. M. Mogilevskiĭ and A. F. Chudnovskiĭ, *Thermal Conductivity of Semiconductors* (Nauka, Moscow, 1972).
13. A. I. Anselm, *Introduction to Semiconductor Theory* (Nauka, Moscow, 1978; Prentice-Hall, Englewood Cliffs, 1981).
14. E. M. Lifshitz and L. P. Pitaevskiĭ, *Course of Theoretical Physics*, Vol. 10: *Physical Kinetics* (Nauka, Moscow, 1979; Pergamon, Oxford, 1981).
15. S. O. Gladkov, *Physics of Composites: Thermodynamic and Dissipative Properties* (Nauka, Moscow, 1999).
16. K. S. Shifrin, *Light Scattering in Turbid Medium* (GITTL, Moscow, 1951).

Translated by P. Pozdeev

Technical Physics Letters, Vol. 28, No. 8, 2002, pp. 657–659. Translated from Pis'ma v Zhurnal Tekhnicheskoĭ Fiziki, Vol. 28, No. 15, 2002, pp. 79–85.
Original Russian Text Copyright © 2002 by Mingaleeva.

On the Mechanism of a Helical Motion of Fluids in Regions of Sharp Path Bending

G. R. Mingaleeva
Kazan State Power Engineering Institute, Kazan, Tatarstan, Russia

Received January 9, 2002

Abstract—The pattern of flow in the inner and outer streams of a liquid or gas in regions of a sharp path bending at a right angle is considered. It is shown that a high hydraulic drag makes it energetically favorable for the fluid to perform a twisted helical motion. Such a regime is spontaneously established under real conditions. An example of this hydraulic factor is offered by an atmospheric cyclone. © *2002 MAIK "Nauka/Interperiodica".*

There are many natural phenomena and technological processes in which flows of liquids or gases encounter regions where the flow path exhibits a sharp turn or bending. Observations show that a medium bypassing such regions exhibits a spontaneous helical rotation, frequently with the formation of several macroscopic and microscopic helical vortices. The forms of this motion display certain specific features depending on the ability of a particular system to self-organize. Several examples of such flows are depicted in Fig. 1.

An analysis of the relevant data, including generalization of the phenomena occurring on different scales, suggests that a common mechanism must exist which is responsible for a self-twisting flow development in fluids under conditions of a sharp path bending. Below, this mechanism is studied from the energy standpoint.

As is known, a fluid flow in a region of sharp bending at a right angle must overcome a high local hydraulic drag and, hence, involves considerable energy losses. For example, the relative local drag in a 90° pipe bend may vary from 0.2 up to 10 with respect to the input flow head, depending on the particular geometry. The lower limit refers to the case of an "optimum" bend with self-rounded sharp edge, whereby the flow exhibits neither collisions of the streams nor changes in their shapes and cross-section dimensions. The upper limit corresponds to a flow outgoing from a bend with sharp edges and a deformed output cross section [9]. Such a large local drag is significantly greater than usual values of the relative friction drag, which do not exceed one-tenth of the input head for objects with a characteristic ratio of $L/D \approx 1$ (L and D being the longitudinal and transverse object dimensions, respectively) in a wide range of Reynolds numbers, where the typical interval of variation of the friction drag coefficient is $\lambda = 0.01–0.1$.

Under these conditions, a flow can either move with an impact on the obstacle, which obviously leads to considerable energy losses, or bypass the obstacle. Evidently, liquids and gases capable of self-organization will flow, according to the well-known laws of mechanics, by the path of minimum resistance. In the case under consideration, such a path is offered by a helical trajectory. Pipeline elements such as coils exhibit no sharp bending regions, and a flow in these elements exhibits only energy losses for the friction drag, although with a somewhat increased value of the hydro-

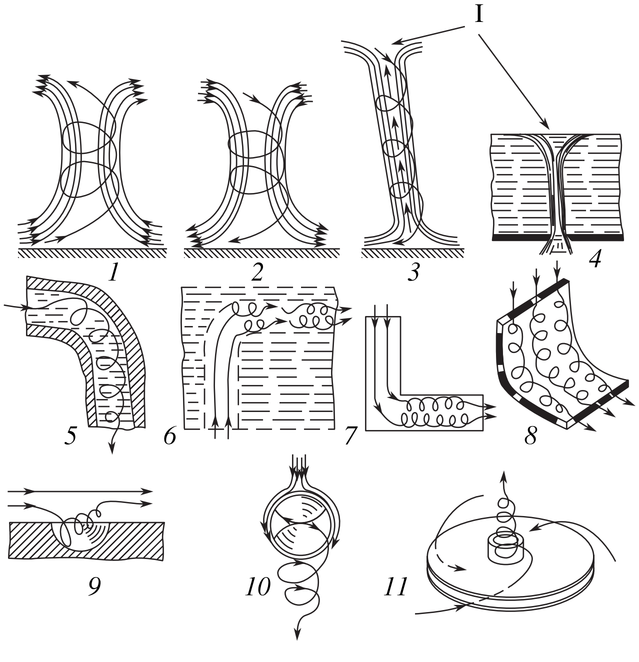

Fig. 1. Examples of spontaneous motion of an axial fluid flow by a helix or by a series of macroscopic and microscopic helical vortices in the regions of a sharp right-angle flow path bending: (*1*) atmospheric cyclone; (*2*) anticyclone; (*3*) tornado (I, tornado eye) [1–4]; (*4*) funnel in a liquid (I, funnel eye) [5, 6]; (*5*) river bed bending [7]; (*6*) ocean stream turning point [8]; (*7*) flow in a 90° pipe bend with sharp edges [9]; (*8*) flow at a 90° bent wall [10]; (*9*) streamlined hemispherical cavity [11, 12]; (*10*) streamlined ball [13]; (*11*) flow of an air evacuated from a radial slit via the central hole [14].

1063-7850/02/2808-0657$22.00 © 2002 MAIK "Nauka/Interperiodica"

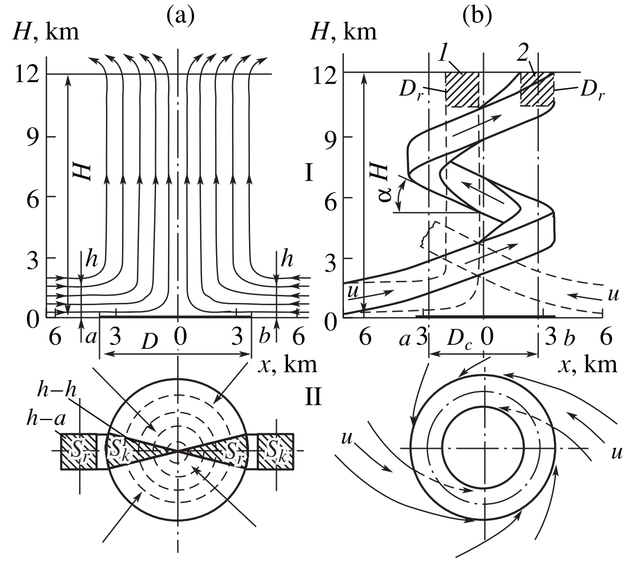

Fig. 2. Air-flow regimes in an atmospheric cyclone: (a) noncirculatory flow at the nucleation stage in (I) vertical section and (II) horizontal section at the surface, showing transverse cross sections before (S_r) and after (S_k) bending; (b) helical flow in a (I) lateral view showing transverse sections (cross-hatched) of the streams in the (*1*) straight flow with initial bending and (*2*) helical flow and (II) top view.

dynamical friction drag coefficient. Nevertheless, these energy losses are significantly lower as compared to those for surmounting sharp path bending in the regions with a local drag coefficient of $C_1 \approx 0.2$, the more so if we take into account that a sharp bending of streams at a right angle usually results either in head-on impact or in deformation of the cross section (in which case $C_1 \longrightarrow 10$).

In what follows, these factors are considered in more detail by application to a particular example offered by the motion of air masses in a medium-size atmospheric cyclone. Figure 2a shows a schematic diagram of such a cyclone at the nucleation (i.e., noncirculatory) stage, featuring neither rarefaction zone nor reverse circulation currents at the center. The figure indicates principal size parameters used in the following analysis (representing one of the particular cases studied [3]).

In most typical cases, a cyclone is formed by the following scheme. An air mass, heated and saturated by water vapor over a warm region (*a*–*b*) of the underlying surface, raises upward in the form of a column as a result of convection caused by the buoyancy effect. New portions of air, arriving to the evacuated site of lowered pressure via radial pathways from the surrounding colder near-ground layer, reach the *a*–*b* region and (heated and vapor-saturated) rise sharply upward in a stream turning at a 90° angle. As a result (according to the condition of flow continuity), a continuous flow is established obeying an obvious relation $\pi D h \approx \pi D^2/4$ (for $\rho u \approx$ const), which yields $h \approx 0.25D$ (h is the height of a near-ground air layer at the entrance of the *a*–*b* zone; D is the equivalent diameter of the *a*–*b* zone; and ρ and u are the local air density and velocity, respectively). The cyclone operates like a thermal machine driven by solar energy.

This scheme features the aforementioned (energetically unfavorable) steep turn of the air stream from horizontal to vertical, the turn involving a head-on collision of the counterflowing streams with deformation of the cross sections (cf. S_r and S_k in Fig. 2a). For the reasons considered above, the flow regime is spontaneously switched into a helical rise mode.[1] Figure 2b schematically illustrates this process for a separate twisted stream (solid curves) in comparison to a straight stream with initial bending (dashed curves).

Selecting separate streams and accomplishing simple calculations by conventional methods, one can readily show that power spent to overcome the hydraulic drag for raising an air mass up to a height H by a helix with the sloping angle α, as calculated by the formula

$$N_3 = Q\Delta p_{23} = Q\lambda_{23}\frac{H}{D_r \sin\alpha}\frac{\gamma u^2}{2g},$$

is significantly lower as compared to that for the motion and rising of equivalent air masses at the same velocities by a straight column with right-angle bending, determined by an analogous formula

$$N_0 = Q(\Delta p_{20} + \Delta p_{10})$$

$$= Q\left(\lambda_{20}\frac{H}{D_r}\frac{\gamma u^2}{2g} + C_{10}\frac{\gamma u^2}{2g}\right) = Q\frac{\gamma u^2}{2g}\left(\lambda_{20}\frac{H}{D_r} + C_{10}\right).$$

Here, N is the power spent for the air-stream motion, Q is the air-flow rate, Δp is the hydraulic drag, and indexes 0–3 refer to the straight stream, local drag, friction drag, and helical stream, respectively. The results of direct observations after atmospheric cyclones show that the helix slope varies within $\alpha \approx 45°–65°$ [2]. Typical values of the friction drag coefficient are as follows: $\lambda_{20} = 0.01–01$, $\lambda_{23} = 0.03–0.15$ (for $\mathrm{Re} = 10^3–10^6$) and $C_1 = 0.2–10$ [9]. Geometrical parameters involved in the calculations are indicated in Fig. 2.

The moments of transition to the stabler helical flow regime (as well as the twist direction: clockwise versus counter-clockwise) exhibit a probabilistic character, depending primarily on the degree of background asymmetry. If this asymmetry is (accidentally) ideal, the rotation may not begin and the vertical circulatory motion will decay as the air column goes away from the nucleation site. However, we will not dwell here on the laws of spontaneous symmetry violation.

---

[1] It should be noted that the pattern of a self-twisting cyclone formation discussed here by no means belittles the role of other numerous factors described in the literature [1–4].

The phenomenon of overcoming the hydraulic drag in the region of sharp path bending at the right angle, with establishment of an energetically more favorable helical motion, will be referred to as the "hydraulic factor." It is easy to show that the hydraulic factor plays a decisive role in all cases of self-twisting helical flows depicted in Fig. 1. One must also bear in mind that this factor is most clearly manifested in a certain interval of the dimensionless criterion controlling the process (Reynolds, Dean, Hurtler, Taylor, and Euler numbers, etc.), the boundaries of which should be established (with an allowance for the probabilistic–statistical character of the phenomenon) by additional investigations.

There are grounds to suggest that the hydraulic factor is independent of the system scale (from giant cyclones to small vortex funnels) and exhibits a universal character. The site of path bending in a fluid flow, creating a situation of instability on an asymmetric background, serves as a generator of the spontaneous motion by a helix or by a series of macroscopic and microscopic helical vortices.

REFERENCES

1. A. V. Byalko, *Our Planet—the Earth* (Nauka, Moscow, 1983).
2. D. V. Nalivkin, *Tornados* (Nauka, Moscow, 1984).
3. A. Kh. Khrgian, *Physics of Atmosphere* (Fizmatgiz, Moscow, 1958).
4. L. T. Matveev, *Course of General Meteorology. Physics of Atmosphere* (Gidrometeoizdat, Leningrad, 1984).
5. V. M. Polikovskiĭ and R. G. Perel'man, *Funnel Formation in Fluids with Open Surface* (GÉI, Moscow, 1959).
6. G. V. Logvinovich, V. N. Buĭvol, A. S. Dudko, *et al.*, *Free Surface Flows* (Naukova Dumka, Kiev, 1985).
7. M. A. Lavrent'ev and B. V. Shabat, *Problems of Hydrodynamics and Related Mathematical Models* (Nauka, Moscow, 1977).
8. P. Thierry and N. Doron, Deep-Sea Res., Part I **43** (9), 1475 (1996).
9. I. E. Idel'chik, *Handbook on Hydraulic Resistances* (Mashinostroenie, Moscow, 1975).
10. H. Schlichting, *Entstehung der Turbulenz* (Berlin, 1959; Inostrannaya Literatura, Moscow, 1962).
11. Ya. P. Chudnovskiĭ, A. P. Kozlov, A. V. Shchukin, *et al.*, Izv. Akad. Nauk, Énerg., No. 3, 39 (1998).
12. S. A. Isaev, A. I. Leont'ev, P. A. Baranov, and A. E. Usachev, Dokl. Akad. Nauk **373** (5), 615 (2000) [Dokl. Phys. **45**, 389 (2000)].
13. M. A. Gol'dshtik, V. N. Shtern, and N. I. Yavorskiĭ, *Viscous Flow with Paradoxical Properties* (Nauka, Novosibirsk, 1989).
14. M. A. Gol'dshtik and V. N. Shtern, Prikl. Mat. Mekh. **53** (4), 619 (1989).

Translated by P. Pozdeev

Technical Physics Letters, Vol. 28, No. 8, 2002, pp. 660–663. Translated from Pis'ma v Zhurnal Tekhnicheskoĭ Fiziki, Vol. 28, No. 15, 2002, pp. 86–94.
Original Russian Text Copyright © 2002 by Drapak, Manasson, Netyaga, Kovalyuk.

Negative Differential Conductivity in a p^+-Bi_2Te_3–p-GaSe Isotype Heterostructure

S. I. Drapak[a],*, V. A. Manasson[b], V. V. Netyaga[a], and Z. D. Kovalyuk[a]

[a] *Chernovtsy Branch, Frantsevich Institute for Materials Science Problems, National Academy of Sciences of Ukraine, Chernovtsy, Ukraine*
** e-mail: chimsp@unicom.cv.ua*
[b] *Antenna Development Company, Waveband Corporation, Torrance (CA), USA*

Received November 23, 2001

Abstract—The electrical properties of a p-Bi_2Te_3–p-GaSe isotype heterostructure synthesized for the first type were studied. A qualitative model is proposed which explains the appearance of a negative differential conductivity in the structure under forward (and, when illuminated, reverse) bias conditions. © *2002 MAIK "Nauka/Interperiodica".*

Gallium selenide (GaSe), exhibiting the natural anisotropy of chemical bonds in and between the crystal layers (which allows atomically smooth mirror substrates with low numbers of "dangling" bonds to be obtained by cleavage in air), offers the ideal material for fabricating various surface-barrier structures under laboratory conditions. Gallium selenide can be used as a base material for solar cells [1], highly effective photodiodes [2], and polarized radiation sensors [3]. One of the factors hindering wide commercial use of this material is the high resistance of the heterostructures based on GaSe substrates. However, a decrease in the resistance of GaSe to a level typical of commercial silicon diodes may lead to nontrivial consequences, whereby the electrical characteristics of the structures will be determined by the properties of interfaces, rather than of the barriers. This effect must be especially pronounced in structures with low potential barriers.

Here we present the results of investigation of a p^+-Bi_2Te_3–p-GaSe isotype heterostructure synthesized for the first type, with a dc resistance of 20–40 Ω and a potential barrier height of 0.1 eV, as determined from the current–voltage (J–U) characteristics.

The samples of heterojunctions were prepared using weakly degenerate single crystals of Bi_2Te_3 and dysprosium-doped single crystals of GaSe with a room-temperature ($T = 300$ K) hole density of $p = 1.6 \times 10^{19}$ cm^{-3} and $p \approx 10^{16}$ cm^{-3}, respectively. The junctions were obtained by the method of optical contact formation [4]. The thickness of a GaSe substrate was 1–1.5 mm and that of a Bi_2Te_3 crystal layer was 0.1–0.2 mm. The current-carrying indium contacts were fused into both Bi_2Te_3 and GaSe sides at 150–180°C and remained ohmic in the entire range of current densities studied. The heterostructures exhibited pronounced rectifying properties in a broad range of temperatures, with the forward current exceeding the reverse current by a factor of not less than 5×10^3 at a forward bias of 1.5–2 V. The forward direction of the J–U characteristic corresponds to a positive potential on the GaSe side.

Figure 1 (curve *1*) shows a typical static current–voltage characteristic of the p^+-Bi_2Te_3–p-GaSe structure measured at $T = 290$ K using an amplitude–frequency analyzer of the H.F.FRA 1255&1286 type. The measurements were performed by changing the applied voltage with a certain step at a rate of 10–200 mV/s. As can be seen, the J–U curve contains a region of negative differential conductivity (NDC). When the current–voltage characteristic was measured point by point, the

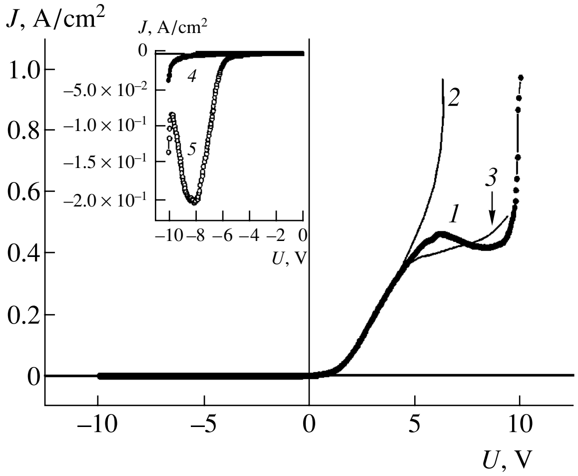

Fig. 1. Typical current–voltage characteristics of the p^+-Bi_2Te_3–p-GaSe isotype heterostructure measured at $T = 290$ K measured (*1*) under static conditions and (*2*, *3*) in a 50-Hz ac current mode. The inset shows a reverse branch of the characteristic measured on the same heterostructure (*4*) in the dark and (*5*) under illumination.

1063-7850/02/2808-0660$22.00 © 2002 MAIK "Nauka/Interperiodica"

pattern remained generally the same but, beginning with a bias voltage of $U \geq 4.5$ V, the J–U curve exhibited a certain delay in the current density (up to 30%) relative to curve *1*. The J–U curves measured in a 50-Hz ac mode contained no NDC region: the oscilloscope screen displayed only a change in shape of the forward branch from position *2* to *3* (Fig. 1). The transitions took place at a relaxation time of 4–6 s, which is evidence of a slow rate of processes responsible for the NDC region in the p^+-Bi_2Te_3–p-GaSe structure. When the heterojunction was illuminated at a power density of 100 mW/m^2, the NDC region was also observed in the reverse branch of the static current–voltage characteristic (see the inset to Fig. 1).

The first point to be noted is that the measurements of resistivity as a function of temperature for GaSe and Bi_2Te_3 give no grounds to attribute the appearance of NDC in the p^+-Bi_2Te_3–p-GaSe heterostructure to the effect of temperature on the conductivity in one (or both) of the two contacting semiconductors. Nor can we explain the NDC (taking into account the degenerate character of Bi_2Te_3) within the framework of a tunneling diode model, since the valence band of p-GaSe corresponds to the allowed levels of Bi_2Te_3 even under equilibrium conditions.

As is known, slow processes can be due either to a system of charged particles possessing "collective" properties (double injection currents) [5] or to the surface states situated in an insulating layer [6]. The former situation is unlikely because (even with an allowance for the injection from ohmic contacts in the rear "nonrectifying" In layer–p^+-Bi_2Te_3–p-GaSe system) the formation of a plasma under forward bias conditions is possible only in Bi_2Te_3; since the resistivity of Bi_2Te_3 is much lower than that of GaSe, a change in the voltage drop on the former semiconductor will not significantly modify the potential distribution in the heterostructure. As is known, cleavage of a semiconductor even under high-vacuum conditions cannot exclude the formation of an oxide layer of the exposed surface [6]. Indeed, it was reported [7, 8] that an ultrathin (with a thickness on the order of atomic dimensions) oxide layer of Ga_2O_3 appeared on a GaSe surface within several minutes after cleavage in air.

Figure 2 shows an energy band diagram of the p^+-Bi_2Te_3–p-GaSe heterostructure under equilibrium conditions, which makes an allowance for a thin insulating interfacial layer (the bandgap width of Ga_2O_3 is $E_g = 4.6$ eV [9]) with localized deep traps. The diagram was constructed taking into account data on the physical parameters of semiconductors [10] and the concentrations of majority carriers determined from the Hall effect measurements. The surface band bending φ_0 in GaSe was determined from the J–U curves using the method described in [11].

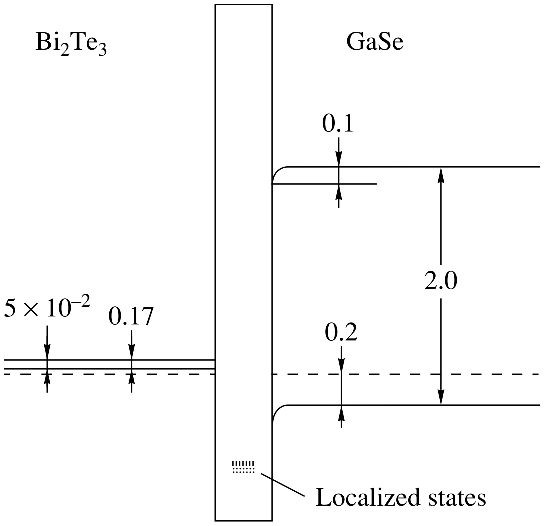

Fig. 2. An energy band diagram of the p^+-Bi_2Te_3–p-GaSe heterostructure with an insulating layer under equilibrium conditions (all energy characteristics are given in electron-volts).

As can be seen from Fig. 2, already a direct bias of $U \geq (2–3)kT$ leads to a flat-band situation in GaSe and the heterostructure under consideration becomes like a classical metal–insulator–metal system, the only difference being that the charge is carried by holes rather than by electrons. According to [6], the charge transfer in the system studied is caused by thermoelectron emission and can be described by the relation

$$I = AT^2 \exp(-W_C/kT)\exp(eU/kT - 1), \qquad (1)$$

where e is the electron charge, $A = 4\pi mk^2e/h^3$ is the Richardson constant, and W_C is the electron work function of the anode material. In our case, factor A should be replaced by the effective Richardson constant $A^* = Am^*/m$ (where m^*/m is the relative effective mass of the majority charge carriers) and W_C, by the electron work function of a semiconductor from which the charge carriers are injected under forward bias conditions (i.e., Bi_2Te_3). Note that the charge in a metal–insulator–metal system can be also transferred by means of tunneling. However, we will not consider this case here, because the tunneling mechanism implies a temperature-independent current–voltage characteristic (or the saturation current depending very weakly on the temperature), which contradicts our experimental results.

Thus, in a forward-biased heterostructure, the voltage drops mostly on the insulating layer. This is related to the small height of the potential barrier in GaSe (0.1 eV) and the related small resistance of the charge-transfer region. At a certain level of the forward bias, the valence band of GaSe decreases down to a level of localized states (slow levels) in the insulator. Then part of the holes tunnel from GaSe to these states and the charge carried by these holes leads to an increase in the barrier height and, in turn, to a decrease in the thermoelectron emission current. The localized states of the

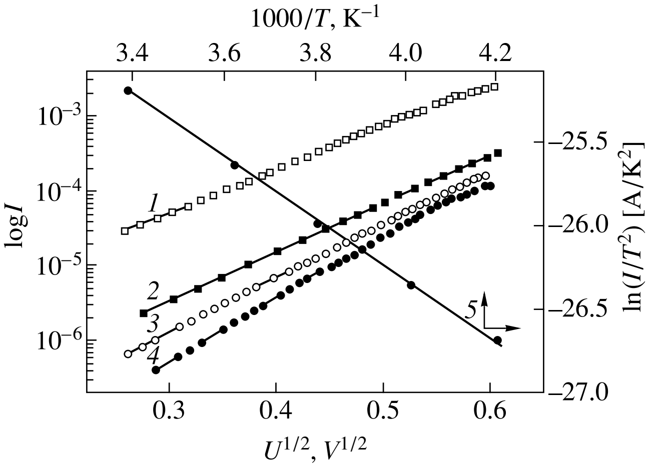

Fig. 3. Current–voltage characteristics of the p^+-Bi_2Te_3–p-GaSe heterostructure plotted in $\log I$ versus $U^{1/2}$ coordinates for various temperatures T = 323 (*1*), 295 (*2*), 263 (*3*), and 238 (*4*); curve (*5*) shows the plot of $\ln(1/T_2)$ versus reciprocal temperature.

insulator may also take place in the transport of charge carriers through this layer (e.g., by the step tunneling mechanism). However, these processes are rather slow and not as effective as the thermoelectron emission. It is possible that the system even features a kind of the positive feedback with respect to the charge transfer: the greater the number of holes tunneling to the localized states in the insulator, the higher the barrier, after which it is energetically favorable for a still greater number of holes to pass by tunneling into the insulator and so on. The further current buildup with increasing forward bias is related to the fact that the valence band of GaSe decreases below the localized slow states and the trapping of charge carriers by these traps becomes impossible.

In the opposite direction, the charge-transfer region in GaSe possesses a higher resistance as compared to that of the insulating layer and, hence, a reverse voltage applied to the p^+-Bi_2Te_3–p-GaSe structure drops mostly in this very region. For low reverse bias values, the J–U curve exhibits a sublinear character typical of the currents related to the generation–recombination processes in the charge transfer region. Only at $|U| \geq$ 0.4–0.5 V, does a slow increase in the current change for a sharp superlinear growth related, in all probability, to the tunneling of carriers into GaSe through the barrier. This mechanism is quite possible since the barrier localized in the base semiconductor acquires a parabolic shape under the action of image forces. According to [6], the current–voltage characteristic of a barrier with a parabolic potential profile (whereby tunneling is the main mechanism of the charge transfer) must represent a straight line in the coordinates of $\ln[IU^{-1}(\varphi_0 - eU)^{-1/2}]$ versus $(\varphi_0 - eU)^{-1/2}$, which is actually observed in the experiment.

The situation changes when the heterostructure is illuminated. In the case under consideration, illumination is equivalent to shifting the potential barrier in GaSe in the forward direction, which results in rectification of the bands in GaSe. This system is analogous to the heterostructure under forward bias conditions, the only difference being that the holes move in the opposite direction (from Bi_2Te_3 to GaSe). In this case, most of the applied voltage drops on the insulating layer and, hence, the over-barrier thermoelectron emission current becomes the dominating mechanism of the charge transfer across the insulator. The NDC phenomenon takes place when the valence band of Bi_2Te_3 approaches the slow states localized in the insulator. The current reaches saturation and, as the applied voltage keeps growing, begins to decrease due to the positive feedback. A buildup of the current with subsequent increase in the bias voltage is explained both by the valence band of Bi_3Te_3 decreasing below the slow states and by the tunneling breakdown of the heterostructure.

It should be noted that, in the metal–insulator–metal system, the charge transfer over the barrier introduced by the insulating layer implies that the conductivity of this layer is zero and determines the diode coefficient. Calculated from the slope of the current–voltage characteristic plotted as $\log I = f(U)$, this coefficient should be $n = 1$. This value was retained in the structure studied for bias voltages $U < 3kT$. As the applied voltage increased above this level, the diode coefficient acquired the value $n = 2$ in the entire temperature range studied. At the same time, the current–voltage characteristic of the structure (for $U \geq 3kT$) was described by a relation of the type $I \sim \exp U^{1/2}$ (Fig. 3, curves *1*–*4*), which is typical both of the Schottky emission and of the Frenkel ionization [6]. Linearity of the $\ln(I/T^2)$ versus $1/T$ plot (Fig. 3, curve *5*) is evidence in favor of the Schottky emission. This is also confirmed by the fact that, determined from the relation [6]

$$\log I = \log(A^*T^2) - 0.43e\varphi_B/kT, \qquad (2)$$

the barrier height of the semiconductor–insulator–semiconductor structure amounts to $\varphi_B \approx 1.2$ eV at T = 295 K. This value agrees well with the cutoff-current voltage (used for estimation of the barrier height) observed at relatively high voltages and explains the discrepancy between the latter parameter and the contact potential difference φ_0 determined from the current–voltage characteristic.

Nevertheless, the insulating layer thickness determined from the slope of the current–voltage characteristic plotted as $\ln I = f(U^{1/2})$ (Fig. 3, curve *2*) amounts to ~2 nm, which is somewhat greater than the value (0.6–0.8 nm) expected according to [7, 8]. This discrepancy can be related to the fact that we assumed the presence of an insulating layer only on the GaSe surface. However, an oxide film could form on the Bi_2Te_3 surface as well. One can also take into account an air gap between the surfaces of two semiconductors in contact. Upon formally dividing the estimated thickness by three, we obtain a complete agreement with the results of [7, 8].

Thus, the proposed model well explains the appearance of a negative differential conductivity in forward-biased (and, under illumination, in reverse-biased) p^+-Bi$_2$Te$_3$–p-GaSe isotype heterostructures.

Acknowledgments. The authors are grateful to V.I. Litvinov (Waveband Corporation, USA) for his interest in this study and fruitful discussions.

REFERENCES

1. S. I. Drapak, V. N. Katerinchuk, Z. D. Kovalyuk, and V. A. Manasson, Fiz. Élektron. **41**, 92 (1990).
2. S. I. Drapak and Z. D. Kovalyuk, Pis'ma Zh. Tekh. Fiz. **27** (18), 1 (2001) [Tech. Phys. Lett. **27**, 755 (2001)].
3. V. A. Manasson, Z. D. Kovalyuk, S. I. Drapak, and V. N. Katerinchuk, Electron. Lett. **26** (10), 664 (1990).
4. V. L. Bakumenko and V. F. Chishko, Fiz. Tekh. Poluprovodn. (Leningrad) **11** (10), 2000 (1977) [Sov. Phys. Semicond. **11**, 1171 (1977)].
5. É. I. Adirovich, P. M. Karageorgiĭ-Alkalaev, and A. Yu. Leĭderman, *Double Injection Currents* (Radio i Svyaz', Moscow, 1978).
6. S. Sze, *Physics of Semiconductor Devices* (Wiley, New York, 1981; Mir, Moscow, 1984), Vols. 1, 2.
7. C. Tatsuyama, S. Ichimura, and H. Iwakuro, Jpn. J. Appl. Phys. **21**, L25 (1982).
8. V. L. Bakumenko, Z. D. Kovalyuk, E. A. Tishin, and V. F. Chishko, Fiz. Élektron. **49**, 123 (1997).
9. T. Hariu, S. Sasaki, H. Adachi, and H. Shibata, Jpn. J. Appl. Phys. **16**, 841 (1977).
10. *Physicochemical Properties of Semiconductor Compounds: a Handbook*, Ed. by A. V. Novoselova, V. B. Lazarev, Z. S. Medvedeva, *et al.* (Nauka, Moscow, 1979).
11. Yu. A. Gol'dberg, O. V. Ivanova, T. V. L'vova, and B. V. Tsarenkov, Fiz. Tekh. Poluprovodn. (Leningrad) **18** (8), 1472 (1984) [Sov. Phys. Semicond. **18**, 919 (1984)].

Translated by P. Pozdeev

Technical Physics Letters, Vol. 28, No. 8, 2002, pp. 664–665. Translated from Pis'ma v Zhurnal Tekhnicheskoĭ Fiziki, Vol. 28, No. 16, 2002, pp. 1–5.
Original Russian Text Copyright © 2002 by Mardasova, Abdulvakhidov, Burakova, Kupriyanov.

The Effect of a Constant Electric Field on the Domain Structure of Ferroelectric $PbSc_{0.5}Nb_{0.5}O_3$ Crystals

I. V. Mardasova, K. G. Abdulvakhidov, M. A. Burakova, and M. F. Kupriyanov
Rostov State University, Rostov-on-Don, Russia
e-mail: kam@rnd.runnet.ru

Received January 24, 2002

Abstract—The effect of a constant electric field on the domain structure formation in ferroelectric lead scandium niobate ($PbSc_{0.5}Nb_{05}O_3$) crystals was studied by a polarization-optical method. It is shown that the crystals contain 71° and 180° domains with the boundaries representing (100) and (110) crystal planes. *© 2002 MAIK "Nauka/Interperiodica".*

Although lead scandium niobate $PbSc_{0.5}Nb_{05}O_3$ (PSN) has been known for a long time [1], the domain structure of PSN crystals is still insufficiently studied. This problem was touched upon in our previous communication [2].

Here we report the results of a polarization-optical study of the domain structure formation and the polarization switching by a constant electric field in freshly grown PSN crystals.

The experiments were performed on PSN samples grown by crystallization of a solution melt in a temperature range from 1200 to 850°C. The crystals had the shape of rectangular parallelepipeds with linear dimensions from 10 μm to 2 mm. The domain structure and polarization switching processes were visually studied with the aid of a special device mounted on an objective table of a polarization microscope, which allowed a constant electric field to be applied to the sample in various crystallographic directions. The electrodes were represented by drops of a concentrated LiCl solution or aquadag.

At room temperature, the PSN crystals possess a rhombohedral symmetry. According to the principle of symmetry and electroneutrality of the domain boundaries in the state of a minimum crystal energy (whereby $\mathbf{nP}_1 - \mathbf{nP}_2 = 0$, where $\mathbf{P}_1$ and $\mathbf{P}_2$ are the spontaneous polarization vectors in the adjacent domains and $\mathbf{n}$ is the normal to the domain boundary), permissible angles between the $\mathbf{P}_s$ vectors of adjacent domains in PSN must be about 71° (109°) and 180°.

As was noted in [3], the domain structure of PSN is rather complicated and depends on the crystal growth conditions and the sample geometry. The crystals with linear dimensions on the order of several dozens of microns exhibit rather clear domain boundaries which can be observed in a polarization microscope. Observations in the course of the layer-by-layer etching of a thick PSN crystal showed that the domain structure varies in depths of the crystal. This is probably explained by the presence of mechanical stresses and growth defects in the crystals, which violate homogeneity of the spontaneous polarization over the crystal volume in the course of the phase transition. Therefore, the domain structure of a real crystal corresponds to a compromise between the symmetry and energy considerations, on the one hand [4], and the perturbing action of inhomogeneous straining and growth defects, on the other hand [5].

As reported previously [2], the application of a constant electric field with a strength of 1.5 kV/cm leads to breakage of the initial domains into smaller ones, smearing of the domain boundaries, vanishing of the domains with the boundaries oriented parallel to the field, and the coarsening (by lateral propagation) and growth of the domains with 71° walls perpendicular to the **E** direction. On the electrode side, the samples exhibited sharp domain wedges oriented at about 45° relative to the applied field **E**, which represented the 180° domains. Colliding with the domain walls oriented perpendicularly to the field **E**, these domains exhibit repeated refraction by 45°.

Increasing the applied voltage up to 3–4 kV/cm leads to the growth of domains with boundaries perpendicular to the field **E**. However, switching off the field leads to partial restoration of the initial domain structure. Holding the sample for 10–30 min in a field of 5–8 kV/cm fixes positions of the 71° domain boundaries perpendicular to the field, as well as the 180° domain boundaries making an angle of 45° with the field direction; all domains with boundaries parallel to the field disappear from the field of vision (see the figure). However, the first transformation of the crystal to a paraphase and back partly restores the initial domain structure.

Study of the crystals etched after exposure to the field showed that domains with the positive ends of the spontaneous polarization vectors $\mathbf{P}_s$ emerging at the crystal surface are etched at a higher rate than the

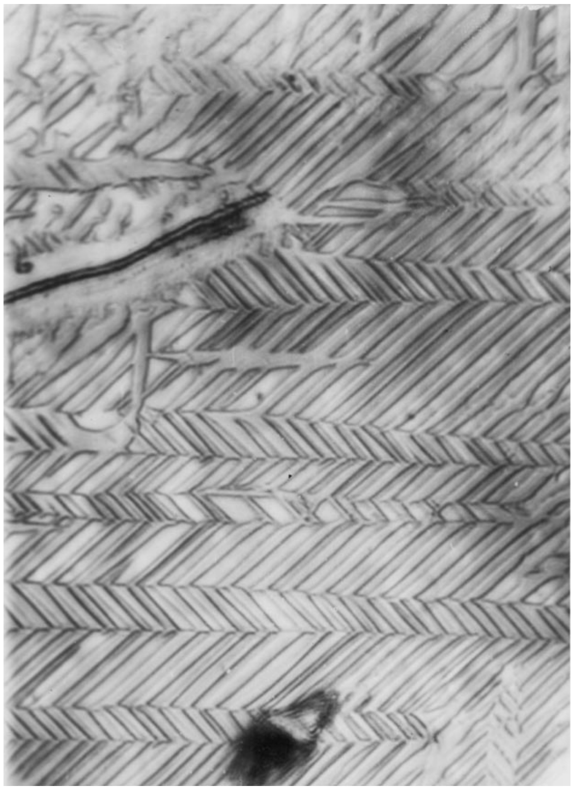

A micrograph showing the 71° and 180° domain structure of a $PbSc_{0.5}Nb_{05}O_3$ crystal. The electric field is directed downward (magnification, ×170).

domains with the negative $\mathbf{P}_s$ ends. Observed in the polarization microscope, the former domains exhibit a dull tint slightly different from that of the neighboring domains. It should be noted that not all regions of the crystal are equally involved in the polarization switching process. Depending on the degree of defectness in various regions of the crystal, the configuration of domains in these regions may vary. A remarkable fact is that the domain boundaries perpendicular to the field direction, which performed oscillations about a certain average position and possessed a sawtooth shape, exhibited a jumplike lateral expansion upon application of the electric field.

A further increase in the applied field strength (up to 9–10 kV/cm) leads to the appearance of microcracks under the electrodes, the formation of regions resembling a block structure, and the heating of a crystal (with transition into a paraphase or electric breakdown). It should be noted that the PSN crystals contain no large regions of a monodomain state (such as that typical of, e.g., $BaTiO_3$). The domain widths measured with an object micrometer exhibited a scatter within 3–5 μm for 71° domains and 13–15 μm for 180° domains.

Thus, it was established that the application of a constant electric field to PSN single crystals leads to the formation of 71° and 180° domain structures with the boundaries representing (100) and (110) crystal planes. The threshold electric field strengths at which the formation of such a structure takes place are different for various samples, depending on the crystal perfection and homogeneity.

REFERENCES

1. G. A. Smolenskii, V. A. Bokov, V. A. Isupov, N. N. Krainik, R. E. Pasynkov, A. I. Sokolov, and N. K. Yushin, *The Physics of Ferroelectric Phenomena* (Nauka, Leningrad, 1985).
2. K. G. Abdulvakhidov and M. F. Kupriyanov, Kristallografiya **41** (6), 1066 (1996) [Crystallogr. Rep. **41**, 1013 (1996)].
3. K. G. Abdulvakhidov, I. V. Mardasova, T. P. Myasnikova, *et al.*, Fiz. Tverd. Tela (St. Petersburg) **43** (3), 489 (2001) [Phys. Solid State **43**, 508 (2001)].
4. I. S. Zheludev and L. A. Shuvalov, Izv. Akad. Nauk SSSR, Ser. Fiz. **21** (2), 264 (1957).
5. F. Jona and G. Shirane, *Ferroelectric Crystals* (Pergamon, Oxford, 1962; Mir, Moscow, 1965).

Translated by P. Pozdeev

Technical Physics Letters, Vol. 28, No. 8, 2002, pp. 666–668. Translated from Pis'ma v Zhurnal Tekhnicheskoĭ Fiziki, Vol. 28, No. 16, 2002, pp. 6–11.
Original Russian Text Copyright © 2002 by P. P. Belousov, P. Ya. Belousov, Dubnishchev.

Laser Doppler Imaging of the Velocity Field in a Swirling Rank Flow

P. P. Belousov, P. Ya. Belousov, and Yu. N. Dubnishchev
Institute of Thermal Physics, Siberian Division, Russian Academy of Sciences, Novosibirsk, Russia
e-mail: dubnistchev@itp.nsc.ru

Received March 5, 2002

Abstract—The velocity field in a swirling Rank flow is studied for the first time by the laser Doppler imaging technique. © *2002 MAIK "Nauka/Interperiodica".*

Optical diagnostics of kinematic parameters is an extensively developed field of laser applications, both in basic research and in industrial technologies, related to the demand for nonperturbative measurement and monitoring of gaseous and condensed media. At present, most widely used for these purposes are the laser Doppler anemometry techniques [1] ensuring the measurement of a local flow velocity. However, the problem of determining spatial distribution of the velocity field on a real time scale has still received no satisfactory solution. The known methods of particle image velocimetry (PIV) [2] involve basic limitations related to dependence of the results of measurements on the spatial and temporal frequencies of a probing set and, hence, on the concentration of calibrated particles introduced into the medium studied. There are also many unresolved problems related to the processing and identification of particle tracks.

Recently [3], we developed a new method for the laser Doppler imaging and measuring of velocity fields on a real time scale. Based on the optical frequency demodulation of a light field, the proposed method is free of the aforementioned disadvantages inherent in PIV. Below we report on the first realization of the laser Doppler imaging of the velocity field in a gas flow.

As an object for the investigation, we selected a swirling flow in the Rank–Hilsh vortex tube. A considerable interest of researchers in the study of such flows is related to attempts at constructing a physical model adequately describing the energy distribution in swirling flows.

Figure 1 shows a simplified scheme of the experimental setup. The Rank–Hilsh vortex tube represents a channel of a square cross section (34 × 34 mm) with transparent walls. The air flow enters the tube through a slit vortexer. Cold air leaves the tube through a central hole in the plane of the vortexer (at the "cold" tube end). The "hot" tube end represents a radial diffuser, through which the hot air outflows from the tube in radial directions. The tube operated in a regime analogous to that used in the measurements reported previously [4].

A flow cross section to be studied was selected by a "laser knife" probe representing the beam of a He–Ne laser operating on a fundamental mode at a power of 15 mW. The laser knife plane was perpendicular to the horizontal walls of the square tube and made an angle of 60° with the tube axis. The axis of an optical processor forming the image of a flow cross section (selected by the laser knife) was oriented at 30° relative to the laser knife plane. According to the light beam geometry in relation to the tube geometry, the optical processor

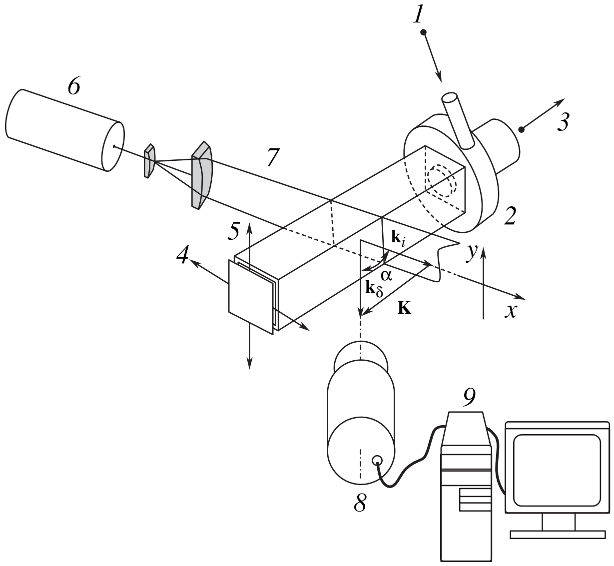

Fig. 1. Schematic diagram of the experimental setup: (*1*) compressed air supply; (*2*) vortexer; (*3*) cold air outflow; (*4*) hot air outflow; (*5*) collimator; (*6*) He–Ne laser; (*7*) laser knife; (*8*) optical processor; (*9*) personal computer.

imaged a spatial distribution of the velocity vector component in the direction determined by a sensitivity vector **K** representing the difference of the wave vectors $\mathbf{k}_s - \mathbf{k}_i$, where $\mathbf{k}_i$ is the wave vector of the incident radiation (forming the laser knife) and $\mathbf{k}_s$ is the wave vector of the scattered radiation in the angular spectrum determined by the optical processor transmission band. The principle of operation of the optical processor was described previously [3]. The transmission function of this processor has a resonance shape. The detection characteristic (discrimination curve) is represented by a linear portion of the decaying branch of the resonance amplitude–frequency characteristic of the optical processor. The mode structure of the processor is matched to that of the laser radiation. A pattern formed in the output plane of the optical processor represents the flow cross section imaged in a frequency-demodulated scattered light. The light field intensity at each point of the image is a single-valued linear function of the projection of the velocity vector onto the sensitivity vector $\mathbf{K} = \mathbf{k}_s - \mathbf{k}_i$.

Indeed, the medium cross section probed by a light wave with the wave vector $\mathbf{k}_i$ is imaged at the optical processor output by a set of images of the scattering optical inhomogeneities $\varphi(\xi, \eta)\delta(x - \xi, y - \eta)$, where (ξ, η) are the coordinates of the optical inhomogeneities in the (x, y) plane of the cross section. Therefore, a frequency-demodulated image of the cross section selected by the laser knife with a wave vector $\mathbf{k}_i$ can be described as

$$\begin{aligned}\omega_D(x, y) &= \gamma\iint \mathbf{K}\mathbf{V}(\xi, \eta)\varphi(\xi, \eta)\delta(x - \xi, y - \eta) \\ &\times d\xi d\eta = \gamma\mathbf{K}\mathbf{V}(x, y)\varphi(x, y),\end{aligned} \tag{1}$$

where the integral is taken over the whole selected cross section; $\omega_D(x, y)$ is the Doppler frequency shift of the light beam forming the point (x, y) in the image at the optical processor output; $\mathbf{V}(x, y)$ is the velocity vector at the point (x, y); and γ is the slope of the discrimination curve of the processor. The factor $\varphi(x, y)$ corresponds to the scattering function in the direction $\mathbf{k}_s$, which describes the primary image of the selected cross section (not subjected to frequency demodulation). Then, the function $\tilde{\omega}_D(x, y) = \dfrac{\omega_D(x, y)}{\gamma\varphi(x, y)} = \mathbf{K}\mathbf{V}(x, y)$ describes the distribution of the relative intensity of the frequency-demodulated image. From this it follows that $\tilde{\omega}_D(x, y)$ provides for a single-valued image of the velocity field component in the direction **K**:

$$V(x, y) = \frac{1}{K}\mathbf{V}(x, y)\mathbf{K}. \tag{2}$$

Figure 2a shows an example of the optical image of a velocity field in the flow cross section selected by the laser knife plane. As can be seen, the velocity field contains dynamically rearranging vortex structures, including double-helix vortices. Figure 2b shows a reconstructed stereo image of the distribution of the projection of the velocity vector $\mathbf{V}(x, y)$ onto the direction of the sensitivity vector **K** (2). Here, the coordinates in the horizontal plane refer to the cross section dimensions (in pixels) selected by the laser knife, while the vertical axis reflect the values of velocity in relative units. In viewing the stereo image, eyes should be accommodated to infinity.

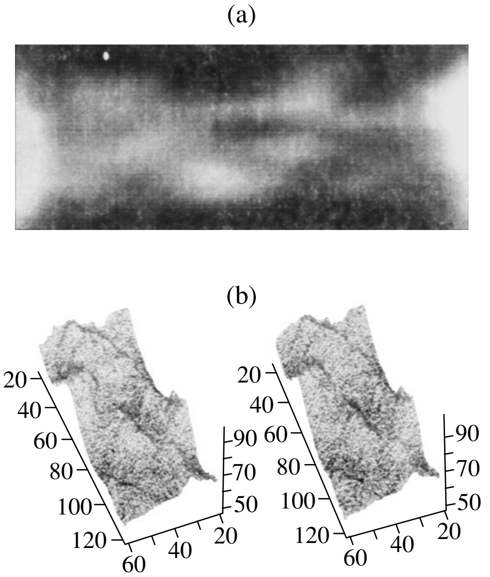

Fig. 2. Laser Doppler imaging of the flow velocity field: (a) a typical image of the swirling flow in a cross section at the hot end of the Rank–Hilsh vortex tube; (b) reconstructed stereo image of the velocity distribution in the selected cross section (for viewing the stereo image, eyes should be accommodated to the infinity).

It is interesting to note that nonhelical wave structures in the velocity field can be put into correspondence with double-helical structures in the field of the optical phase density revealed previously in the same tube under analogous conditions by methods of Hilbert optics [4]. Since the phase density distribution is determined by the pressure and temperature variations, this analogy points to a relation between the dynamic spatial fields of pressure, temperature, and flow velocity in these remarkable configurations observed for the first time using the laser Doppler imaging method.

Performed for the first time, the real-time imaging of a dynamic velocity field determines a qualitatively new level of the optical measuring techniques. The laser Doppler imaging allows us to study nonstationary spatiotemporal distributions of the kinematic parameters, which is necessary for the development of adequate physical models in basic hydro- and gasdynamics.

Acknowledgments. The authors are grateful to N.I. Yavorskii, A.V. Lebedev,[†] M.Kh. Pravdina, V.A. Arbuzov, and V.A. Pavlov for designing and constructing the Rank tube.

The work was supported in parts by the Russian Foundation for Basic Research (project no. 99-02-16702) and by the INTAS Foundation (project no. 00-135).

REFERENCES

1. Yu. N. Dubnishchev and B. S. Rinkevichyus, *Methods of Laser Doppler Anemometry* (Nauka, Moscow, 1982).
2. J. Puvost, J. Legrand, P. Legentilhomme, and L. Doubliez, Exp. Fluids **29**, 291 (2000).
3. P. P. Belousov, P. Ya. Belousov, and Yu. N. Dubnishchev, Kvantovaya Élektron. (Moscow) **29** (2), 157 (1999).
4. V. A. Arbuzov, Yu. N. Dubnishchev, A. V. Lebedev, *et al.*, Pis'ma Zh. Tekh. Fiz. **23** (23), 84 (1997) [Tech. Phys. Lett. **23**, 938 (1997)].

Translated by P. Pozdeev

[†] Deceased.

Technical Physics Letters, Vol. 28, No. 8, 2002, pp. 669–672. Translated from Pis'ma v Zhurnal Tekhnicheskoĭ Fiziki, Vol. 28, No. 16, 2002, pp. 12–19.

A Decrease in the Effective Cross Section of a Cooling Stream Caused by Hot Air Penetration into the Blowout Channel

V. G. Volkov[a], S. O. Shiryaeva[a],*, and V. V. Lebedev[b]

[a] *Yaroslavl State University, Yaroslavl, Russia*

* *e-mail: shir@uniyar.ac.ru*

[b] *Rybinsk State Academy of Aviation Technology, Rybinsk, Russia*

Received February 1, 2002

Abstract—The phenomenon of penetration of a hot air stream into a channel of finite depth by which a cooling stream is injected was revealed and studied by numerical methods. The penetrating stream decreases the effective cross section of the cooling stream, increases the velocity of this stream, and reduces the near-wall gas screen cooling efficacy. *© 2002 MAIK "Nauka/Interperiodica".*

Introduction. Previously, the character of flow and heat exchange processes accompanying the efflux of a submerged cold stream from a channel of finite depth into a hot main stream were studied by methods of numerical modeling in a flat case. It was established that separation (detachment) of the cooling stream leads to penetration of the hot main stream into the side channel. This phenomenon influences the gas screen formed downstream at the channel output. The effect was experimentally observed in the case of channels with output diameters about ten times greater than those used for the gas screen cooling purposes [1]. Since it is rather difficult to study this phenomenon experimentally in the case of narrow channels (with a diameter below 1 cm), a valuable alternative is offered by methods of numerical modeling.

In the numerical modeling of a stream outflowing from a side channel of finite depth, it is very important to set correct boundary conditions at the channel bottom, because this factor significantly influences the results of modeling [2]. The typical wall thickness of a cooled turbine blade is such that the depth of channels through which the cooling air is supplied to the near-wall hot stream to form a gas screen does not exceed 2–6 channel diameters. The coolant flow through such a hole exhibits separation, whereby the outflowing stream does not fill the whole channel cross section [3], which leads to certain features in setting the boundary conditions.

Bogomolov [4] described possible regimes of the efflux of an infinite stream, passing under a wall with a transverse slit possessing sharp edges and finite depth (also referred to below as the hole), into a space above the wall. Depending on the efflux regime, determined by the ratio of the velocity of unperturbed coolant stream under the wall to the stream velocity at the hole output, the rate of flow through the hole may significantly vary. The results were obtained by applying formalism of the theory of functions of a complex variable to a flat potential flow of incompressible fluid. In this context, it was of interest to study the character of flow through the hole on the near-wall gas screen formed downstream at the coolant blowout channel. The problem of modeling the efflux of a submerged stream passing, via a channel of finite depth in a solid wall, from a stream under the wall into a viscous compressible turbulent flow above the wall has not yet been solved in the general case.

Problem formulation and solution. Let us consider the formation of a gas screen by a coolant stream injected into the main stream at an angle of 90° from a rectangular slit with a width h and a depth L. The problem to be solved is mathematically formulated in [4] as a complete system of Navier–Stokes equations with necessary boundary conditions (see [2, 5, 6]). Inhomogeneous boundary conditions with respect to the outflowing stream velocity will be set at the side channel input in two variants, representing either a homogeneous velocity distribution (by analogy with the cases studied in [2]) or an inhomogeneous distribution. The coolant stream outflows from a channel with the relative depth $L/h = 2$. The boundary conditions will be selected for the case of a shock-free inflow of the coolant into the channel (without the formation of recirculation zones). For this purpose, we use a complex flow potential derived in [4] and determine the flow velocity projections U and V onto the axes X and Y, respectively, at $Y = 0$ (i.e., at the channel input).

The calculations are performed using a program based on the solution of a complete system of Navier–Stokes equations (averaged according to Reynolds). The program was described elsewhere [5, 6] together

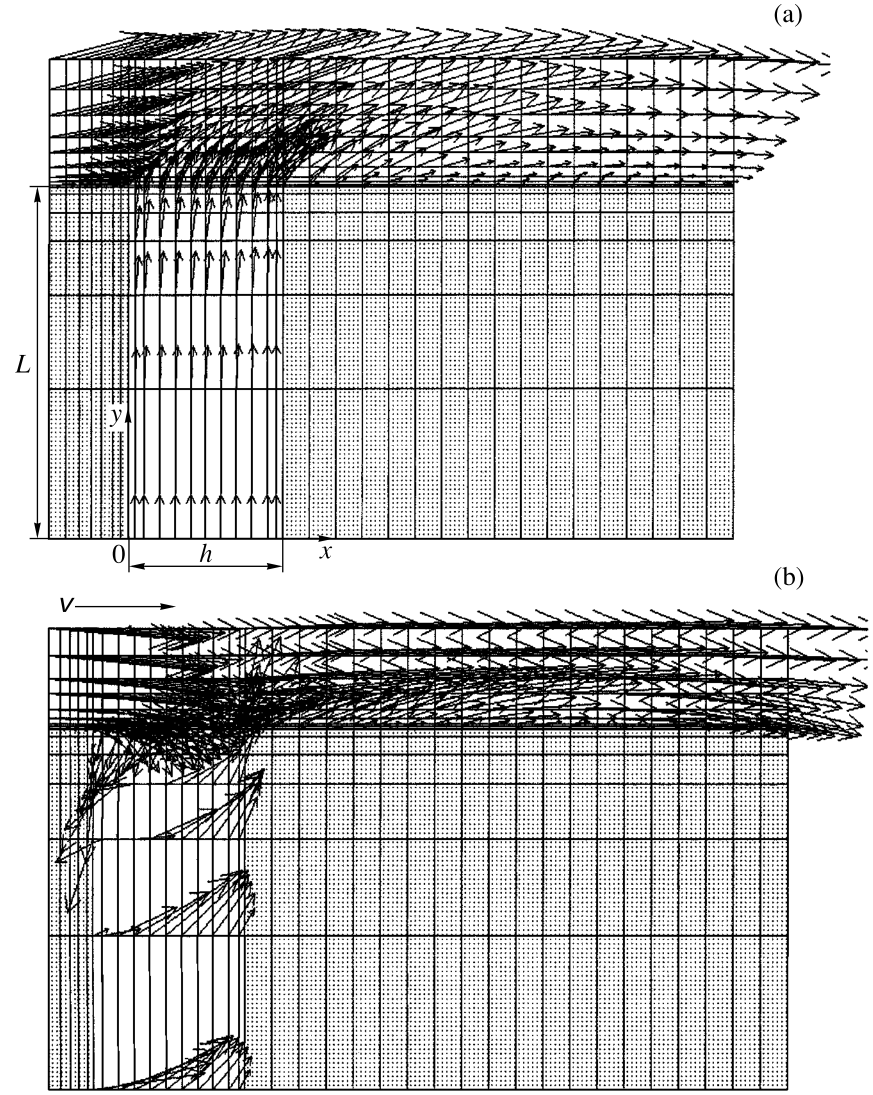

Fig. 1. Velocity fields calculated for (a) homogeneous and (b) inhomogeneous coolant velocity profiles at the input of a slit channel ($m = 1$).

with the boundary conditions for the main stream. The walls are maintained under adiabatic conditions ($\partial T/\partial n = 0$). The solutions were obtained for the Mach number $M_0 = 3$ of the hot main stream at the entrance into the region under consideration and the Reynolds number Re = 3300 (determined using the main stream velocity and the slit width h). The calculated regimes were determined by the injection parameter $m = 0.5$ or 1. The injection parameter (equal to the ratio of the coolant flux density at the channel output to the hot main stream density at the entrance into the region under consideration) was determined from the coolant flow rate. The density and velocity of the hot flow at the entrance into the region under consideration were taken equal to unity. The ratios of the initial temperatures of the cold and hot flows were taken equal to 0.5. The solutions were obtained in a dimensionless form.

The numerical modeling procedure was based on a difference scheme obtained using the conventional methods of control volumes, compressibility scaling, and splitting. The difference scheme was of the second order of accuracy with respect to the spatial variable and of the first order of accuracy with respect to the time variable. The problem was solved in a nonuniform lattice with 36 sites along the X axis, 38 sites along the Z axis, and 88 sites along the Y axis, the total number of sites being 120400. The spatial step was minimum ($dZ = 0.00095$) at the solid wall (in order to adequately describe the boundary layer) and maximum ($dY = 0.1$) at the periphery (i.e., at the upper and exit faces of the region under consideration). The lattice site density increased in the local regions of intense variation of the flow parameters.

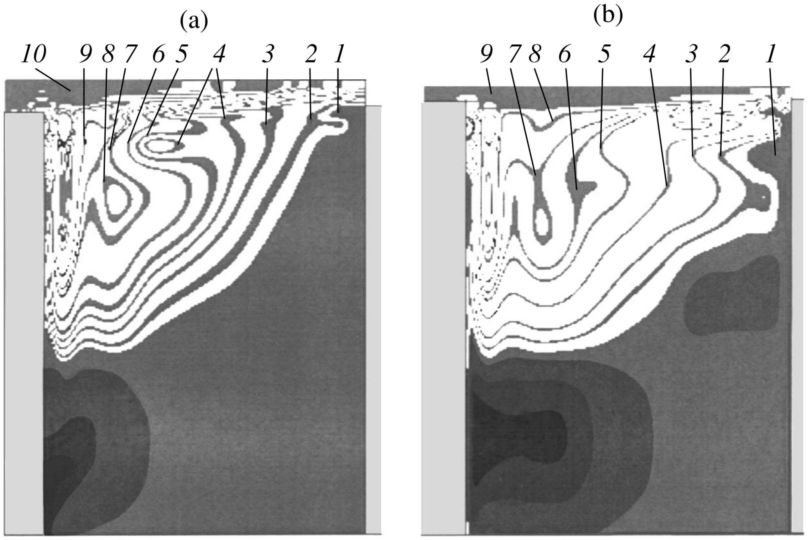

Fig. 2. Temperature fields in a slit channel with separating coolant flow: (a) $m = 0.5$, $T = 0.5$ (*1*), 0.53 (*2*), 0.55 (*3*), 0.59 (*4*), 0.61 (*5*), 0.66 (*6*), 0.77 (*7*), 0.8 (*8*), 0.85 (*9*), 1 (*10*); (b) $m = 1$, $T = 0.5$ (*1*), 0.55 (*2*), 0.59 (*3*), 0.69 (*4*), 0.78 (*5*), 0.82 (*6*), 0.88 (*7*), 0.97 (*8*), 1 (*9*).

Figure 1 shows the results of the flow calculation in the form of velocity field fragments for the injection parameter $m = 1$ in both variants of the velocity profile at the channel input. As can be seen, a characteristic feature of the velocity field in the stream outflowing from the side channel for the inhomogeneous input profile is penetration of the hot main stream into the hole, with the formation of a circulating flow. This leads to narrowing of the effective cross section of the coolant stream. Since the total flow rate is constant (according to the boundary conditions adopted at the channel input), the stream velocity at the channel output increases. Thus, the process of convective heat exchange between cold and hot streams begins already in the channel. This results from the coolant flow separation at the channel output. A similar pattern is observed for $m = 0.5$.

Figure 2 shows isotherms of the temperature field in the channel for $m = 0.5$ and 1 in the case of an inhomogeneous input profile. The presence of isotherms with a temperature above 0.5 is evidence of the mixing of the cold coolant with the hot main stream penetrating into the channel at the upper left edge. As can be seen, an increase in the injection parameter m from 0.5 to 1 increases the amount of hot medium entering the channel and intensifies heat exchange in the channel. This is evidenced by expansion of the region of temperatures above 0.5 and by general elevation of the temperature levels.

Discussion. The screen cooling efficacy is characterized by a relative temperature of the adiabatic wall, which is determined by the formula

$$\theta = \frac{T_h - T_w}{T_h - T_c},$$

where T_h, T_c, and T_w are the absolute temperatures of the hot and cold streams and the wall, respectively. Figure 3 shows distributions of the screen cooling efficacy for the various flow conditions considered above. As can be seen, the initial efficacy θ for the separated flow (curve *2*) is lower than that for the flow without separation (curve *1*) irrespective of the injection parameter.

The observed behavior is explained (i) by an increase in the coolant temperature taking place in the channel as a result of mixing with the hot stream and (ii) by displacement of the coolant stream from the wall more deeply into the main stream as a result of increasing coolant velocity (due to the total flow rate conservation). These effects account for the nonmonotonic character of curve *2* in Fig. 3, corresponding to the case of $m = 1$. Note that the results of calculations with $m = 0.5$ and various boundary conditions are close because the main stream perturbations induced by the coolant blowout rapidly decay downstream. The results for $m = 1$ are

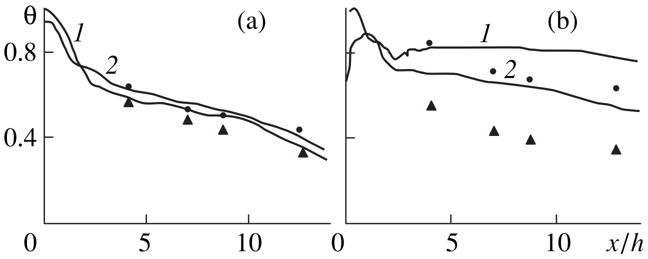

Fig. 3. Profiles of the screen cooling efficacy θ downstream at the channel output (x is the distance from the slit, h is the slit width) calculated for a “thin” boundary layer assuming (*1*) homogeneous and (*2*) inhomogeneous boundary conditions at the channel input. The points representing experimental data refer to (●) “thin” and (▲) “thick” boundary layers: (a) $m = 0.5$; (b) $m = 1$.

significantly different, which is related to the essentially altered dynamics of interaction of the coolant stream and the hot main stream.

For comparison, Fig. 3 presents the experimental data obtained for a flat plate (Re = 1800, $M_0 = 0.056$) and a coolant stream injected through a vertical slit. Our data refer to the case of a "thick" boundary layer, developed over a region with the relative length x/h = 30 in front of the injected stream (x is the distance to the slit and h is the slit width). Data for a "thin" boundary layer with x/h = 3–4 were taken from [7]. The calculations were performed only for the case of a "thin" boundary layer with x/h = 3.5 (by "thick" layers we imply those with a thickness comparable to exceeding the slit width h). As is known, the boundary layer strongly affects the formation of a near-wall gas screen and determines the screen efficacy, the effect increasing with the injection parameter [6]. As can be seen, the results of calculations for $m = 0.5$ using the boundary conditions of both types show a satisfactory agreement with experimental data for both thin and thick layers (cf. curves and experimental points in Fig. 3a). For m = 1, the results of calculations with inhomogeneous boundary conditions (Fig. 3b, curve *2*) agree quite satisfactorily with the experiment involving a "thin" boundary layer on the plate. Moreover, the theoretical curve correctly reflects the character of variation of the screen efficacy θ with the coordinate x/h (the curve equidistantly follows the experimental data).

Conclusion. In modeling the process of coolant efflux from a wall channel of finite depth into a transverse stream passing by the wall and the formation of a near-wall gas screen downstream at the blowout hole, it is necessary to take into account the coolant stream separation at the channel output. This is provided by correctly selecting the boundary conditions at the channel input or (if these conditions are unknown) by expanding the calculation region so that the lattice would include internal sites at the channel input and by placing the lattice boundaries where the boundary conditions can be either exactly or approximately set.

REFERENCES

1. R. J. Goldstein, P. Jin, and R. L. Olson, J. Turbomach. **121**, 225 (1999).
2. V. G. Volkov and V. V. Lebedev, in *Proceedings of the XIII School-Workshop of Academician A.I. Leont'ev for Young Scientists and Specialists "Physical Principles of Experimental and Mathematical Simulation of Gas Dynamics and Heat and Mass Transfer in Power Plants," St. Petersburg, 2001* (Mosk. Énerg. Inst., Moscow, 2001), Vol. 1, p. 61.
3. S. Friedrichs, H. P. Hodson, and W. N. Daves, J. Turbomach. **119**, 786 (1997).
4. E. N. Bogomolov, Prikl. Mekh. **4** (10), 105 (1968).
5. V. G. Volkov, V. V. Lebedev, and S. O. Shiryaeva, Pis'ma Zh. Tekh. Fiz. **28** (2), 67 (2002) [Tech. Phys. Lett. **28**, 70 (2002)].
6. V. G. Volkov, V. V. Lebedev, and S. O. Shiryaeva, Pis'ma Zh. Tekh. Fiz. **28** (4), 87 (2002) [Tech. Phys. Lett. **28**, 167 (2002)].
7. N. N. Kortikov and Yu. A. Smirnov, Inzh.-Fiz. Zh. **48** (5), 715 (1983).

Translated by P. Pozdeev

Technical Physics Letters, Vol. 28, No. 8, 2002, pp. 673–674. Translated from Pis'ma v Zhurnal Tekhnicheskoĭ Fiziki, Vol. 28, No. 16, 2002, pp. 20–24.
Original Russian Text Copyright © 2002 by Melikyan, Itin.

Dynamics of Bone Tissue Mineralization in Porous Titanium and the Mechanical Properties of a Titanium–Bone Tissue Composite

M. L. Melikyan and V. I. Itin

Structural Macrokinetics Department, Tomsk Scientific Center, Siberian Division, Russian Academy of Sciences, Tomsk, Russia

Received February 21, 2002

Abstract—We studied the dynamics of bone tissue mineralization in the pores of a titanium matrix and the mechanical properties of the resulting titanium–bone tissue composite. It is shown that the mineralization process is virtually accomplished within six months after implantation of a porous titanium article into the organism. As the pores and channels in the titanium matrix are filled with bone tissue, the material becomes a composite with mechanical properties higher as compared to those of the porous implant or bone tissue. *© 2002 MAIK "Nauka/Interperiodica".*

Porous permeable matrices of titanium and related alloys are used in medicine in the form of implants substituting tissues of the organism. The living tissues readily grow into the porous space and gradually fill all pores in the implant [1, 2]. Porous coatings are also applied onto endoprostheses of the hip joints and various dentures, which eventually ensures a tight contact between an implant and the recipient bone [2–4].

Data on the dynamics of bone tissue growth through porous permeable titanium and the mechanical behavior of the resulting titanium–bone tissue composite were previously reported in [5]. In this study, we monitored the dynamics of mineralization (i.e., variation of the chemical composition) of the bone tissue in the implant pores and determined mechanical characteristics of the titanium–bone tissue composites with various volume ratios of the metal and the bone tissue.

The implants were modeled by cylindrical samples, 4 mm in diameter and 4 mm in length, cut using an electroerosion tool from porous titanium blanks synthesized from a titanium powder of the PTEM2 grade by sintering in the regime T_1 = 960°C, t_1 = 2 h; T_2 = 1350°C, t_2 = 4 h [5]. The powder was preliminarily separated by sieving into fractions so as to obtain sintered materials with an open porosity of 44–47, 59–66, and 78–80%. A considerable proportion of pores possess diameters within 100–300 μm, which are considered optimum for bone tissue growth.

Experiments on the growth of bone tissue into the porous structure of titanium implants were performed on chinchilla rabbits weighing 3–3.5 kg. The animals were narcotized with thiopental sodium (3.5 mg/kg) and operated on, whereby a 4- to 5-cm-long cut was made in the pelvis region, the soft tissues were detached from the bone, and four holes were made with a 2-mm hard-alloy drill. Then, the diameters of holes were increased to 4 mm using special bores and the titanium implants were positioned in the holes. The operation wounds were thoroughly closed with a catgut suture, and the animals were treated with bicillin (500 U/kg). The test animals were killed by air embolism on the 7th, 14th, and 21st day and 1, 2, 3 and 6 months after sample implantation. The samples for histological examination were prepared by cutting bone blocks with implants and fixing tissues in a 1% glutaraldehyde solution. The bone sections were studied by electron microscopy and by electron-probe microanalysis (EPMA) on a REMMA-202M setup. Then the implants were extracted and mechanically tested in the compression mode. The static tests were conducted in an Instron 1185 test machine operated at a straining rate of 0.5 mm/min. The test results were evaluated in terms of the true compression stresses and expressed as the ultimate strength and the relative strain at break.

The electron-microscopic examination confirmed the analogous data of other researchers and the results obtained by optical microscopy [4]. The growth of bone tissues begins with a capillary impregnation of the porous titanium matrix with physiological fluids carrying the cells. The cells attach to the pore surface coated with titanium dioxide (TiO_2) and give rise to tissue formation. The bone tissue nucleates and grows simultaneously in many pores in the form of nuclei (domains) which increase in size and gradually fill the pores. This process gives rise to a flow of tissue from the bulk to the external surface of the implant. However, in addition to this outward flow reported previously, we observed a flow of the tissue growing from the external surface inward the implant. As a result, the porous space in the implant is filled with the tissues.

The degree of mineralization of the tissues grown in the pores was determined by EPMA (Fig. 1), which

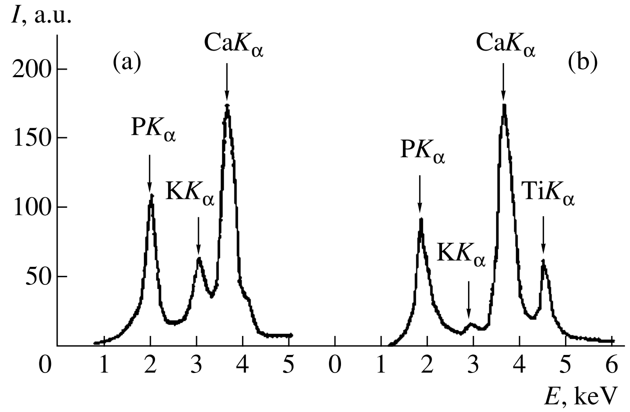

Fig. 1. The energy-dispersive spectra of tissues (a) in an intact hip joint bone of a rabbit and (b) in the pores of a titanium implant (one month after implantation) with a initial porosity of 66%.

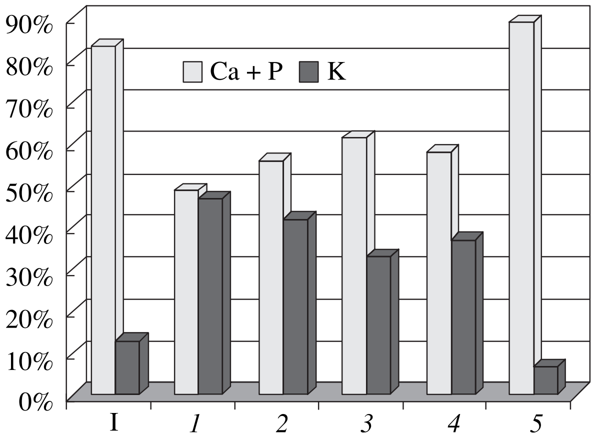

Fig. 2. Variation of the relative content of calcium plus phosphorus and potassium in the pores of a titanium implant (with an initial porosity of 66%) with the time of occurrence in the organism of a rabbit: (*1*) 21 day; (*2*) 1 month; (*3*) 2 months; (*4*) 3 months; (*5*) 6 months; (I) intact bone tissue.

provided data on the concentrations of the main chemical elements in the tissues. By measuring the content of potassium, it is possible to judge the presence of cells because the potassium concentration is much greater in the cell cytoplasm than in the tissue fluid (representing an isotonic solution of sodium chloride). The concentrations of phosphorus and calcium (relative to the content of these elements in natural bones) is a measure of the degree of mineralization of the newly formed tissues.

Investigation of the dynamics of tissue growth through the porous implant structure and of the degree of mineralization by methods of electron microscopy and EPMA showed (Fig. 2) that tissues of variable contrast (density) are formed within 21–30 days in the pores of the titanium matrix. The newly formed tissues include bone tissue characterized by clear intense peaks of potassium, phosphorus, and calcium in the energy-dispersive spectra. The relative total content of phosphorus and calcium in this tissue amounts to 50% at a high potassium concentration. The degree of mineralization is higher for tissues in the pores near the surface than in the central part of the implant. As the duration of implant occurrence in the organism increases to 6 months, intensity of the phosphorus and calcium peaks in the spectra increases, while intensity of the potassium peaks drops. The relative content of the three elements in all pores at this time corresponds to mature natural bone tissue (Fig. 2). The porous space of the implant is filled up to approximately 90% by the bone tissue, which penetrates into all bends of the pores.This provides for a tight mechanical linkage between bone and implant over the entire tissue–metal interface.

Testing the mechanical properties of composites with various content of bone tissue, approximately corresponding to the porosity of the initial titanium matrix, showed that, after a 6-month exposure, maximum true yield stresses (ultimate strength for compression, 460 MPa) and relative strain at break (about 32%) were inherent in the samples with an initial porosity of 44–47%, while minimum values of these characteristics (ultimate strength, 160 MPa; relative strain at break, 17.5%) were observed in the samples with an initial porosity of 78–80%. Implants with an initial porosity of 59–66% exhibited intermediate results, with an ultimate strength of 220 MPa and a relative strain at break of about 20%. We may suggest that the key role in determining the maximum mechanical strength of the titanium–bone tissue composites is played by the metal component. A significant degradation of the mechanical properties with increasing proportion of bone tissue in the composite is related to the biological component of the composite.

The results of our investigation showed that a porous permeable titanium matrix, with the pores and channels gradually filled by the newly formed bone tissue, converts into a high-strength composite with the mechanical properties significantly higher as compared to those of the porous implant [5] or bone tissue [6].

REFERENCES

1. V. É. Gyunter, V. I. Itin, L. A. Monasevich, *et al.*, *Effects of Shape Memory and Their Application in Medicine* (Nauka, Novosibirsk, 1992).
2. M. Z. Mirgazizov, V. É. Gyunter, V. I. Itin, *et al.*, *Superelastic Implantates and Constructions from Alloys with Shape Memory in Stomatology* (Quintessenz Verlags-GmbH, Moscow, 1993).
3. R. M. Pilliar, J. Biomed. Mater. Res. **21** (A1), 1 (1987).
4. T. I. Barmina, V. G. Stepanov, A. B. Andrusov, *et al.*, Metally, No. 2, 136 (1994).
5. V. I. Itin, V. É. Gyunter, V. N. Khodorenko, *et al.*, Poroshk. Metall., No. 9/10, 29 (1997).
6. V. A. Berezovskiĭ and N. N. Kolotilov, *Biophysical Characteristics of Human Tissues: a Handbook* (Naukova Dumka, Kiev, 1990).

Translated by P. Pozdeev

Technical Physics Letters, Vol. 28, No. 8, 2002, pp. 675–677. Translated from Pis'ma v Zhurnal Tekhnicheskoĭ Fiziki, Vol. 28, No. 16, 2002, pp. 25–31.
Original Russian Text Copyright © 2002 by Barannik, Shabanov, Zyryanov.

Interference Oscillations in the Dynamics of the Optical Response of Polymer Dispersed Nematic Liquid Crystals

A. V. Barannik, A. V. Shabanov, and V. Ya. Zyryanov
Kirensky Institute of Physics, Siberian Division, Russian Academy of Sciences, Krasnoyarsk, Russia
e-mail: zyr@iph.krasn.ru

Received March 11, 2002

Abstract—The dynamics of the optical response of a polymer-dispersed nematic liquid crystal under the action of electric field pulses was experimentally studied for film samples differing in the size of nematic droplets. The optical signal relaxation curve exhibits an oscillating character, with the number of oscillations determined by the transverse size of the nematic droplets. The interference character of the signal oscillations is confirmed by an analysis of the oscillating response within the framework of the anomalous diffraction approximation and by a comparison with the dependence of the transmitted light intensity on the applied voltage measured in a static regime. *© 2002 MAIK "Nauka/Interperiodica".*

Previously [1–6], we discovered and studied oscillations in the dependence of the optical transmission of polymer-dispersed nematic liquid crystal (PDNLC) films on the applied voltage. These oscillations are caused by interference of the light transmitted between the liquid crystal (LC) droplets and the light scattered from the droplets in the forward direction. Reorientation of the LC director inside the droplets under the action of an electric field applied to the PDNLC film leads to a change in the phase shift between the interfering light rays and, hence, to oscillations in the dependence of the transmitted radiation on the applied voltage. The number of oscillations (extrema) on the transmitted intensity curve is proportional to the transverse (i.e., normal to the film plane) size of the droplets. The experiments reported in [1–6] were performed in a static regime, whereby the voltage sweep time (10 s and above) was significantly greater than the characteristic time of reorientation of the nematic droplets (1–10 ms). Under these conditions, the oriented structure of the nematic droplets passes, in the course of increasing field strength, through a sequence of equilibrium states from a bipolar configuration of the LC director to the state of saturation, in which the LC director is oriented parallel to the field nearly the whole droplet volume.

Technical applications, such as spatial light modulators used in flat displays and the data recording, storaging, and processing devices, typically employ discrete addressing based on the high-frequency pulsed electric field action upon discrete elements of a shutter. In this context, it is important to study the contribution of the interference component to the optical response of PDNLC films measured in a dynamic regime, in which case the time of electric signal switching is much smaller as compared to the characteristic time of reorientation of the nematic droplets.

The samples of PDNLC films were prepared by a conventional method based on the phase separation of a homogeneous solution of the liquid crystal and prepolymer components, initiated by photocuring of the polymer matrix [7]. The composition components were an optical adhesive of the NOA-65 type (Norland Products Inc.) and a nematic mixture of cyanobiphenyl derivatives [8] taken in a 1 : 1 mass ratio. The initial solution was placed into a gap between glass plates with transparent electrodes, the film thickness being determined by 10-μm spacers. During the subsequent treatment, the total power of a mercury lamp was varied from 1 to 10 mW/cm^2. The sample was separated into several regions, each processed using a certain photocuring regime (temperature and radiation intensity). By varying these technological parameters, it was possible to change morphological characteristics of the final sample structure. As a result, the average nematic droplet size in various regions of a sample film varied from 1 to 10 μm. Within a certain region of the composite film, the deviation of the nematic droplet size from the average did not exceed 40%.

Investigations of the sample texture by means of a polarization microscope showed that the internal oriented structure of the nematic droplets corresponds to a bipolar configuration of the LC director. The symmetry axes, connecting two poles of the droplet, are oriented predominantly in the film plane and exhibit random azimuthal orientations. It should be noted that the symmetry axes of small droplets may slightly deviate from the film plane, because the shape of such droplets is close to spherical. Large droplets are significantly oblate, with the transverse size being 1–2 μm smaller than the lateral dimensions (in the film plane). In droplets of this shape, a minimum of the elastic energy is attained

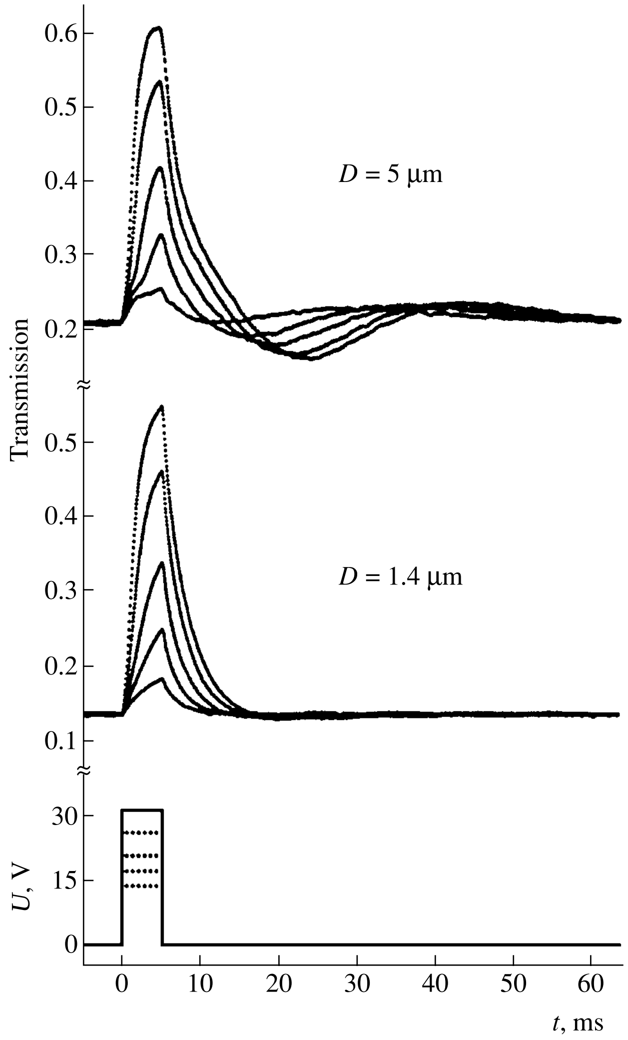

Fig. 1. Oscillograms of the optical transmission signal from two regions of a composite polymer film containing nematic droplets with different average size D, observed in response to a single control voltage pulse (bottom diagram) with an amplitude of 14.0, 17.5, 21.0, 26.3, and 31.5 V (bottom to top).

for the symmetry axes parallel to the long axes of droplets [9] that aligned in the film plane.

The electrooptical characteristics were studied using the monochromatic radiation of a He–Ne laser operating at $\lambda = 0.633$ μm. The volt–contrast characteristics were measured using a slowly varying (~1 V/s) amplitude of the alternating (500 Hz) voltage applied to the cell electrodes. We studied the dynamics of the optical response of the PDNLC films as a function of the amplitude of single rectangular electric pulses with a duration of 5 ms.

Figure 1 presents oscillograms of the optical response for two PDNLC film regions differing in nematic droplet size and shows the shape of the control electric pulse. The sample containing small nematic droplets exhibits monotonically decaying, nearly exponential curves of the transmitted light intensity variation after switching off the applied voltage. The curves of signal relaxation observed for the sample with large nematic droplets exhibit a significantly different nonmonotonic behavior, whereby the transmitted light intensity decreases, exhibits a minimum, increases again, passes through a local maximum, and then gradually decreases to the initial level. The position of minimum on the time scale, as well as the total relaxation time, depend on the electric pulse amplitude. This is explained by the fact that a more pronounced transformation of the oriented droplet structure requires a longer relaxation time. At the point of minimum, the transmitted light intensity is lower than that in the initial state (before the application of electric pulse). It is interesting to note that the depth of the minimum (i.e., the difference of optical transmission in the initial state and at the point of minimum) increases with the control pulse amplitude.

For comparison, Fig. 2 shows variation of the transmitted light intensity in response to the applied voltage for the same sample regions measured in a static regime. The curve for the PDNLC containing small nematic droplets exhibits a classical S-like shape [7]. No threshold behavior with a bending point corresponding to the Fréedericksz critical field is observed in this case, which is explained, as noted above, by the presence of nematic droplets with the symmetry axes oriented at an angle with respect to the film plane. Violation of the condition of orthogonality of the axes of a bipolar LC director configuration and the applied field direction [2–4] is just what leads to a thresholdless shape of the volt–contrast characteristic. This situation is typical of composite films in which the nematic droplet size is significantly smaller than the film thickness. In contrast, the orthogonality condition holds better for the film containing large droplets, as manifested by a threshold character of the optical transmission variation in this sample region (Fig. 2). This curve displays additional minimum and maximum resembling those observed in the dynamic regime (Fig. 1).

Now let us use an analytical approach developed previously [2–5] for explaining the observed interference oscillations of the volt–contrast characteristic. The relative phase shift of the interfering light rays is determined by the ratio of the difference in the optical paths to the light wavelength: $\Delta nD/\lambda$, where $\Delta n = n_{\mathrm{lc}} - n_{\mathrm{p}}$, n_{lc} is the refractive index for an extraordinary ray in the liquid crystal and $n_{\mathrm{p}} \simeq 1.52$ is the refractive index of the polymer matrix. The refractive index for the extraordinary ray, depending on the mutual orientation of the electric vector of the light wave and the LC director, varies in the given nematic composition from $n_{\mathrm{lc}}^{\min} \simeq 1.52$ to $n_{\mathrm{lc}}^{\max} \simeq 1.72$. In the saturation state (corresponding to the maximum transmission in Figs. 1 and 2), the LC director is perpendicular to the electric field vector of the light beam, $\Delta n = n_{\mathrm{lc}}^{\min} - n_{\mathrm{p}} = 0$, and, hence, the

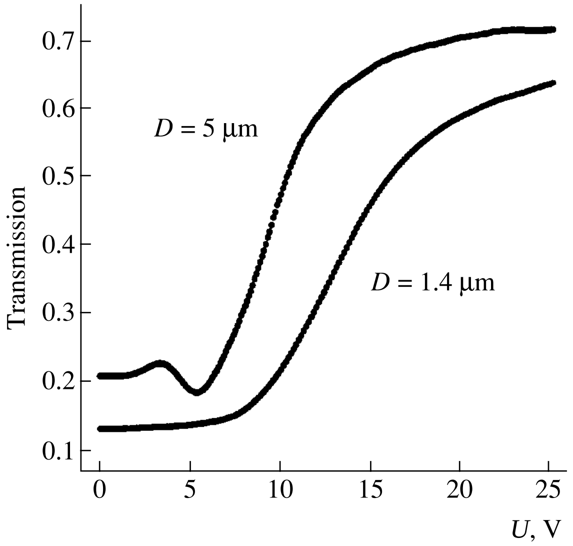

Fig. 2. Variation of the optical transmission depending on the applied voltage, measured in the static regime for the same regions of the composite film as in Fig. 1.

phase shift is zero. As the applied voltage decreases (Fig. 2), the birefringence increases and, at a certain point, the optical path difference ΔnD reaches $\lambda/2$. This condition corresponds to the first minimum in the volt–contrast characteristic. As the applied voltage droplets further, the path difference crosses a level of $\Delta nD = \lambda$, which corresponds to the first local maximum. The relation $\Delta nD = 3\lambda/2$ corresponds to the second minimum in the transmission, and so on.

The transverse size of small nematic droplets amounts on the average to 1.4 μm. In this case, the maximum possible optical path difference is $\Delta n^{\max}D = 0.2 \times 1.4$ μm $= 0.28$ μm $< \lambda/2$. For such small LC droplets dispersed in the polymer matrix, no oscillations can be observed in the optical transmission curves (Fig. 1 and 2).

For large nematic droplets with a transverse size of 5 μm, the optical path difference is $\Delta n^{\max}D = 0.2 \times 5$ μm $= 1.0$ μm $\approx 3\lambda/2$. Therefore, relaxation of such droplets into the initial state after switching off the electric pulse (Fig. 1) or with decreasing applied voltage (Fig. 2) will result in the transmission sequentially passing through the first minimum, maximum, and second minimum, and attaining saturated initial (zero field) state, in agreement with the experimental observations.

Thus, we reported for the first time the results of investigation of the oscillating character of the optical response relaxation observed upon application of a rectangular electric pulse to the film of a polymer-dispersed nematic liquid crystal. An analysis of the experimental results presents convincing evidence of the interference nature of these oscillations. It should be noted that the dynamic pattern of the optical response of composite films in the general case can be extremely complicated as a result of the interplay of various effects including, for example, the influence of an electric field of the spatially separated impurity ions [10, 11], the formation of defects and domains [12, 13], restructurization of the droplet–polymer interphase boundary [8, 14], etc. In this context, the results presented above show the importance of taking into account the interference effects during complex analysis of the dynamic characteristics of composite films.

Acknowledgments. This study was partly supported by the Ministry of Science and Technology and the Ministry of Education of the Russian Federation and by the Krasnoyarsk Regional Science Foundation.

REFERENCES

1. V. Ya. Zyryanov, V. V. Presnyakov, and V. F. Shabanov, Pis'ma Zh. Tekh. Fiz. **22** (14), 22 (1996) [Tech. Phys. Lett. **22**, 563 (1996)].
2. A. V. Shabanov, V. V. Presnyakov, V. Ya. Zyryanov, *et al.*, Pis'ma Zh. Éksp. Teor. Fiz. **67** (9), 696 (1998) [JETP Lett. **67**, 733 (1998)].
3. A. V. Shabanov, V. V. Presnyakov, V. Ya. Zyryanov, *et al.*, Mol. Cryst. Liq. Cryst. **321**, 245 (1998).
4. V. V. Presnyakov, V. Ya. Zyryanov, A. V. Shabanov, *et al.*, Mol. Cryst. Liq. Cryst. **329**, 27 (1999).
5. A. V. Konkolovich, V. V. Presnyakov, V. Ya. Zyryanov, *et al.*, Pis'ma Zh. Éksp. Teor. Fiz. **71** (12), 710 (2000) [JETP Lett. **71**, 486 (2000)].
6. V. Ya. Zyryanov, V. V. Presnyakov, A. N. Serebrennikov, *et al.*, Mol. Cryst. Liq. Cryst. **368**, 3983 (2001).
7. G. M. Zharkova and A. S. Sonin, *Liquid-Crystalline Composites* (Nauka, Novosibirsk, 1994).
8. A. V. Barannik, S. L. Smorgon, V. Ya. Zyryanov, and V. F. Shabanov, Opt. Zh. **64** (5), 99 (1997) [J. Opt. Technol. **64**, 486 (1997)].
9. A. V. Koval'chuk, M. V. Kurik, O. D. Lavrentovich, *et al.*, Zh. Éksp. Teor. Fiz. **94** (5), 350 (1988) [Sov. Phys. JETP **67**, 1065 (1988)].
10. O. A. Afonin, V. F. Nazvanov, and A. V. Novikov, Pis'ma Zh. Tekh. Fiz. **15** (6), 33 (1989) [Sov. Tech. Phys. Lett. **15**, 220 (1989)].
11. V. A. Zhuikov, V. F. Shabanov, G. M. Zharkova, *et al.*, Mol. Cryst. Liq. Cryst. **179**, 377 (1990).
12. E. Shimada and T. Uchida, Jpn. J. Appl. Phys. **31**, L352 (1992).
13. P. S. Drzaic, Liq. Cryst. **3** (11), 1543 (1988).
14. D. Cupelli, M. Macchione, F. P. Nicoletta, *et al.*, Appl. Phys. Lett. **76** (20), 2856 (2000).

Translated by P. Pozdeev

Technical Physics Letters, Vol. 28, No. 8, 2002, pp. 678–679. Translated from Pis'ma v Zhurnal Tekhnicheskoĭ Fiziki, Vol. 28, No. 16, 2002, pp. 32–36.
Original Russian Text Copyright © 2002 by Zolotukhin, Golev, Popov, Ievlev.

Thermoelectric Properties of Nanotubular and Fractal Carbon Deposits

I. V. Zolotukhin, I. M. Golev, A. A. Popov, and V. P. Ievlev
Voronezh State Technical University, Voronezh, Russia

Received March 18, 2002

Abstract—The structure and thermo emf of nanotubular and fractal carbon layers deposited from an electric discharge plasma were studied. The thermo emf of such nanotubular and fractal deposits is almost tenfold higher as compared to that of polycrystalline carbon, which is explained by the nanostructural state of carbon in the deposits studied. © *2002 MAIK "Nauka/Interperiodica".*

To the present, the kinetic properties of many materials with mono- and polycrystalline and amorphous structures have been well studied and have reached limiting values. Further increase in the kinetic properties can be expected only in cases when the structural state of a substance is basically changed. From this standpoint, promising results can be anticipated in systems possessing fractal and nanotubular structures.

As is known, fractal structures in solids are usually formed in open systems under conditions of high energy dissipation. Under such thermodynamically nonequilibrium conditions, atoms and molecules exhibit self-organization into particles or clusters of nanometer dimensions and eventually form fractal aggregates. The characteristic features of these aggregates are structural hierarchy, self-similar (automodel) character, scale invariance, low density, and the presence of nanodimensional porosity.

Here we report the results of studying the thermo emf in carbon deposits possessing fractal and nanotubular structures.

Carbon deposits with a fractal structure were obtained in the course of sputtering graphite of a special purity grade (OSCh-7-3) in an electric arc. The process was conducted in an argon atmosphere at a pressure of P = 300–400 Torr, a current density of j = 1100–1250 A/cm^2, and a voltage of U = 20–25 V. The deposition time was varied from 30 to 120 s. The nanotubular deposits were obtained by sputtering the same graphite in the electric arc in a helium atmosphere at P = 500 Torr, j = 65–75 A/cm^2, and U = 20 V. The deposition time was 900–1800 s. Compact carbon layers with a thickness of 1–1.5 mm were separated from a polished graphite cathode surface and characterized by various methods. The surface structure of the deposited layer was studied in a REM-300 scanning electron microscope (SEM). The density of the samples, determined by hydrostatic weighing with an uncertainty of 3–5%, was 1.32 and 1.7 g/cm^3 for the fractal and nanotubular deposits, respectively. For comparison, we studied samples of mono- and polycrystalline (grain size, 20–50 μm) graphite with an area of 10–20 mm^2 and a thickness of 0.5–1.5 mm. The surface of these reference samples was ground and polished, after which the mechanical stresses were relieved by annealing at 873 K.

The surface morphology of carbon deposits obtained in an argon atmosphere is illustrated by a SEM micrograph in Fig. 1a. The pattern is self-similar and scale-invariant, which is a characteristic feature of the fractal structure. The micrograph reveals rather large cloudlike formations with an average size of 10–20 μm. These are composed of smaller aggregates with an average size of 1–2 μm which, in turn, consist of globular carbon clusters 6–10 nm in size. The density of fractal deposits amounted to 59–61% of the graphite density, and the fractal dimension was D = 2.89. Figure 1b shows the surface of a nanotubular deposit. Here, one can see 2.5- to 5.5-μm aggregates including rounded fragments with dimensions from 100 to 350 nm, which are composed of multilayer nanotubes with a diameter of 12–15 nm. "Fluff" of such nanotubes is seen on the vertices of intermediate fragments.

The temperature dependence of the differential thermo emf S was measured relative to lead, which is known to possess a zero thermo emf. A cold junction was represented by the electric contact between the carbon sample surface (facing the cathode) and a massive lead plate the temperature of which was equal to that of the ambient medium. A hot junction was formed on the opposite sample surface by pressing a lead needle with a diameter of 0.1 mm to a fractal or nanotubular deposit under a load of 0.2–2 N. The lead needle was situated in a copper cylinder inside an electric heater, by which the needle temperature could be controlled in a range from 290 to 550 K. Mounted in the immediate vicinity of the needle–sample contact point was the junction of a chromel–alumel thermocouple made of 50-μm-thick wires. In this structure, the S value was measured at a temperature gradient of about 250 K/mm across the sample. The control measurements of thermo emf on sil-

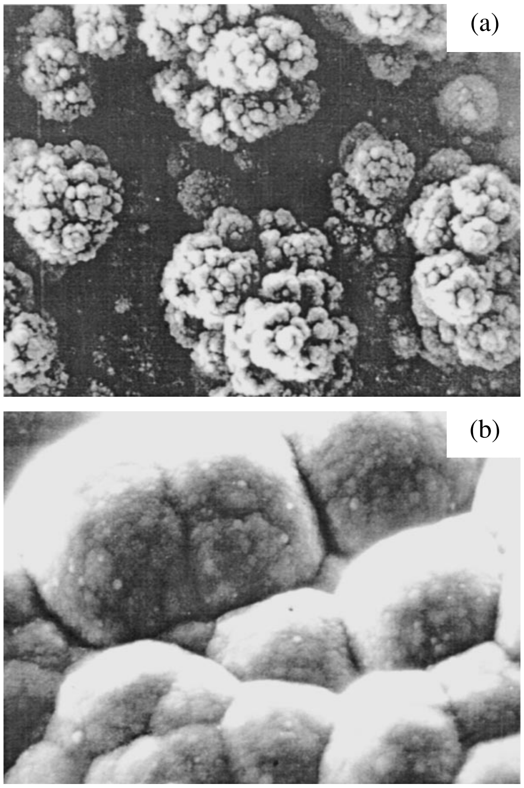

Fig. 1. SEM micrographs showing the surface morphology of (a) fractal (magnification, ×2600) and (b) nanotubular (×8400) carbon deposits.

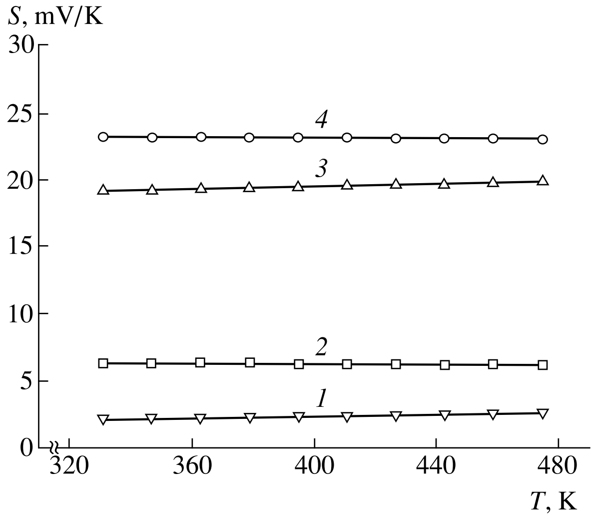

Fig. 2. The plots of thermo emf versus temperature for (*1*) polycrystalline graphite, (*2*) monocrystalline graphite, (*3*) fractal carbon deposit, and (*4*) nanotubular deposit.

ver plates (possessing a much higher thermal conductivity) gave S values close to the tabulated data. The relative error of S measurements did not exceed 2–3%.

Figure 2 presents the results of thermo emf measurements for the fractal (curve *3*) and nanotubular (curve *4*) carbon deposits, in comparison to the $S(T)$ curves for mono- and polycrystalline graphite samples. In the temperature range from 300 to 500 K, the thermo emf of the fractal and nanotubular carbon deposits is 8–9 times that of the polycrystalline graphite.

The magnitude and sign of thermo emf of a fine-grained graphite were recently studied by Matsuĭ *et al.* [1]. In the finely disperse material (grain size, 30 nm), the thermo emf was positive in the temperature range from 4.2 to 300 K, with the S values at 300 K not exceeding 10 μV/K. The values of $S \sim 20$ μV/K observed in our samples are by no means surprising, since the fractal deposits are composed of carbon particles with dimensions of 6–10 nm.

According to the concepts formulated in [2, 3], an increase in the thermo emf of a material is ensured by a "quantum-lattice" structure and by large active areas of interphase and intergrain boundaries. From this standpoint, both fractal and nanotubular carbon deposits conform to the notions of a "quantum-lattice" structure: the materials are composed of carbon particles with dimensions on the order of 6–10 nm or of multilayer carbon nanotubes 10–15 nm in diameter. Both materials are porous, with the density amounting to 60 and 77% of the density of compact graphite, respectively. Estimates of the specific internal surface area of the fractal and nanotubular deposits gave values of 270 and 120 m^2/g, respectively.

As is known (e.g., in semiconductors), the thermo emf also increases with the charge carrier mobility in the material [3]. The nanotubular deposits exhibit a nondissipative electron transport [4]. Therefore, the multilayer carbon nanotubes are characterized by a quantum conductivity, which is independent of the nanotube length and diameter even at room temperature. The fractal carbon deposit is also characterized by a sufficiently high conductivity (~10^4 S/m at 300 K [5]), which suggests the possibility of a ballistic charge transport in the bulk of the material.

Thus, converting graphite into a form possessing a nanotubular or fractal structure is accompanied by a significant increase in the thermo emf. These structural states can be used for the development of materials possessing improved thermoelectric characteristics.

REFERENCES

1. L. Yu. Matsuĭ, I. V. Ovsienko, and L. L. Vovchenko, Fiz. Nizk. Temp. **27** (1), 68 (2001) [Low Temp. Phys. **27**, 52 (2001)].
2. N. Cewen, Sci. Found. China **7** (1), 23 (1999).
3. M. Rontani and L. J. Sham, Appl. Phys. Lett. **77** (19), 3033 (2000).
4. V. I. Tsebro and O. E. Omel'yanovskiĭ, Usp. Fiz. Nauk **170** (8), 906 (2000).
5. I. V. Zolotukhin, Yu. V. Sokolov, and V. P. Ievlev, Fiz. Tverd. Tela (St. Petersburg) **40** (3), 584 (1998) [Phys. Solid State **40**, 539 (1998)].

Translated by P. Pozdeev

Technical Physics Letters, Vol. 28, No. 8, 2002, pp. 680–683. Translated from Pis’ma v Zhurnal Tekhnicheskoĭ Fiziki, Vol. 28, No. 16, 2002, pp. 37–44.
Original Russian Text Copyright © 2002 by Ponomarenko, Prokhorov.

Separation of the Informative Component from a Chaotic Signal of a Time-Delay System

V. I. Ponomarenko and M. D. Prokhorov

Saratov Branch, Institute of Radio Engineering and Electronics, Russian Academy of Sciences, Saratov, Russia
e-mail: sbire@sgu.ru

Received February 25, 2002

Abstract—A new method is proposed for determining the parameters of time-delay systems using the observable time series. With this method, it is possible to reveal communications in the case of data transmission based on the nonlinear mixing of the informative signal and a chaotic signal of the time-delay system. *© 2002 MAIK “Nauka/Interperiodica”.*

Introduction. In recent years, using chaotic signals for the hidden transmission of data has drawn considerable attention of researchers [1–7]. Various methods were suggested for secretly transmitting an informative signal employing chaotic dynamics, based on the principles of chaotic masking, switching of chaotic regimes, nonlinear mixing, frequency modulation by a chaotic signal, etc. However, it was found that some of these methods can, in fact, provide for only a limited confidence. For example, an informative communication transmitted by various methods using chaotic systems of low dimensionality can be revealed by an eavesdropper employing methods developed for dynamic system reconstruction from the observable time series [8] or by constructing sequence maps [9].

In the case of data transmission using chaotic systems of high dimensionality operating in a hyperchaos regime, the secret information can be recognized in some cases using a procedure of reconstruction of the transmitting system [10] by methods using spectrograms [11] and neural networks [12]. Recently [13], it was suggested to perform a secure data transmission using time-delay systems exhibiting chaotic motions of very high dimensionality. However, shortly after it was demonstrated [14] that, in cases of chaotic masking and modulation by a chaotic signal, the informative communication can still be revealed by the method of time-delay system reconstruction by the time series [15, 16].

Here we propose a new method for restoration of the parameters of a chaotic transmitting time-delay system from the observable time series. It will be demonstrated that informative communications can be revealed in cases of data transmission using a nonlinear mixing of the informative signal and chaotic signal.

Description of the data transmission channel. A communication system employing the nonlinear mixing of an informative signal to a chaotic signal was proposed by Volkovskiĭ and Rul’kov [3] and then developed by Dmitriev *et al.* [4]. In these methods, the chaotic signals were generated by a ring oscillator with 1.5 degrees of freedom [3] and by a ring scheme based on the Chua system [4]. We suggest using the chaotic carrier signals generated by a time-delay system characterized by a large number of positive Lyapunov exponents.

A schematic diagram of the communication system is presented in Fig. 1. In the absence of an informative signal ($m(t) = 0$), the transmitter can be described by a differential equation with delay. In the simplest case, this equation can be written as follows:

$$\varepsilon_0 \dot{x}(t) = -x(t) + f(x(t-\tau_0)), \qquad (1)$$

where $x(t)$ is the state of the system at the time instant t, f is a nonlinear function, τ_0 is the delay time, and ε_0 is a parameter characterizing the inertia of the system. The informative signal $m(t)$ is added to a chaotic signal $x(t)$ in the adder and the total signal $s(t) = x(t) + m(t)$ is fed into the communication channel and, simultaneously, into a feedback loop of the transmitting system. Oscillations of the transmitting system are

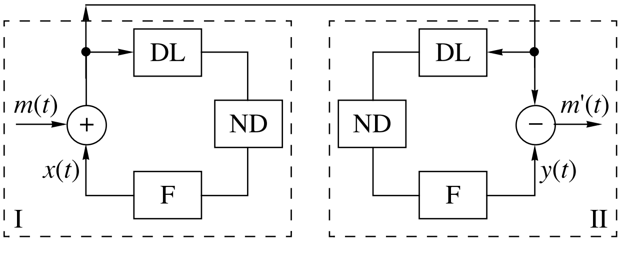

Fig. 1. Schematic diagram of a communication system: (I) transmitter; (II) receiver; (DL) delay line; (ND) nonlinear device; (F) filter.

described by the equation

$$\varepsilon_0\dot{x}(t) = -x(t) + f(x(t-\tau_0) + m(t-\tau_0)). \qquad (2)$$

The receiver is composed of the same elements as the transmitter, except for the adder being replaced by a subtracter breaking the feedback chain, and is described by the equation

$$\varepsilon_0\dot{y}(t) = -y(t) + f(x(t-\tau_0) + m(t-\tau_0)), \qquad (3)$$

where $y(t)$ is the signal entering the subtracter. The subtracter output yields the reconstructed informative signal $m'(t) = x(t) + m(t) - y(t)$.

Once the elements of the receiving and transmitting systems are identical, the two systems will be synchronized after a certain transient process. Indeed, the difference $\Delta(t) = x(t) - y(t)$ between the oscillations described by Eqs. (2) and (3) decreases for any $\varepsilon_0 > 0$ because $\dot{\Delta}(t) = -\Delta/\varepsilon_0$. As a result of this synchronization, $x(t) = y(t)$ and $m'(t) = m(t)$. Note that the quality of reconstruction of the signal $m(t)$ depends on neither amplitude nor frequency characteristics. This implies that complicated informative signals can be transmitted without distortions.

Reconstruction of the time-delay system parameters from the observable time series. Security of chaotic communication systems is based on the fact that parameters of the transmitting system are known only to the receiving party, which possesses an exact copy of the transmitter. Using the data transmission system described above, we will demonstrate that an informative communication can be revealed by an eavesdropper having access only to a time series of the transmitted signal $s(t)$. To this end, we have to reconstruct parameters of the time-delay system of type (1) generating the masking chaotic signal.

In order to restore the delay time τ_0 from the observable time series, we will use a method proposed in our recent papers [17, 18], where it was shown that time series of the systems of type (1) possess virtually no extrema spaced from each other by τ_0. Then, in order to find τ_0, we have to determine the numbers N of the pairs of extrema spaced by various times τ in the known time series. Upon plotting the $N(\tau)$ dependence, we determine the τ_0 value as the position of the absolute minimum of the $N(\tau)$ function. The presence of an informative component of small amplitude does not qualitatively change the shape of $N(\tau)$. As was demonstrated in [17, 18], this method of determining τ_0 works even at a noise level on the order of 10%.

In order to determine the parameter of inertia ε_0 and the nonlinear function f of system (1) from the chaotic time series, we propose a new method, which will be first demonstrated in the absence of an informative system. According to Eq. (1), a set of points with the coordinates $[x(t-\tau_0), \varepsilon_0\dot{x}(t) + x(t)]$ plotted on the plane would reproduce the function f. Since the quantity ε_0 is not known a priori, we have to plot $\varepsilon\dot{x}(t) + x(t)$ versus $x(t-\tau_0)$ for various ε values until the obtaining of a single-valued correspondence on the $[x(t-\tau_0), \varepsilon\dot{x}(t) + x(t)]$ plane, which is only possible for $\varepsilon = \varepsilon_0$. A quantitative criterion for this single-valued correspondence in the search for ε_0 can be represented by the condition of minimum length $L(\varepsilon)$ connecting the points $[x(t-\tau_0), \varepsilon\dot{x}(t) + x(t)]$ ordered with respect to the coordinate $x(t-\tau_0)$. A minimum in $L(\varepsilon)$ will correspond to $\varepsilon = \varepsilon_0$, while the set of points corresponding to this ε on the $[x(t-\tau_0), \varepsilon_0\dot{x}(t) + x(t)]$ plane will reproduce the nonlinear function.

In contrast to other methods [15, 16] using only extremal points or the points selected by a certain rule for reconstruction of the nonlinear functions, the proposed approach employs all points of the time series. This circumstance allows the nonlinear function to be more completely reconstructed using short time series even for a weakly developed chaos. Note that the mixing of an informative component of small amplitude to the chaotic signal will insignificantly influence the accuracy of determining ε_0.

In order to estimate performance of the method in the presence of perturbations, let us apply the procedure outlined above to a process obtained by adding a Gaussian white noise with zero mean to a time series determined by the Mackey–Glass equation,

$$\dot{x}(t) = -bx(t) + \frac{ax(t-\tau_0)}{1 + x^c(t-\tau_0)}. \qquad (4)$$

Equation (4) can be converted to the form (1) by introducing $\varepsilon_0 = 1/b$ and the function $f[x(t-\tau_0)] = ax(t-\tau_0)/b(1 + x^c(t-\tau_0))$. Using the $L(\varepsilon)$ function, it is possible to restore the ε_0 value at a noise level on the order of 3%.

Reconstruction of the receiving system parameters. Once the transmitting system parameters are restored, we can reconstruct the receiving system as well. In order to demonstrate possibilities of the proposed method, let us first consider a numerical example representing a chaotic signal generated by the Mackey–Glass system (4) to which a frequency-modulated (FM) harmonic signal (communication) $m(t) = A\sin[2\pi f_c t - B\cos(2\pi f_m t)]$ is admixed. In the FM signal, A determines amplitude of the informative signal, f_c is the central frequency of the signal spectrum, B is the FM index, and f_m is the modulation frequency.

Figures 2a and 2b show fragments of the time series and the power spectra of the FM signal and the total transmitted chaotic signal $s(t) = x(t) + m(t)$. Figure 2c shows a plot of the number N of the pairs of extrema in the $s(t)$ time series which are spaced by τ from each other. The $N(\tau)$ curve was constructed using 20000 points of the

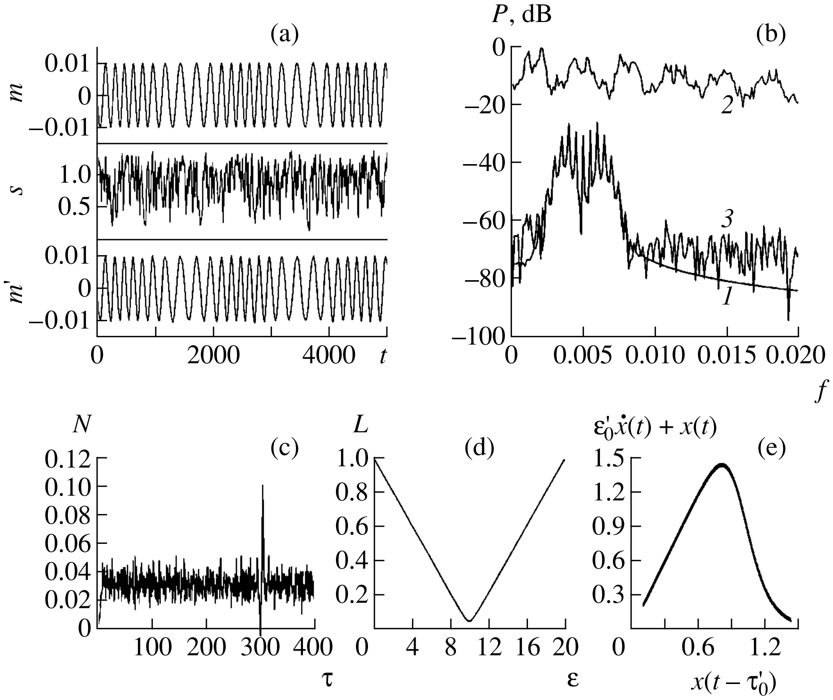

Fig. 2. (a) Fragments of the time series of a frequency-modulated harmonic signal $m(t) = A\sin[2\pi f_c t - B\cos(2\pi f_m t)]$ with $A = 0.01$, $B = 3$, $f_c = 5 \times 10^{-3}$, and $f_m = 5 \times 10^{-4}$; a total signal $s(t)$ transmitted via the channel with $a = 0.2$, $b = 0.1$, $c = 10$, and $\tau_0 = 300$; and the revealed signal $m'(t)$; (b) power spectra of the signals (*1*) $m(t)$, (*2*) $s(t)$, and (*3*) $m'(t)$; (c) plot of $N(\tau)$ with $N_{\min}(t) = N(300.0)$; (d) plot of $L(\varepsilon)$ with $L_{\min}(\varepsilon) = L(10.0)$ is normalized so that the most disordered set of points is characterized by $L = 1$; (e) reconstructed nonlinear function.

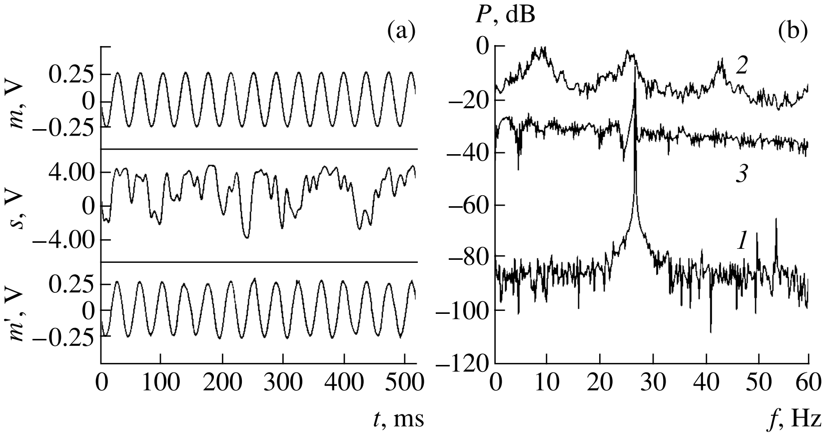

Fig. 3. (a) Fragments of the time series of a harmonic signal $m(t) = A\sin(2\pi f_c t)$ with $A = 0.25$ V and $f_c = 27$ Hz, a total signal $s(t)$ transmitted via the channel, and the revealed harmonic signal $m'(t)$; (b) power spectra of the signals (*1*) $m(t)$, (*2*) $s(t)$, and (*3*) $m'(t)$.

$s(t)$ time series containing about 600 extrema (the $N(\tau)$ function is normalized to the total number of extrema). The derivative $\dot{x}(t)$ was estimated from the observable time series using a local parabolic approximation. Using the absolute minimum of $N(\tau)$, we estimate the delay time at $\tau'_0 = 300.0$.

The $L(\varepsilon)$ plot (Fig. 2d) was constructed using only 2000 points of the $s(t)$ time series. The value of the parameter of inertia determined as the position of minimum of the $L(\varepsilon)$ curve is $\varepsilon'_0 = 10.0$ ($\varepsilon_0 = 1/b = 10$). A nonlinear function reconstructed for the above τ'_0 and ε'_0 values is depicted in Fig. 2e. This function was approximated by polynomials of various powers. The approximating functions ensured good quality of the synchronous response of the receiver for polynomials with a power of not less than 12. Figures 2a and 2b show a fragment of the time series of the informative

FM signal, revealed by the proposed method, and the corresponding power spectrum.

Another example is offered by an experimental data transmission system in which a chaotic signal source is represented by a time-delay feedback oscillator. In the case when the filter F (see Fig. 1) is represented by a low-frequency RC filter of the first order, the oscillator is described by the equation $RC\dot{V}(t) = -V(t) + f[V(t-\tau_0)]$, where $V(t)$ and $V(t-\tau_0)$ are the delay line (DL) input and output voltages, respectively; R and C are the resistance and capacitance of the filter elements, respectively; and f is the transmission function of the nonlinear device (ND). This equation is of type (1) with $\varepsilon_0 = RC$.

In our experiment, the nonlinear device possessed a quadratic transmission function. An informative signal admixed to the chaotic signal $V(t)$ represented a harmonic function $m(t) = A\sin(2\pi f_c t)$ with amplitude A and frequency f_c. The total transmitted signal was $s(t) = VB(t) + m(t)$. The signals $m(t)$ and $s(t)$ were recorded at a sampling frequency of $f_s = 4$ kHz. Figure 3 shows the fragments of time series and the corresponding power spectra of these signals together with the harmonic signal $m'(t)$ revealed using the proposed method.

Conclusion. We proposed a new method for reconstructing time-delay systems from the observable time series and demonstrated the possibility of revealing communications in systems of secure data transmission using chaotic signals of time-delay systems. Thus, communication systems employing signals of time-delay systems can be insufficiently secure despite a high dimensionality and a large number of positive Lyapunov exponents of the chaotic attractors of these systems.

Acknowledgments. The authors are grateful to B.P. Bezruchko for fruitful discussions.

This study was supported by the Russian Foundation for Basic Research (project no. 02-02-17578) and by the US Civilian Research and Development Foundation for the Independent States of the Former Soviet Union (CRDF Award no. REC-006).

REFERENCES

1. L. Kocarev, K. S. Halle, K. Eckert, *et al.*, Int. J. Bifurcation Chaos Appl. Sci. Eng. **2** (3), 709 (1992).
2. K. M. Cuomo and A. V. Oppenheim, Phys. Rev. Lett. **71** (1), 65 (1993).
3. A. R. Volkovskiĭ and N. F. Rul’kov, Pis’ma Zh. Tekh. Fiz. **19** (3), 71 (1993) [Tech. Phys. Lett. **19**, 97 (1993)].
4. A. S. Dmitriev, A. I. Panas, and S. O. Starkov, Int. J. Bifurcation Chaos Appl. Sci. Eng. **5** (4), 1249 (1995).
5. A. S. Dmitriev, A. I. Panas, and S. O. Starkov, Usp. Sovrem. Radioélektron., No. 10, 4 (1997).
6. A. S. Dmitriev and L. V. Kuz’min, Pis’ma Zh. Tekh. Fiz. **25** (16), 71 (1999) [Tech. Phys. Lett. **25**, 665 (1999)].
7. É. V. Kal’yanov, Pis’ma Zh. Tekh. Fiz. **27** (16), 1 (2001) [Tech. Phys. Lett. **27**, 665 (2001)].
8. K. M. Short, Int. J. Bifurcation Chaos Appl. Sci. Eng. **6** (2), 367 (1996).
9. G. Pérez and H. A. Cerdeira, Phys. Rev. Lett. **74** (11), 1970 (1995).
10. K. M. Short and A. T. Parker, Phys. Rev. E **58** (1), 1159 (1998).
11. T. Yang, L.-B. Yang, and C.-M. Yang, Phys. Lett. A **247** (1–2), 105 (1998).
12. T. Yang, L.-B. Yang, and C.-M. Yang, Physica D (Amsterdam) **124** (1–3), 248 (1998).
13. B. Mensour and A. Longtin, Phys. Lett. A **244** (1–3), 59 (1998).
14. C. Zhou and C.-H. Lai, Phys. Rev. E **60** (1), 320 (1999).
15. M. J. Bünner, M. Popp, Th. Meyer, *et al.*, Phys. Lett. A **211**, 345 (1996).
16. M. J. Bünner, M. Popp, Th. Meyer, *et al.*, Phys. Rev. E **54** (4), 3082 (1996).
17. A. S. Karavaev, V. I. Ponomarenko, and M. D. Prokhorov, Pis’ma Zh. Tekh. Fiz. **27** (10), 43 (2001) [Tech. Phys. Lett. **27**, 414 (2001)].
18. B. P. Bezruchko, A. S. Karavaev, V. I. Ponomarenko, and M. D. Prokhorov, Phys. Rev. E **64** (5), 056216 (2001).

Translated by P. Pozdeev

Technical Physics Letters, Vol. 28, No. 8, 2002, pp. 684–686. Translated from Pis'ma v Zhurnal Tekhnicheskoĭ Fiziki, Vol. 28, No. 16, 2002, pp. 45–51.
Original Russian Text Copyright © 2002 by Shalygina, Abrosimova.

Micromagnetic Structure and Local Magnetic Properties of Permalloy Microstripes

E. E. Shalygina and N. M. Abrosimova
Moscow State University, Moscow, 119899 Russia
e-mail: shal@magn.phys.msu.su

Received January 10, 2002; in final form, March 18, 2002

Abstract—The micromagnetic structure and local magnetic properties of permalloy microstripes with an aspect ratio varying from 2 to 15 are studied by scanning Kerr microscopy. The local magnetic properties of the microstripes strongly depend on their dimensions and on the position of a local site probed. It is established that the local magnetic properties and the magnetization distribution in the samples are determined by inhomogeneous magnetic dipole fields. *© 2002 MAIK "Nauka/Interperiodica".*

In recent years, considerable attention of researchers is devoted to the investigation of local magnetic properties and remagnetization behavior of two- and one-dimensional magnetic materials in which one or two system dimensions fall within a micrometer or nanometer range. Among these low-dimensional magnetic materials (LDMMs), most interesting are those composed of magnetic micro- or nanowires; particular examples are offered by ultrathin microstripes and magnetic dots. The main methods of obtaining LDMMs are high-resolution electron beam lithography and electrochemical or chemical deposition of magnetic 3*d* metals onto porous semiconductor substrates.

Investigation of the micromagnetic structure (equilibrium magnetization distribution) of the LDMMs, the relationship between their dimensions and local magnetic properties, and the influence of low-dimensional magnetic elements on the remagnetization processes in these materials are currently important problems for the physics of magnetic phenomena. At the same time, monitoring the magnetic behavior of LDMMs is important for practical applications, since LDMMs are widely used in miniature devices of modern microelectronics. The micromagnetic structure and magnetic properties of LDMMs can be studied by a variety of experimental techniques (including atomic and magnetic force microscopy, SQUID magnetometers, etc.) [1–9]. However, the most rapid and fullest characterization of LDMMs is provided by the scanning Kerr microscopy techniques.

The aim of this work was to study the micromagnetic structure and local magnetic properties of permalloy microstripes with the ratio of length l to width w (aspect ratio) varying from 2 to 15 by the scanning Kerr microscopy method. Within the framework of this study, we paid considerable attention to the analysis of magnetostatic interaction between microstripes.

The samples, comprising sets of periodically arranged microstripes, were prepared from $Ni_{80}Fe_{20}$ permalloy films by high-resolution electron beam lithography. The initial $Ni_{80}Fe_{20}$ permalloy films were obtained by dc magnetron sputtering at a residual pressure in a working chamber of 10^{-8} Torr and an Ar pressure of 1×10^{-4} Torr. These films exhibited a uniaxial magnetic anisotropy with an easy magnetization axis in the film plane. The saturation field H_s and the coercive field H_c for the magnetization reversal along the easy axis were 8.2 and 1.2 Oe, respectively.

Each sample contained a total of $\sim 1 \times 10^6$ microstripes. The microstripes were oriented with their long sides in the direction of the easy axis of the initial films. The stripe width was $w = 2$ μm. In the series of samples studied, the l/w ratio varied from 2 to 15, while the spacing S_1 of microstripes in each row varied from 0.25 to 4 μm; the distance between rows was $S_2 = 2$ μm. The microstripes possessed distinct 90° side faces. We also prepared samples containing single microstripes with the dimensions indicated above.

The micromagnetic structure and local magnetic properties of the permalloy microstripes described above were studied with the aid of a magnetooptical micromagnetometer. The experimental setup was constructed on the basis of a polarization microscope ensuring a magnification of up to 1200× and a linear resolution of up to 0.2 μm. The size of a microscopic near-surface region of the sample probed by the micromagnetometer was determined by the width of a slit mounted in the microscope image plane in front of the optical detector. By scanning the microstripe image along the length l with the 0.5×2 mm slit, we measured the local hysteresis loops and the distribution of the in-plane magnetization components using the equatorial Kerr effect.

Distributions of the magnetization component M_n perpendicular to the microstripe surface were measured using the polar Kerr effect. The sensitivity of measurements was increased by using a modulation technique for the detection of magnetooptical signals. Therefore, the samples were subjected to remagnetization in an alternating magnetic field **H** at a frequency of $f = 80$ Hz. The field **H** was applied in the sample plane in the direction parallel to the microstripe length. Under these conditions, we actually measured the ratios $\delta(l, H)/\delta_s \sim M(l, H)/M_s$, where $\delta = (I - I_0)/I_0$; I and I_0 are the intensities of light reflected from magnetized and nonmagnetized samples, respectively; and δ_s denotes the value of δ at $M = M_s$, where M_s is the saturation magnetization. These measurements were performed in the central regions of the samples.

Figure 1 shows the local hysteresis loops measured in the central and terminal regions of microstripes of various length. As can be seen, the local magnetic characteristics of the microstripes depend both on their dimensions and on the local site position. In particular, the local values of H_s increase with decreasing microstripe length l and with increasing distance from the microstripe center. It was found that the local saturation fields of the samples composed of microstripes are greater than the H_s values of continuous films, but smaller than the H_s of single microstripes. We calculated the local H_s values using an analytical expression for the local demagnetization factor of the central region of a rectangular element (Fig. 2a) [10]. It was found that, for $l/w < 7$, the calculated and measured H_s values virtually coincide, while for $l/w > 7$, the experimental values are considerably greater than the calculated ones.

The latter discrepancy can be explained as follows. The measured magnetization distributions showed that the microstripes with $l/w > 7$ contain in-plane magnetization components both parallel ($M_\parallel$) and perpendicular ($M_\perp$) to the applied magnetic field. The function $M_\perp(l)$ changes sign, while the $M_\perp$ value is nonzero up to high magnetic field strengths, where the $M_\parallel$ component almost ceases to change, reaching a level of $(0.97–0.98)M_s$. These data suggest that microstripes with $l/w > 7$ exhibit a buckling remagnetization mode. The existence of $M_\perp$ gives rise to stray fields perpendicular to applied magnetic field **H**, which accounts for blocking of the remagnetization process and leads to an increase in H_s.

The shape of the local hysteresis loops (Fig. 1)—in particular, an almost linear dependence of the magnetization on the magnetic field strength—is evidence that the remagnetization of microstripes takes place primarily via rotation of the local magnetization vectors.

Let us consider in more detail the results of investigation of the micromagnetic structure (equilibrium magnetization distribution) in the microstripes. Figure 3a shows distributions of the in-plane magnetization com-

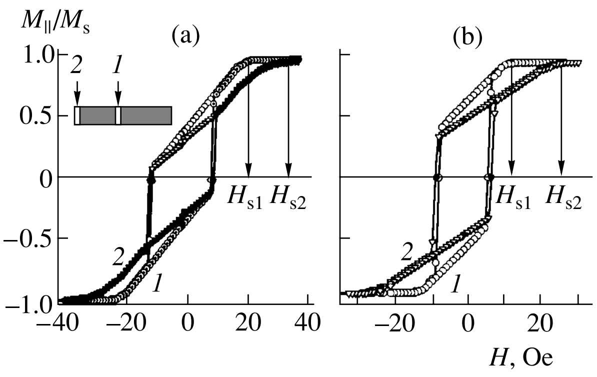

Fig. 1. Local hysteresis loops measured in (*1*) central and (*2*) terminal regions of permalloy microstripes with dimensions (a) 2 × 4 × 0.015 μm and (b) 2 × 6 × 0.015 μm. The measurements were performed using the equatorial Kerr effect with a low-frequency magnetic field oriented along the microstripe length *l*. The spacing of microstripes in both samples was $S_1 = 0.5$ μm. The inset in the left panel indicates the sites of measurements on a microstripe.

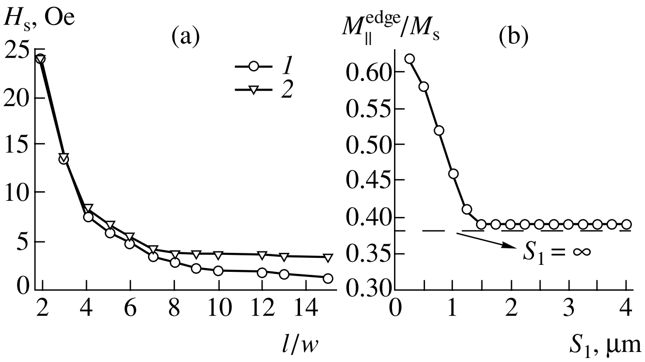

Fig. 2. (a) Dependence of the calculated (*1*) and experimental (*2*) local saturation fields H_s in the central region of a microstripe on the aspect ratio *l/w*; (b) plot of the planar magnetization component in the edge part of a microstripe versus spacing S_1 for the samples of microstripes with dimensions 2 × 6 × 0.015 μm. Dashed line indicates the magnetization of the edge part of an isolated microstripe.

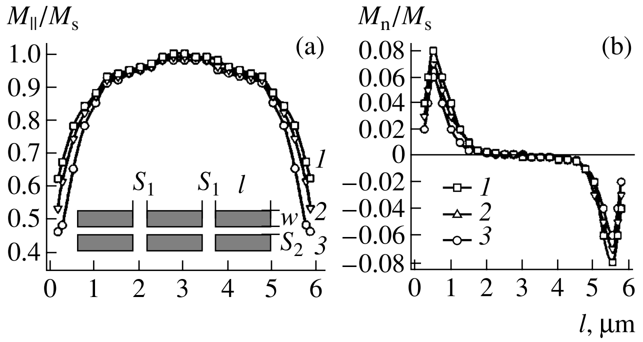

Fig. 3. The distributions of (a) planar $M_\parallel$ and (b) normal M_n magnetization components along a microstripe measured using the equatorial and polar Kerr effects, respectively, on the samples containing microstripes with dimensions 2 × 6 × 0.015 μm spaced by $S_1 = 0.25$ (*1*), 0.5 (*2*), and 1.0 μm (*3*). The low-frequency magnetic field $H = 13$ Oe was oriented along the microstripe length *l*. The inset in the left panel shows the arrangement of microstripes in a sample.

ponents parallel to the magnetic field applied along the microstripe length. The curves refer to samples of microstripes with the same dimensions, but with different spacings S_1. Measurements of the polar Kerr effect showed that, besides the in-plane magnetization components, there exist components M_n perpendicular to the microstripe surface. The polar Kerr effect was measured using a magnetic field **H** parallel to l and light normally incident onto the sample. Figure 3b shows the plots of $M_\text{n}(l)$ measured for the same samples. As can be seen from Fig. 3, the normal magnetization component exists in the planar field only in the terminal parts of the microstripes. The appearance of M_n can be explained by the presence of stray fields in these regions. It is also seen that the local magnetization components (both M_n and $M_\|$) in the terminal parts of microstripes increase with decreasing S_1, while the local values of M_n and $M_\|$ in the central regions vary insignificantly. Moreover, it was found that the $M_\|(l)$ and $M_\text{n}(l)$ curves exhibit asymmetric shapes, provided that the S_1 values of the nearest neighbor microstripe are different.

Figure 2b presents a plot of the planar magnetization component of the edge part of a microstripe $M_\|^\text{edge}$ versus S_1, where $M_\|^\text{edge}$ is the local planar magnetization averaged over a terminal region of 0.25×2 μm. As can be seen from these data, the $M_\|^\text{edge}$ value increases with decreasing S_1 in the region of $S_1 < 1.25$ μm and asymptotically tends to the value of $M_\|^\text{edge}$ for $S_1 = \infty$ (isolated stripe) in the region of $S_1 > 1.25$ μm. This behavior is explained as follows. According to micromagnetic calculations [11], a local demagnetization factor for the probed region of a microstripe (belonging to a set of $\sim 10^6$ magnetic microstripes) depends both on the position of this region in the given microstripe and on the spacing of microstripes in the sample. This is related by inhomogeneous magnetic dipole fields arising during the magnetization of samples. These fields rapidly decay (as $\sim 1/r^2$) with distance from the edge (on approaching the central part), which is accompanied by a decrease in the local demagnetization factor. As a result, the local magnetization of the central regions changes rather slightly, while the terminal regions are subject to a strong influence of inhomogeneous dipole magnetic fields. As the microstripe spacing S_1 decreases, this effect becomes more pronounced due to increasing interaction between the microstripes.

In conclusion, magnetooptical investigation of the samples comprising sets ($\sim 10^6$) of permalloy microstripes with micron dimensions showed that the local magnetic properties of these microstripes strongly depend on their dimensions, the position of a local site probed, and the mutual arrangement (spacing) of microstripes. It has been shown that behavior of the samples studied is determined primarily by the inhomogeneous magnetic dipole fields. It has been experimentally established that a strong magnetostatic interaction between microstripes in the samples is manifested beginning with a spacing of $S_1 < 1.25$ μm.

Acknowledgments. This study was supported by the Russian Foundation for Basic Research, project no. 02-02-16627.

REFERENCES

1. J. F. Smyth, S. Schultz, D. R. Fredkin, *et al.*, J. Appl. Phys. **69**, 5262 (1991).
2. A. Maeda, M. Kume, T. Ogura, *et al.*, J. Appl. Phys. **76**, 6667 (1994).
3. K. J. Kirk, J. N. Chapman, and C. D. Wilkinson, Appl. Phys. Lett. **71**, 539 (1997).
4. A. Ercole, A. O. Adeyeye, C. Daboo, *et al.*, J. Appl. Phys. **81**, 5452 (1997).
5. A. Stankiewicz, W. K. Hiebert, G. E. Ballentine, *et al.*, IEEE Trans. Magn. **34**, 1003 (1998).
6. J. Shi, T. Zhu, M. Durlam, *et al.*, IEEE Trans. Magn. **34**, 997 (1998).
7. R. D. Gomez, T. V. Luu, A. O. Pak, *et al.*, J. Appl. Phys. **85**, 6163 (1999).
8. F. Marty, A. Vaterlaus, V. Weich, *et al.*, J. Appl. Phys. **85**, 6166 (1999).
9. T. Schrefl, J. Magn. Magn. Mater. **207**, 66 (1999).
10. J. A. Copeland, J. Appl. Phys. **35**, 1905 (1972).
11. P. K. George and A. J. Hughes, IEEE Trans. Magn. **12**, 137 (1976).

Translated by P. Pozdeev

Technical Physics Letters, Vol. 28, No. 8, 2002, pp. 687–689. Translated from Pis'ma v Zhurnal Tekhnicheskoĭ Fiziki, Vol. 28, No. 16, 2002, pp. 52–57.
Original Russian Text Copyright © 2002 by Bazhenova, Bormotova, Golub, Kotel'nikov, Makeich, Shcherbak.

The Formation of Vortex Shocks in a 3D Subsonic Flow Behind a Weak Shock Wave Emerging from a Channel

**T. V. Bazhenova, T. A. Bormotova, V. V. Golub, A. L. Kotel'nikov,
A. A. Makeich, and S. B. Shcherbak**

*Institute for High Energy Densities, Associated Institute for High Temperatures, Russian Academy of Sciences,
Moscow, Russia*

e-mail: bazhenova@ihed.ras.ru

Received March 21, 2002

Abstract—The structure of a 3D subsonic flow behind a diffracted shock wave was studied by experimental and numerical methods for the incident shock wave Mach numbers M_0 close to unity. It is established that vortex shocks appear in the flow behind the diffracted shock wave even when M_0 decreases to 1.04, which is much lower than the threshold Mach number obtained analytically for a 2D automodel case. The time interval from the outflow start to the local supersonic zone formation, as well as the experimentally measured time of appearance of the first vortex shock, increase with decreasing M_0. *© 2002 MAIK "Nauka/Interperiodica".*

When a shock wave expands on emerging from a channel into space, the boundary of the outflowing gas (on which the flow velocity exhibits discontinuity) forms a large-scale vortex. The formation of a secondary shock wave in this large-scale vortex was revealed by numerical analysis of a weak shock wave diffracted on a dihedral angle in unbounded space for the incident shock wave Mach numbers $M_0 \geq 1.45$ [1] and experimentally observed in a shock wave emerging from a rectangular channel and diffracted on a flat dihedral angle for $M_0 \geq 1.33$ [2, 3]. These results suggest that local supersonic zones appear in a subsonic cocurrent flow. The formation of vortex shocks as a result of the supersonic jet drag leads to an increase in the entropy and favors dissipation of the mechanical energy in the flow behind the diffracted shock wave.

The observed phenomena can be explained by the following factors: (i) the formation of a shock wave in the vortex due to coherent structures appearing as a result of the Kelvin–Helmholtz instability development at the interface between two media; (ii) the flow acceleration under the action of three-dimensional (3D) rarefaction waves entering into the channel; and (iii) the formation of a quasi-nozzle in the flow by a separation line coiling into a vortex.

Sun and Takayama [2] attempted to theoretically predict the value of M_0 for which a secondary shock wave will appear in a semibounded space (automodel case). It was assumed that the shock wave formation at the vortex core is caused by a supersonic flow created by rarefaction waves at the dihedral angle. It was found that a minimum incident shock wave Mach number for which the secondary supersonic flow can arise is 1.346. This threshold value was consistent with the results of experiments performed with a flat dihedral angle [3] and with a weak shock wave emerging from a channel with rectangular cross section [2]. However, it should be noted that the appearance of weak shocks is difficult to detect by the interferometric techniques employed in [2, 3].

Table 1. Experimental dependence of the vortex shock formation time t on the incident shock wave Mach number M_0

M_0	t, μs	M_0	t, μs
1.1	595	1.31	352
1.15	498	1.32	304
1.23	425	1.34	288
1.24	389	1.35	278
1.25	401	1.37	292
1.25	389	1.37	270
1.27	352	1.38	231
1.3	352	1.45	183

Table 2. Time of the vortex shock formation numerically calculated for various Mach numbers of the incident shock wave

M_0	t, μs	$\bar{t}$
1.40	43	0.30
1.35	65	0.45
1.30	143	0.99
1.27	215	1.49
1.25	288	2.00

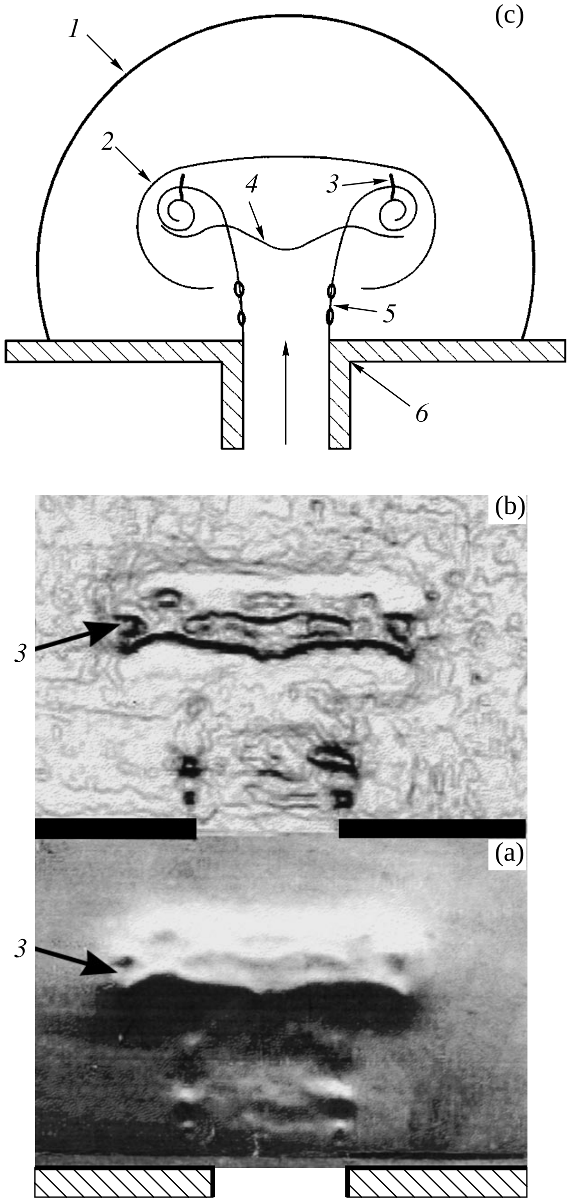

Fig. 1. The flow pattern behind a diffracted shock wave ($M_0 = 1.04$; $t = 1200$ μs; $\bar{t} = 8.3$) illustrated by (a) a schlieren photograph, (b) the image processed by Adobe Photoshop, and (c) schematic diagram of the flow structure: (*1*) diffracted shock wave (outside the imaged area); (*2*) an interface between the gas driven by the diffracted shock wave and the gas emerging from the channel; (*3*) vortex shock; (*4*) vortex loop; (*5*) the Kelvin–Helmholtz instability at the separation line; (*6*) shock wave tube output edge.

As is known, the channel output geometry influences the intensity of a diffracted wave and the structure of a flow behind this wave. For a shock tube with a square cross section, the diffracted shock wave acquires a complicated 3D shape [4] varying in time and space. It was pointed out that the emerging flow structure behind a strong diffracted shock wave in the 3D case is different from the patterns observed in the axisymmetric and flat cases [5].

Here we report the results of experimental and numerical investigation of the formation of local supersonic zones and vortex shocks in a 3D case, in the flow behind a weak shock wave emerging from the channel with a square cross section.

The experiments were performed in a setup comprising a shock tube connected to a vacuum chamber. The working gas was air. The shadow pattern of the flow structure evolution behind the shock wave was monitored by a modified high-speed camera of the VSK-5 type, which allowed up to 72 images sized 16 × 22 mm to be obtained in each experiment at a time interval of 4–7 μs. In order to analyze some details of the process, we obtained separate 24 × 36 mm images with the aid of a spark light source. A typical schlieren photograph of the flow pattern formed upon diffraction of a shock wave emerging from a square channel is shown in Fig. 1. The shot was made at a time instant corresponding to $t = 1200$ μs after the wave escaped from the channel output. In addition, Fig. 1 presents the results of computer processing of the image and a schematic diagram of the flow structure. As can be seen, there are sharp changes in intensity at the corners of the vortex ring. In order to check that the observed optical inhomogeneity corresponds to a shock wave, we conducted experiments with the Foucault knife in the reverse position. The vortex shock formation in separate shots was observed even upon decreasing the incident shock wave Mach number down to $M_0 = 1.04$.

The monitoring of evolution of the flow structure behind the shock wave allowed us to trace dependence of the time of the vortex shock formation on the Mach number of the incident shock wave (Table 1). The relative time interval $\bar{t}$ (in dimensionless units) from the outflow start to the vortex shock's appearance linearly decreases by the law $\bar{t} = 13\text{–}8.2M_0$ when the incident shock wave Mach number M_0 increases.

The results of numerical calculations of a 3D field of the flow parameters behind the diffracted shock wave showed that, by a certain time instant t after the outflow start, zones with a Mach number above unity appear near the vortex (Table 2). The dimensionless time is obtained by normalization to $d/\sqrt{P_0/\rho_0}$, where d is the channel cross section side length and P_0 and ρ_0 are the initial pressure and gas density in the working chamber, respectively. Under the experimental conditions studied, the dimensionless time unit corresponds to 144 μs.

According to the results of calculations, the formation of a supersonic flow zone takes place at a lower value of the incident shock wave Mach number M_0 as compared to that at which the vortex shock is experimentally observed (Table 1). The difference can be related to the fact that the vortex shock formation requires additional time. This time increases with decreasing M_0, which explains why the vortex shocks

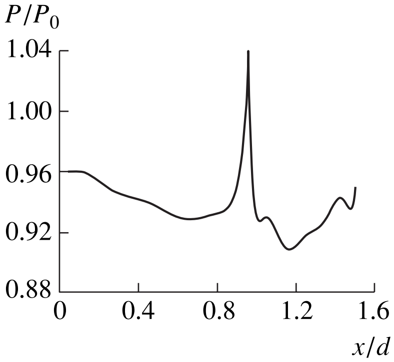

Fig. 2. A flow pressure profile along the square diagonal in the cross section spaced by 0.5*d* from the channel output at a time instant $\bar{t}$ = 2.15 (t = 310 μs). Numerical calculation for M_0 = 1.25.

were not observed in [2, 3]. The pressure jump in the vicinity of the vortex is illustrated in Fig. 2.

Thus, the experiments and numerical calculations showed that vortex shocks appear in a 3D subsonic flow behind a diffracted shock wave at the incident wave Mach numbers M_0 below a threshold determined analytically for a 2D automodel case.

Acknowledgments. This study was supported by the Russian Foundation for Basic Research, project no. 01-01-00664.

REFERENCES

1. R. Hillier, Shock Waves **4**, 17 (1995).
2. M. Sun and K. Takayama, Shock Waves **7**, 287 (1997).
3. H. Kleine, E. Rizerfeld, and H. Gronig, in *Proceedings of the 19th International Symposium on Shock Waves, Marseille, 1993*, Ed. by R. Brun and L. Z. Dumitrescu (Springer-Verlag, Berlin, 1995), Vol. 4, p. 117.
4. T. V. Bazhenova, O. A. Bulat, V. V. Golub, *et al.*, Izv. Akad. Nauk, Mekh. Zhidk. Gaza, No. 1, 200 (1993).
5. T. V. Bazhenova, V. V. Golub, T. A. Bormotova, *et al.*, Teplofiz. Vys. Temp. **39** (1), 123 (2001).

Translated by P. Pozdeev

Technical Physics Letters, Vol. 28, No. 8, 2002, pp. 690–692. Translated from Pis'ma v Zhurnal Tekhnicheskoĭ Fiziki, Vol. 28, No. 16, 2002, pp. 58–64.
Original Russian Text Copyright © 2002 by Fedosov, Galanzha, Solov'eva, Tuchin.

Laser Monitoring of the Flow Velocity in Lymphatic Microvessels Based on a Spatiotemporal Correlation of the Dynamic Speckle Fields

I. V. Fedosov, E. I. Galanzha, A. V. Solov'eva, and V. V. Tuchin
Saratov State University, Saratov, Russia
e-mail: fedosoviv@info.sgu.ru

Received March 19, 2002

Abstract—A method and the corresponding experimental setup for the *in vivo* laser monitoring of temporal variations in the velocity and direction of flow in lymphatic microvessels are described. Experimental results on the laser monitoring of flow in the mesenteric microvessels of rat are presented. The method is based on an analysis of the statistical properties of the dynamic speckle fields and provides for a high spatial resolution. The results of determination of the lymph flow velocity by the proposed method agree well with analogous data of functional transmission microscopy. *© 2002 MAIK "Nauka/Interperiodica".*

Introduction. The lymphatic vascular system plays an important role in maintaining tissue homeostasis in an organism. Investigation of the alternating local lymph flow in microvessels is of considerable interest from the standpoint of physiology, since the lymphatic drainage of organs and tissues is the factor ensuring their normal functioning due to permanent removal of excess fluids, proteins, and cells from the interstitial space and return to the blood flow [1–5].

At present, there are two basic methods for measuring the flow velocity with an allowance for the flow direction, which can be, in principle, used for the *in vivo* monitoring of lymph motion in microvessels of the lymphatic system. The first method is offered by functional biomicroscopy techniques involving video record of the vessel studied, followed by a shot-by-shot analysis of the video images [5, 6]. However, this approach is applicable for relatively low cell concentrations in the flow and involves a time-consuming stage of image processing. The second method, called laser Doppler anemometry, is based on using the optical heterodyne effect for determining the Doppler frequency shift of laser radiation scattered from moving particles [7]. The main disadvantage of this method is the need for using complicated and expensive devices ensuring a single-sideband modulation of the optical radiation, which is necessary for measuring small velocities of biological flows and determining the flow direction [8, 9].

The results of our previous investigations showed good prospects for using the method of speckle interferometry for *in vivo* evaluation of local lymph flow [5, 10, 11]. This method ensured a rapid and relatively simple measurement of the lymph flow velocity. Unfortunately, it was only possible to calculate the relative average lymph flow velocity without determining the flow direction.

Here we describe for the first time the method and the experimental setup for the *in vivo* laser monitoring of temporal variations in the velocity and direction of lymph flow in the mesenteric microvessels of rat. The method is based on an analysis of the statistical properties of the dynamic speckle fields generated by focused laser radiation and ensures high spatial resolution. The results of determining the lymph flow velocity by the proposed method agree well with analogous data obtained by functional transmission microscopy. Using the new technique in combination with the latter method significantly expands the possibilities of diagnostics involving the study of cell flows with complicated dynamics.

Spatiotemporal correlation of dynamic speckle fields. An approximate optical model of the lymph flow in a microvessel with a diameter of about 100 μm, at a cell concentration in the lymph on the order of 10%, is provided by a random phase screen (RPS) model [10, 11]. Let us consider the scattering of a beam of coherent radiation from a moving RPS. The spatiotemporal correlation function of the scattered light intensity at two points is as follows [12]:

$$g_1(\mathbf{r}, \tau) - 1 = \exp\left(-\frac{|\mathbf{v}|^2}{w^2}\tau^2\right)\exp\left(-\frac{1}{r_s^2}\left|\mathbf{r} - \left(1 + \frac{l}{\rho}\right)\mathbf{v}\tau\right|^2\right), \qquad (1)$$

where $\mathbf{r}$ is the difference of coordinates of the two points in the observation plane, τ is the delay time, $\mathbf{v}$ is the RPS velocity, w is the radius of the illuminated RPS area, ρ is the radius of curvature of the wave front in the RPS plane, l is the distance from the RPS plane to the observation plane, $r_s = 2l/(k_0 w)$ is the average speckle size, and k_0 is the incident radiation wavenumber.

As can be seen from Eq. (1), the speckle field is translated in the observation plane at a velocity

$$\mathbf{V}_s = \frac{\mathbf{r}}{\tau_d} = \left(1 + \frac{l}{\rho}\right)\mathbf{v}, \tag{2}$$

where τ_d is the position of maximum of the correlation function. During this, the structure of the speckle field continuously changes and, after traveling a distance

$$r_T = \left(1 + \frac{l}{\rho}\right)w, \tag{3}$$

the correlation decreases e times. In the case when $\mathbf{r}$ is parallel to $\mathbf{v}$, $|\mathbf{r}| \ll r_T$, and $\rho \ll l$, relation (2) yields a simple expression for the flow velocity:

$$v \approx \frac{\rho}{l}\frac{r}{\tau_d}. \tag{4}$$

Thus, in the approximation of a single uniformly moving thin RPS and a fixed scattering geometry, the position τ_d of the maximum of the mutual correlation function of the dynamic speckle field is inversely proportional to the flow velocity.

Experimental setup. Figure 1 shows a schematic diagram of the experimental setup based under a biological microscope for *in vivo* laser monitoring of the flow velocity of biological fluids in microvessels. The radiation of a He–Ne laser (LG-207, λ = 633 nm) is transmitted through the illumination channel and focused by the microscope lens in a plane spaced by about 100 μm from the axis of a microvessel studied. The radiation scattered from the lymph flow is detected by two photodetectors situated at a distance of 300 mm from the objective plane of the microscope. The working area diameter of each photodetector is 3 mm, which corresponds to an average speckle diameter in the observation plane. The distance between the centers of photodetectors (7 mm) is significantly smaller than the r_T value given by formula (3). The centers of photodetectors are situated on the line parallel to the direction of translation of the speckle field.

The output signals of the photodetectors are amplified by the photocurrent converters and digitized by a two-channel 16-digit analog-to-digital converter. The frequency of discretization is selected depending on the interval of flow velocities measured. The data are fed into a personal computer, which constructs a mutual correlation function of the signals from photodetectors, determines the position of maximum, and calculates the flow velocity.

A digital video camera mounted on the microscope column monitors the sample (rat mesentery) area simultaneously with registration of the speckle signals. From this record, it is possible to determine the average lymph flow direction and velocity (in μm/s), as well as some other parameters of the lymph microcirculation (microvessel diameter, phase contractility, and valve operation). In order to avoid illumination of the camera by the laser radiation and illumination of the photodetectors by the microscope illuminator, the camera objective and illuminator are equipped with green light filters, while the photodetectors are provided with a red light filter.

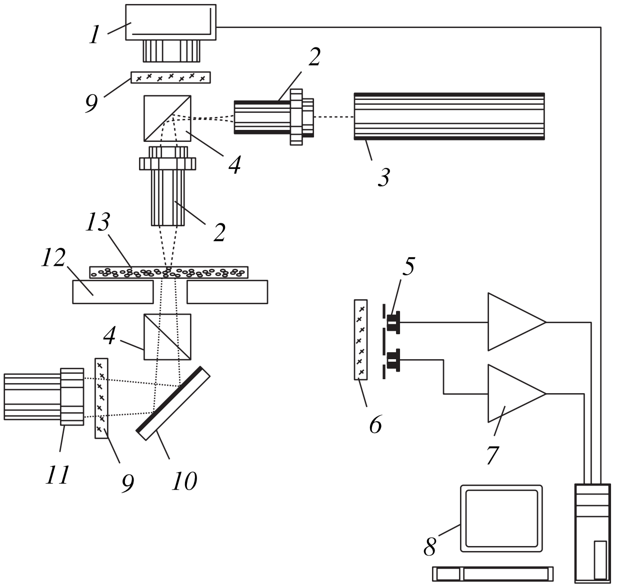

Fig. 1. A schematic diagram of the setup for the *in vivo* laser monitoring of the lymph flow dynamics in microvessels: (*1*) digital video camera; (*2*) microobjective; (*3*) He–Ne laser; (*4*) beam splitter; (*5*) photodiodes; (*6*) red filter; (*7*) photocurrent converter-preamplifier; (*8*) personal computer; (*9*) green filter; (*10*) mirror; (*11*) illuminator; (*12*) temperature-controlled stage; (*13*) lymphatic microvessel (rat mesentery).

The experiments were performed on white mongrel rats. A narcotized animal was placed on a temperature-controlled stage of the microscope. The lymph flow was studied *in vivo* in a mesentery of the small intestine in the transillumination mode.

Results and discussion. The experimental setup described above allows variations in the velocity and direction of the motion of cells at the intersection of the laser beam and the lymph microvessel to be monitored on a real time scale. The measurements are performed at a time resolution of 20 ms in a velocity range from 10 μm/s to 10 mm/s.

Figure 2 shows a typical record of the lymph flow velocity versus time in a rat mesenteric microvessel with a diameter of 150 μm. The record of the laser velocimeter (curve *a*) is compared to the data obtained upon processing of the video record (curve *b*). As can be seen, the curves show a good mutual correspondence

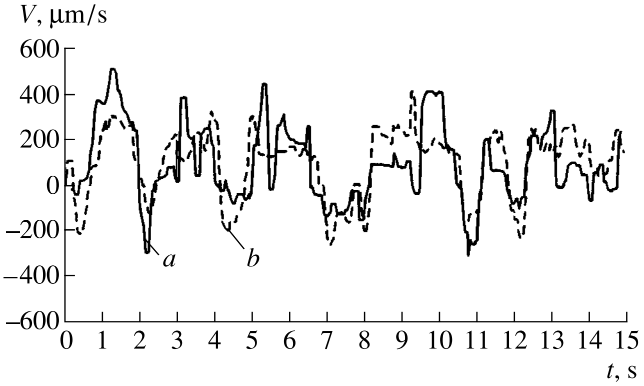

Fig. 2. Time variation of the lymph flow velocity in a microvessel (*a*) monitored by the laser velocimeter and (*b*) restored from the functional transmission microscopy record.

between the data obtained by the two independent techniques. A certain scatter in the values of flow velocity is explained by the fact that the video-record processing gives the average velocity of cells in the whole cross section of the vessel studied, while the laser velocimeter measured only the average velocity of the cells crossing a probed region with a diameter of about 40 μm situated in the central part in the lymphatic microvessel.

It should be noted that determination of the lymph velocity using a video record is a very laborious procedure, since it is necessary to measure the cell positions in each sequential shot, followed by averaging of the calculated values over the whole sequence. At the same time, transmission microscopy gives absolute values of the lymph flow, which are necessary for calibrating the relative velocities determined from the speckle interferometry data.

Conclusion. The proposed method of determining the lymph flow velocity with an allowance for the flow direction is simple in realization and allows the lymph flow dynamics to be monitored *in vivo* on a real time scale. Using a laser velocimeter for monitoring time variations of the lymph flow velocity significantly increases the possibilities of functional microscopy, which is still one of the basic methods for investigation of the microcirculation of biological fluids [6].

Acknowledgments. This study was supported by the Russian Foundation for Basic Research (project no. 00-15-96667 of the Leading Scientific Schools Program) and by the US Civilian Research and Development Foundation for Independent States of the Former Soviet Union (CRDF Award no. REC-006).

REFERENCES

1. N. G. McHale, News Physiol. Sci. **10**, 112 (1995).
2. V. M. Buyanov and A. A. Alekseev, *Lymphology of Endotoxicosis* (Meditsina, Moscow, 1990).
3. A. A. Gashev, Fiziol. Zh. SSSR im. I.M. Sechenova **77** (7), 63 (1991).
4. D. A. Berk, M. A. Swartz, A. J. Leu, and R. K. Jain, Am. J. Physiol. **270**, H330 (1996).
5. G. E. Brill’, E. I. Galanzha, S. S. Ul’yanov, *et al.*, Fiziol. Zh. im. I.M. Sechenova **87** (5), 600 (2001).
6. Yu. I. Gurfinkel’, V. V. Lyubimov, V. N. Oraevskiĭ, *et al.*, Biofizika **40** (4), 793 (1995).
7. B. S. Rinkevichyus, *Laser Diagnostics of Flows* (Mosk. Énerg. Inst., Moscow, 1990).
8. T. Eiju, M. Nagai, K. Matsuda, *et al.*, Opt. Eng. **32** (1), 15 (1993).
9. B. A. Levenko, A. V. Priezzhev, S. G. Proskurin, *et al.*, Izv. Akad. Nauk, Ser. Fiz. **59** (6), 162 (1995).
10. S. S. Ulyanov, V. V. Tuchin, A. A. Bednov, *et al.*, Lasers Med. Sci. **12**, 31 (1997).
11. S. S. Ulyanov, J. Biomed. Opt. **3** (3), 237 (1998).
12. T. Yoshimura, J. Opt. Soc. Am. A **3** (7), 1032 (1986).

Translated by P. Pozdeev

Technical Physics Letters, Vol. 28, No. 8, 2002, pp. 693–695. Translated from Pis'ma v Zhurnal Tekhnicheskoĭ Fiziki, Vol. 28, No. 16, 2002, pp. 65–70.

The Energy Spectrum of Charge Carriers in a Strongly Oblate Ellipsoidal Quantum Dot

G. G. Zegrya, O. V. Konstantinov, and A. V. Matveentsev
Ioffe Physicotechnical Institute, Russian Academy of Sciences, St. Petersburg, 194021 Russia

Received March 28, 2002

Abstract—A new method of introducing curvilinear coordinates for an oblate ellipsoid of revolution is developed, which is valid for charge carriers obeying a parabolic isotropic dispersion law. Using this method, simple analytical formulas are derived for the energy spectrum of carriers in an oblate ellipsoidal quantum dot. According to these expressions, there are energy levels of two types. The first type is characterized by a quantum number corresponding to the motion of carriers predominantly along the minor axis of the ellipsoid. The distances between levels of the first type are large: only one such level is found in an InAs quantum well confined between GaAs layers. The second type is characterized by a quantum number corresponding to the motion of carriers along the major axis of the ellipsoid. The distances between levels of the second type are small and many such levels can be sometimes accommodated in a quantum dot, their number rapidly increasing with the degree of oblateness of the ellipsoid. *© 2002 MAIK "Nauka/Interperiodica".*

Introduction. The case of a quantum well, in which the motion of carriers in the well plane is not quantized and the continuous spectrum of lateral motion forms a band, has been exhaustively studied. The well bottom corresponds to a level of the first type. It is important to note that the lowest energy level of this type in the quantum well corresponds to a nodeless wave function. In papers [1, 2], devoted to the theory of energy levels in a quantum dot (QD), it was assumed that the lowest state belongs to a different type, corresponding to a wave function with a single node at the center of the well. In the case of a parabolic dispersion law, such levels cannot be accommodated in the well. For this reason, previously [2] we used a nonparabolic law of dispersion, which allowed a state with a single-node wave function to exist at the QD center.

Below we demonstrate that a strongly oblate ellipsoid of revolution allows a bound ground state to exist, the wave function of which, like that in the quantum well, exhibits no nodes. This level is accompanied by a substructure of states with various quantum numbers corresponding to the motion along the major axis of the ellipsoid.

The ellipsoidal QD model. Consider an ellipsoidal QD with the shape determined by the equation

$$\frac{x^2+y^2}{b^2}+\frac{z^2}{r^2} = 1, \tag{1}$$

where r and b are the minor and major axes of the ellipsoid of revolution, respectively. Let us introduce the factor n, representing the ratio of axes so that $b = nr$, and a system of coordinates of the spherical type in which the ellipsoid surface represents a sphere of radius r = const:

$$x = nr\sin\theta\cos\varphi, \quad y = nr\sin\theta\sin\varphi, \quad z = r\cos\theta. \tag{2}$$

However, this system is not convenient because the curvilinear coordinates are not orthogonal. In order to demonstrate this, let us consider the square of a length element,

$$ds^2 = dx^2+dy^2+dz^2, \tag{3}$$

where dx, dy, dz are differentials of the Cartesian coordinates related to the curvilinear coordinates r, θ, φ by expressions (2). Calculation of the square of a length element in the curvilinear coordinates yields

$$\begin{aligned} ds^2 &= dr^2+r^2d\theta^2+n^2r^2\sin^2\theta d\varphi^2 \\ &\quad +(n^2-1)[\sin\theta dr+r\cos\theta d\theta]^2. \end{aligned} \tag{4}$$

As can be seen from this formula, the coordinates r, θ are mutually orthogonal only for $n = 1$. Upon substituting variables

$$R = r\sin\theta; \quad dR = \sin\theta dr + r\cos\theta d\theta, \tag{5}$$

we obtain

$$ds^2 = dr^2+r^2d\theta^2+n^2R^2d\varphi^2+(n^2-1)dR^2. \tag{6}$$

Let us consider the limiting case of a strongly oblate ellipsoid ($n \gg 1$). In this case, the term $r^2d\theta^2$ can be ignored and the curvilinear coordinates r, R, φ become orthogonal since the squared arc length contains no cross products of differentials of the curvilinear coordinates:

$$ds^2 = dr^2 + n^2 dR^2 + n^2 R^2 d\varphi^2. \tag{7}$$

Note that the factors at the squares of differentials of the curvilinear coordinates in expression (7) represent the squares of the Lamé coefficients [3] in these coordinates:

$$H_r = 1; \quad H_R = n; \quad H_\varphi = nR. \tag{8}$$

Using these coefficients, it is easy to construct the Laplacian for a strongly oblate ellipsoid with $n \gg 1$ (see, e.g., [3]):

$$\nabla^2\Psi = \frac{\partial^2\Psi}{\partial r^2} + \frac{1}{n^2}\left[\frac{1}{R}\frac{\partial}{\partial R}\left(R\frac{\partial\Psi}{\partial R}\right) + \frac{1}{R^2}\frac{\partial^2\Psi}{\partial\varphi^2}\right], \tag{9}$$

which is analogous to the Laplacian in a cylindrical coordinate system.

The substructure of quantum levels. Consider the Schrödinger equation

$$-\frac{\hbar^2}{2m}\nabla^2\Psi = E\Psi, \tag{10}$$

$$E = \frac{\hbar^2}{2m}(k^2 + p^2) = E(k) + E(p), \tag{11}$$

where k and p are the discrete components of a quasi-wave vector, the values of which are determined from the boundary conditions of a given problem. For the variables φ and R, the boundary conditions express a cyclic character of the wave function. As for the variable r, the boundary conditions correspond to finiteness and continuity of the wave function at $r = 0$ and to continuity of the wave function and its derivative along the normal on the surface $r = a$. Under these boundary conditions, the Hamiltonian of Eq. (10) admits the separation of variables. For this purpose, we can seek a wave function in the form of a product of three functions

$$\Psi = e^{iM\varphi}\chi(R)\eta(r). \tag{12}$$

In view of the periodicity of the wave function with respect to variable φ, the quantum number M must be an integer ($M = 0, 1, 2, \ldots$).

According to Eq. (11), the energy is a sum of two terms. The first term $E(k)$ represents the energies of levels corresponding to the electron motion along the radial coordinate r. The spectrum of these energies is characterized by large distances between levels. The second term $E(p)$ describes a substructure of the energy levels and corresponds to the motion of electrons predominantly along the major axis of the ellipsoid. After the separation of variables, Eq. (11) yields two one-dimensional equations. One of these, corresponding to the motion of carriers predominantly along the radius, determines the ground state with a nodeless wave function $\eta(r) = \cos kr$. The other equation, corresponding to the motion of carriers along the major axis of the ellipsoid, is as follows:

$$\frac{1}{R}\frac{d}{dR}\left(R\frac{d\chi}{dR}\right) - \frac{M^2}{R^2}\chi = -p^2 n^2 \chi^2. \tag{13}$$

Taking into account that the wave function must be finite at $R = 0$, a solution to Eq. (13) can be expressed through a Bessel function with an integer index M:

$$\chi(R) = J_M(KR), \quad K = pn. \tag{14}$$

Now let us change the reference direction for counting the polar angle. To this end, we pass from θ to the new variable $\theta' = \frac{\pi}{2} - \theta$, for which $R = r\cos\theta'$. The new limits of variation of the variables are as follows: $-\pi/2 < \theta' < \pi/2$; $-a < R < a$. For an even M, the solution represents an even function $\Psi(R) = \Psi(-R)$. The boundary condition at $\theta' = \pi/2$ ($R = 0$) consists in that the derivative must be continuous. Since the function χ must be even with respect to the angle θ', the derivative must turn zero at $\theta' = \pi/2$ (i.e., at $R = 0$), otherwise the function would exhibit a break at this point. Thus, the boundary condition for an even M reduces to the requirement that the derivative must be zero ($j'_M = 0$) at $R = 0$. For an odd M, the solution represents an odd function $\Psi(R) = -\Psi(-R)$. In this case, the boundary condition at $\theta' = \pi/2$ ($R = 0$) consists in that the function must be zero (i.e., $J_M = 0$). Thus,

$$J'_M(P) = 0, \quad M = 0, 2, \ldots; \quad J_M(Q) = 0, \quad M = 1.3, \ldots. \tag{15}$$

The roots of these equations are known (see, e.g., the handbook [4]). Each root is characterized by the number s: $P \equiv P_s(M)$, $Q \equiv Q_s(M)$ ($s = 1, 2, 3, \ldots$). The first roots in this series are as follows: $P_1(0) = 0$; $P_1(2) \approx 3.0$; $Q(1) = P_2(0) \approx 3.8$. It should be emphasized that the equation for the derivative has a zero root (corresponding to a zero energy) for the motion along the major axis.

Numerical values of energies. The main feature of the above solution is that the system always has at least one bound state $E(k)$ for any effective mass and an arbitrary potential step at the quantum well boundary. For this reason, the proposed theory can be applied to description of the energy spectrum of electron within the framework of a parabolic model. Let us assume that the energies of electrons and holes inside the well obey the parabolic dispersion law:

$$E_{c,v}(k) = \frac{\hbar^2 k^2}{2m_{c,v}}, \tag{16}$$

where $m_c = 0.027m_0$ and $m_v = 0.41m_0$ are tabulated values of the effective electron and hole masses, respectively, in an InAs crystal. Outside the well in the GaAs crystal, the corresponding effective masses of charge carriers are as follows:

$$m_{cB} = 0.065 m_0, \quad m_{vB} = 0.45 m_0. \tag{17}$$

In this region, the wave function is described by the exponent exp(–*qr*), where

$$q^2 = \frac{2m_B}{\hbar^2}[\Delta E - E_{c,v}(k)], \tag{18}$$

m_B is the carrier (electron or hole) mass in GaAs given by formulas (17), and the corresponding potential steps at $T = 300$ K are equal to $\Delta E_c = 0.70$ eV and $\Delta E_V = 0.38$ eV. Discrete values of the radial component of the wave vector inside the sphere are determined by the well-known equation following from the conditions of continuity of the function and its derivative at the boundary $r = a$:

$$\tan(ka) = -\frac{q}{k}, \tag{19}$$

the values of k representing the solutions of Eq. (19) determining the energies of distant levels $E(k)$ in the well. Calculations show that a 24-Å-thick InAs quantum well confined between GaAs layers contains a single radial electron state with an energy of $E(k) = 0.53$ eV.

In the case of an ellipsoid with $d = 24$ Å and the axial ratio $n = 8$ (at a major semiaxis length of $l = 190$ Å), we obtain four electron energy states with the wave functions J_0, J_2, J_0, J_1; the two last states are degenerate. The energies of these states are $E_0 = 0.53$ eV, $E_3 = 0.62$ eV, and $E_1 = E_2 = 0.68$ eV. For holes (possessing a greater effective mass), there are two radial states. Each of the two corresponds to a substructure with respect to the angular variables. A ground state with respect to the radial variable corresponds to 57 energy states with respect to the angular variables, which fall within an energy gap at the QD boundary. The excited state with a single node in the radial variable corresponds to 18 energy states with respect to the angular variables.

In concluding, let us consider two other sets of dimensions of the model quantum dots. The first case is 30 Å × 100 Å with an axial ratio of $n = 3.33$. In this case, there are 39 energy levels for holes, which are spaced at least by 0.058 eV from the valence band top, and two electron energy levels with $E_0 = 0.453$ eV and $E_1 = 0.688$ eV. The second case represents a QD with dimensions of 30 Å × 300 Å and an axial ratio of $n = 10$. Here, there are 12 energy levels for electrons and an enormously large number of states for holes (on the order of several hundreds).

REFERENCES

1. L. V. Asryan and R. A. Suris, Semicond. Sci. Technol. **11**, 554 (1996).
2. V. P. Evtikhiev, O. V. Konstantinov, and A. V. Matveentsev, Pis'ma Zh. Tekh. Fiz. **27** (6), 65 (2001) [Tech. Phys. Lett. **27**, 248 (2001)].
3. V. I. Smirnov, *A Course of Higher Mathematics* (GITTL, Moscow, 1954; Addison-Wesley, Reading, 1964), Vol. II.
4. *Handbook of Mathematical Functions,* Ed. by M. Abramowitz and I. A. Stegun (National Bureau of Standards, Washington, 1964; Nauka, Moscow, 1979).

Translated by P. Pozdeev

Technical Physics Letters, Vol. 28, No. 8, 2002, pp. 696–698. Translated from Pis'ma v Zhurnal Tekhnicheskoĭ Fiziki, Vol. 28, No. 16, 2002, pp. 71–78.
Original Russian Text Copyright © 2002 by Aleksandrov, Alekseev, Demidov, Dudin, Katsavets, Kogan, Pogorel'skiĭ, Ter-Martirosyan, Sokolov, Chaly, Shkurko.

High-Power Low-Threshold Laser Diodes (λ = 0.94 μm) Based on MBE-Grown $In_{0.1}Ga_{0.9}As$/AlGaAs/GaAs Heterostructures

S. B. Aleksandrov, A. N. Alekseev, D. M. Demidov, A. L. Dudin,
N. I. Katsavets, I. V. Kogan, Yu. V. Pogorel'skiĭ, A. L. Ter-Martirosyan,
É. G. Sokolov, V. P. Chaly, and A. P. Shkurko
ATC-Semiconductor Devices Joint-Stock Company, St. Petersburg, Russia
e-mail: ter@atc.rfntr.neva.ru
ATC-Semiconductor Technologies and Equipment, Joint-Stock Company, St. Petersburg, Russia
e-mail: atcste@mail.fi.ru

Received March 26, 2002

Abstract—The parameters of high-power laser diodes operating at λ = 0.94 μm, based on MBE-grown $In_{0.1}Ga_{0.9}As$/AlGaAs/GaAs quantum-dimensional heterostructures, are reported. The laser diodes manufactured using an optimized MBE technology and specially selected dopant profiles are characterized by a low threshold current density, a high optical output power, a high differential quantum efficiency, and a long working life (above 10000 h). © *2002 MAIK "Nauka/Interperiodica".*

High-power laser diodes emitting in a wavelength interval of 0.96–0.98 μm are widely used for the pumping of Er^{3+} ions in solid-state lasers and optical fiber laser amplifiers. Fabricated using laser heterostructures with separate electronic and optical confinement, based on $In_{0.2}Ga_{0.8}As$ quantum-dimensional active regions, such diodes are characterized by high efficiency, good reliability, and long working life [1–3].

At the same time, some applications (e.g., solid-state lasers based on Yb^{3+} ions possessing a maximum absorption at 0.94–0.95 μm [4]) require increased energy of the laser diode radiation quantum. Accordingly, the concentration of In in the active region has to be reduced.

Below we will consider some features of the fabrication technology of $In_{0.1}Ga_{0.9}As$/AlGaAs/GaAs quantum-dimensional heterostructures, which was optimized so as to obtain high-power laser diodes with a low threshold current density, low internal losses, and a high differential quantum efficiency. We have also studied the optical and temporal characteristics of laser diodes based on heterostructures grown using the optimized technology.

The laser heterostructures were grown by molecular beam epitaxy (MBE) in a domestic system of the EP1203 type, which was modified so as to provide for a reproducible growth of the structures with an InGaAs active region. The most important changes are as follows:

(i) A modified unit used for the dynamic heating of substrates facilitates the formation of heterojunctions at a significant difference of the growth temperatures for the AlGaAs wavegude (~700°C) and the InGaAs active region (540–560°C).

(ii) An indium-free sample holder, specially designed for the EP1203 system, ensures a high homogeneity of the layer parameters over the area of the heterostructure.

(iii) A new gallium source, based on an evaporator with a quasi-two-zone heating of the crucible, significantly decreases the density of oval defects on the heterostructure surface and, hence, markedly increases the product yield.

The substrate temperature was monitored, in addition to reflection high-energy electron diffraction, by high-precision optical pyrometry.

The laser heterostructures were grown by classical design, comprising a graded-index waveguide layer of undoped $Al_xGa_{1-x}As$ ($x = 0.6 \longrightarrow 0.3 \longrightarrow 0.6$) with a total thickness of 0.3 μm between $Al_xGa_{1-x}As$ emitters ($x = 0.6$). Inside the waveguide layer was placed a 9-nm-thick $In_yGa_{1-y}As$ active region bounded by 3-nm-thick GaAs layers (Fig. 1a). The results of modeling showed that these MBE-grown laser heterostructures must be characterized by an optical confinement factor of $\Gamma = 0.034$ and a halfwidth of the laser diode far field pattern (in the direction perpendicular to the *p*–*n* junction) $\theta_\perp = 40°$, which agrees well with the experimentally measured values.

Materials of the *n* and *p* types were doped with silicon and beryllium, respectively. The dopant profile in the emitter layers was optimized so as to minimize the internal optical losses. Optimization of the process technology consisted in selecting the MBE parameters (temperature, growth rate, and ratio of the fluxes of III and V group elements) for the growth of the InGaAs active layer.

The quality of the epitaxially grown semiconductor material was checked by measuring the photoluminescence (PL) of test heterostructures with a design closest to that of the laser heterostructures. The spectra of PL and laser diode emission were measured in a standard setup based on an MDR-23 monochromator. The PL spectra were excited by a solid-state Nd^{3+} laser (λ = 0.53 μm) with an intensity of about 100 W/cm^2. The internal quantum yield (η_{int}) was estimated by comparing the PL intensity of the test structures to that of the reference samples according to an approach described in [5]. Optimization of the growth technology increased reproducibility of the internal quantum yield of PL above 90% over the entire area of the test structures (Fig. 1b).

The internal optical losses (α_{int}) and the through current density (J^0_{th}) of the laser heterostructures [6] were determined from the dependence of the inverse differential quantum efficiency ($1/2\eta$) on the laser diode resonator length (L) and from a plot of the threshold current density (J_{th}) versus the inverse resonator length. The laser diode chips with a contact strip of width W = 100 μm, which were prepared using a standard post-growth processing technology but bore no special coatings on the mirrors, were soldered with an In-containing solder to copper heat sinks (with *p*-sides facing the metal). The measurements were performed using laser diodes operating in a continuous wave mode at a heat sink temperature of 25°C. The samples with mirrors were prepared by depositing a multilayer dielectric reflecting coating onto the rear face of the laser diode resonator, and an antireflection film, onto the front face of the resonator; the reflection coefficients of these films were 95 and 5%, respectively.

The long-term tests of laser diodes were conducted in the regime of stabilized constant pumping current, at an initial optical output power of P = 1 W. The tests were performed under normal conditions (T = 25°C) and at an elevated temperature (T = 50°C) leading to more than tenfold acceleration of the degradation processes [7]. The test duration was not less than 1000 h in the former case and not less that 200 h in the latter case. The expected working life of laser diodes was estimated by linear extrapolation of the time variation of the optical output power to 80% of the initial value.

Figure 2a shows the plots of $1/2\eta$ versus L and J_{th} versus $1/L$. A linear approximation of the former plot [7] yields an estimate of α_{int} = 1.5 cm^{-1} and η_{int} = 98%. Note that α_{int} is close to the record value reported for a laser diode with the classical design [8, 9]. The through current density J^0_{th} determined from the plot of J_{th} versus $1/L$ is J^0_{th} = 70 A/cm^2, which agrees well with the threshold current density of the four-cleaved samples measured in a pulsed regime (τ = 2 μs).

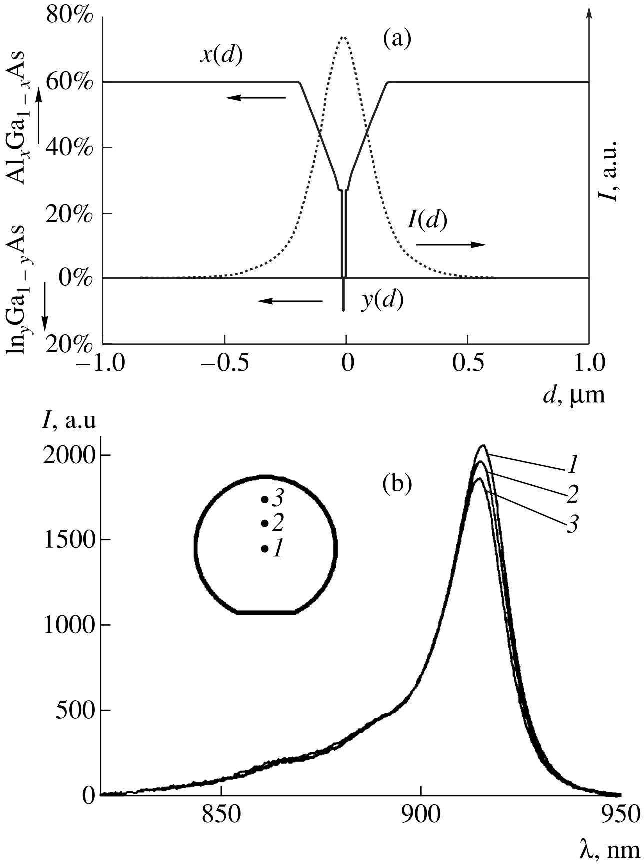

Fig. 1. (a) The design of $Al_xGa_{1-x}As/In_yGa_{1-y}As/GaAs$ laser heterostructures, the $x(d)$ and $y(d)$ profiles, and the calculated near-field diagram $I(d)$ at the laser diode mirror; (b) the PL spectrum of a laser heterostructure and its variation over the surface of a test structure with a diameter of 32.4 mm. The inset indicates the sites of PL measurements.

Figure 2b shows the plots of optical output power P_{opt} versus pumping current for two laser diodes with different resonator lengths, based on the heterostructures grown by the optimized technology. The laser diodes possess a high differential quantum efficiency at a low threshold current density (η = 65%, J_{th} = 100 A/cm^2 and η = 70%, J_{th} = 120 A/cm^2 for L = 2000 and 1000 μm, respectively). The characteristic temperature calculated from the temperature dependence of the laser diode threshold current is T_0 = 150°C.

Measurements of the laser diode emission spectra showed that the emission intensity maximum takes place at 945 ± 3 nm and shifts with a temperature coefficient of 0.27 nm/K. The halfwidth of the laser emission band does not exceed 1.5 nm. Long-term tests using a batch of 30 laser diodes showed the absence of the so-called “fast” degradation mechanism usually related to “dark line defects” [10, 11] (leading to a sig-

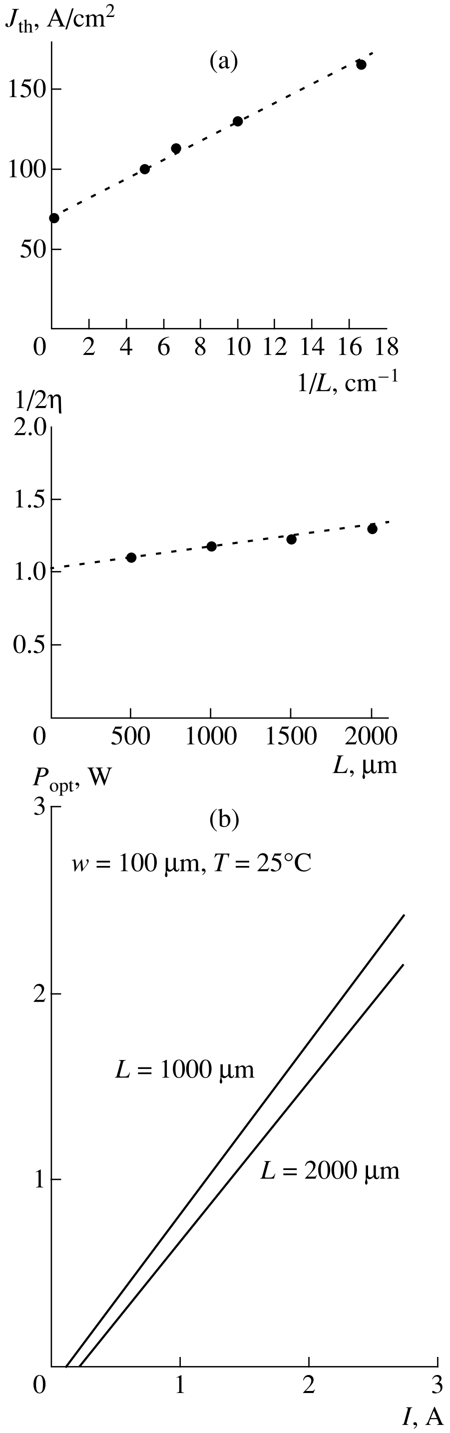

Fig. 2. Characteristics of laser diodes: (a) dependences of the inverse differential quantum efficiency ($1/2\eta$) and threshold current density (J_{th}) on the resonator length; (b) dependence of the optical output power P_{opt} on the pumping current I for different resonator lengths L.

nificant drop in P_{opt} within several tens of hours). The "slow" degradation rate of the tested laser diodes was < 2×10^{-5} h^{-1}, which corresponds to an expected working life of not less than 10000 h.

Thus, optimization of the MBE growth conditions and the dopant profile allowed us to obtain low-threshold (J^0_{th} = 70 A/cm^2) $In_{0.1}Ga_{0.9}As/AlGaAs/GaAs$ laser heterostructures characterized by a high internal efficiency (η_{int} = 98%) and low internal optical losses (α_{int} = 1.5 cm^{-1}). The laser diodes based on these heterostructures operate at 945 nm and possess a high differential quantum efficiency (η > 65%), low threshold current density (J_{th} = 100 A/cm^2), and a working life above 10000 h.

The optimized MBE technology provides for stable growth of laser heterostructures of the classical design with parameters ensuring fabrication of low-threshold long-life laser diodes with an output power of 1 W at an emitting dimension of 100 μm. Further increase in the limiting optical output power of laser diodes requires, first, a change in the heterostructure design toward increasing waveguide width and, second, a certain modification of some postgrowth processing stages. At present, research in both directions is in progress and the results will soon be published.

Acknowledgments. The authors are grateful to R.V. Leus for his help in the postgrowth treatment of laser heterostructures.

REFERENCES

1. H. K. Choi and C. A. Wang, Appl. Phys. Lett. **57** (4), 321 (1990).
2. T. Takeshita, M. Okayasu, O. Kogure, and S. Uehara, Jpn. J. Appl. Phys. **29** (7), L1138 (1990).
3. N. Chand, N. G. Chu, N. K. Dutta, *et al.*, IEEE J. Quantum Electron. **30 (**2), 424 (1994).
4. N. Pavel, J. Saikawa, and T. Taira, Jpn. J. Appl. Phys. **40** (1), 146 (2001).
5. Zh. I. Alferov, D. Z. Garbuzov, A. G. Denisov, *et al.*, Fiz. Tekh. Poluprovodn. (Leningrad) **22** (12), 2105 (1988) [Sov. Phys. Semicond. **22**, 1331 (1988)].
6. H. C. Casey, Jr. and M. B. Panish, *Heterostructure Lasers*, Part B: *Materials and Operating Characteristics* (Academic, New York, 1978).
7. H. Ishikawa, T. Fujiwara, K. Fujiwara, *et al.*, J. Appl. Phys. **50** (4), 2518 (1979).
8. J. Wang, B. Smith, X. Xie, *et al.*, Appl. Phys. Lett. **74** (11), 1525 (1999).
9. D. A. Livshits, A. Yu. Egorov, I. V. Kochnev, *et al.*, Fiz. Tekh. Poluprovodn. (St. Petersburg) **35** (3), 380 (2001) [Semiconductors **35**, 365 (2001)].
10. V. P. Chaly, M. I. Etinberg, G. A. Fokin, *et al.*, Semicond. Sci. Technol. **9**, 345 (1994).
11. S. L. Yellen, A. H. Shepard, R. J. Dalby, *et al.*, IEEE J. Quantum Electron. **29** (6), 2058 (1993).

Translated by P. Pozdeev

Technical Physics Letters, Vol. 28, No. 8, 2002, pp. 699–701. Translated from Pis'ma v Zhurnal Tekhnicheskoĭ Fiziki, Vol. 28, No. 16, 2002, pp. 79–84.
Original Russian Text Copyright © 2002 by Ishimov, Senokosov, Dement'ev, Goglidze.

Technological Conditions for Optimization of the Optoelectronic Parameters of the $(As_2S_3)_x(As_2Se_3)_{1-x}$ Glassy Semiconductor Films on a Polymer Roll Base

V. M. Ishimov, É. A. Senokosov, I. V. Dement'ev, and T. I. Goglidze
Trans-Dniester State University, Tiraspol
e-mail: feshenko@mail.ru

Received February 26, 2002

Abstract—We have experimentally studied dependence of the optoelectronic parameters (resistance, photosensitivity, drift mobility, and optical absorption edge) of thin $(As_2S_3)_x(As_2Se_3)_{1-x}$ glassy semiconductor films on the rate of their thermal deposition in vacuum onto a Lavsan (Dacron) roll base. Films obtained at the optimum deposition rates, ranging from 4 to 7×10^{-3} μm/s, are characterized by greater values of the resistance, photosensitivity, and drift mobility, while the absorption edge approaches a value typical of a bulk glassy semiconductor. The influence of pores, formed in the volume of the deposit, on the physical properties of the films is discussed. © *2002 MAIK "Nauka/Interperiodica".*

Thin films of glassy chalcogenide semiconductors (GCSs) based on $(As_2S_3)_x(As_2Se_3)_{1-x}$ solid solutions are widely used in silverless photography, holography, copying techniques, and recording media [1]. In particular, such films are employed in electrophotography (Xerox) and photothermoplastic memory devices [2]. GCS films are most frequently obtained on a metallized polymer roll base by thermal deposition in vacuum [3]. However, this technology has still not been completely developed and cannot ensure the obtaining of multicomponent GCS films with preset homogeneous parameters. This requirement is of primary importance for thin-film materials on a polymer roll base. The search for optimum technological conditions and the corresponding methods of control, which would provide for the obtaining of $(As_2S_3)_x(As_2Se_3)_{1-x}$ with reproducible parameters, permanently draws the attention of researchers.

We have studied the dependence of the main optoelectronic properties of thin GCS films with the compositions $(As_2S_3)_x(As_2Se_3)_{1-x}$ ($x = 0$, 0.3, 0.5, 0.7, and 1.0) on the rate w of their thermal deposition in vacuum onto moving metallized Lavsan (Dacron) ribbons. The process was conducted in a special device [4] which maintained constant composition of a multicomponent vapor and allowed the vapor density to be controlled within broad limits. The GCS film thickness was d = 1.2–1.5 μm.

Variation of the dark resistivity ρ and photosensitivity k (characterizing a change of the resistance under illumination) were monitored by a contactless method based on the potential decay measurements in the dark and under illumination [5]. Table 1 presents the ρ and k values measured at 300 K using an illumination intensity of 15 lx for $(As_2S_3)_x(As_2Se_3)_{1-x}$ films of various compositions. As can be seen, both the resistivity and photosensitivity of the films depend (under otherwise identical conditions) on the deposition rate. When the rate w increases up to 5×10^{-3} μm/s, the ρ and k values grow as well. As the w value increases further, the resistivity and photosensitivity begin to decrease.

Stationary current–voltage (I–U) characteristics of the GCS films were measured using sandwich structures with chromium (bottom) and bismuth (top) electrodes. It was found that $(As_2S_3)_x(As_2Se_3)_{1-x}$ films of all compositions exhibit I–U curves of identical shape, composed of portions approximated by the power law $j = AU^n$ with different exponents n. For electric field strengths $E < 5 \times 10^4$ V/cm, the current depends on the voltage according to the Ohm law ($n \approx 1$). The I–U curve portion measured for the greater fields strengths (from 5×10^4 to 10^6 V/cm) corresponds to $n \approx 2.2$–3.5. This is evidence of a current limited by the space charge of exponentially distributed traps [6]. In the region of fields $E > 10^6$ V/cm, the current exhibits a rapid buildup with $n \approx 7$–12.

We believe that a sharp growth of the space-charge-limited current in the latter region is explained by a limiting filling of traps, the concentration of which (n_t) is related to the applied voltage U as [7]

$$n_t = \frac{1}{4\pi}\frac{\varepsilon}{e_0 d^2}U, \qquad (1)$$

where ε is the static dielectric constant and e_0 is the

Table 1. The resistivity ρ, photosensitivity *k*, and local state (trap) density n_t in $(As_2S_3)_x(As_2Se_3)_{1-x}$ films obtained at various deposition rates on a Lavsan (Dacron) roll base

Composition $(As_2S_3)_x(As_2Se_3)_{1-x}$		Deposition rate *w*, 10^{-3} μm/s							
		1.0	2.0	3.0	4.0	5.0	6.0	7.0	8.0
$x = 1$	ρ, Ω cm	1.5×10^{-14}	2.3×10^{14}	2.4×10^{14}	2.5×10^{14}	3.1×10^{14}	2.7×10^{14}	2.6×10^{14}	2.1×10^{14}
	k	1.2	1.2	1.3	3.4	3.9	3.1	2.8	2.1
	n_t, cm^{-3}	8.5×10^{16}	8.2×10^{16}	7.8×10^{16}	7.6×10^{16}	7.3×10^{16}	7.2×10^{16}	7.9×10^{16}	8.1×10^{16}
$x = 0.7$	ρ, Ω cm	2.2×10^{14}	2.2×10^{14}	2.6×10^{14}	2.8×10^{14}	6.9×10^{13}	3.2×10^{14}	3.1×10^{14}	2.6×10^{14}
	k	1.9	2.2	4.5	7.9	9.7	9.4	7.5	6.3
	n_t, cm^{-3}	6.4×10^{16}	6.1×10^{16}	5.9×10^{16}	5.4×10^{16}	5.1×10^{16}	5.1×10^{16}	5.3×10^{16}	5.8×10^{16}
$x = 0.5$	ρ, Ω cm	2.1×10^{13}	2.5×10^{13}	3.4×10^{13}	4.7×10^{13}	1.3×10^{13}	3.2×10^{13}	2.7×10^{13}	2.2×10^{13}
	k	14.5	17.3	21.2	27.6	15.3	23	19	16
	n_t, cm^{-3}	4.7×10^{16}	4.2×10^{16}	3.9×10^{16}	3.7×10^{16}	3.1×10^{16}	3.2×10^{16}	3.4×10^{16}	3.8×10^{16}
$x = 0.3$	ρ, Ω cm	1.1×10^{13}	1.2×10^{13}	2.3×10^{13}	5.9×10^{13}	5.7×10^{13}	5.1×10^{13}	5.3×10^{13}	5.2×10^{13}
	k	7.5	10.9	12.5	19.4	25.8	27.7	25	22
	n_t, cm^{-3}	3.7×10^{16}	3.2×10^{16}	2.9×10^{16}	2.6×10^{16}	2.2×10^{16}	2.2×10^{16}	2.5×10^{16}	2.8×10^{16}
$x = 0$	ρ, Ω cm	5.9×10^{11}	4.6×10^{11}	4.6×10^{11}	8.5×10^{11}	4.3×10^{12}	3.9×10^{12}	3.6×10^{12}	9.1×10^{11}
	k	29	34	49	56	62	48	42	37
	n_t, cm^{-3}	2.2×10^{16}	1.7×10^{16}	1.4×10^{16}	9.1×10^{15}	9.2×10^{15}	9.4×10^{15}	1.2×10^{16}	1.4×10^{16}

electron charge. The values of n_t calculated by formula (1) are presented in Table 1. As can be seen from these data, the concentration of trap states in the films obtained at a given deposition rate increases with the As_2S_3 content in the $(As_2S_3)_x(As_2Se_3)_{1-x}$ films. In films of the same composition, the value of n_t is virtually independent of the deposition rate (in the interval studied).

Investigation of a drift mobility of the majority carriers (holes) by the time-of-flight technique showed that the mobility depends on the temperature according to the activation law $\mu = \mu_0 \exp(-E_a/kt)$ [9], where μ_0 is the hole mobility at $T = 0$ K and E_a is the mobility activation energy. The room-temperature mobilities for $(As_2S_3)_x(As_2Se_3)_{1-x}$ films of various compositions are presented in Table 2. As can be seen, the maximum mobility was observed for the As_2Se_3 films. As the content of As_2S_3 increases, the drift mobility of holes in the $(As_2S_3)_x(As_2Se_3)_{1-x}$ films decreases and the activation energy grows.

It was established that, for $\alpha < 10^3$ cm^{-1}, the $(As_2S_3)_x(As_2Se_3)_{1-x}$ films of all compositions studied exhibit an exponential dependence of the absorption coefficient on the incident photon energy $h\nu$, thus obeying the Urbach rule [10]:

$$\alpha = \alpha_0 \exp\left[-\frac{(h\nu - E_g)}{\bar{w}}\right], \qquad (2)$$

where E_g is the optical bandgap of this GCS and $\bar{w}$ is an energy parameter characterizing the slope (i.e., degree of smearing) of the absorption edge. Using (2), we determined the optical bandgaps E_g of the $(As_2S_3)_x(As_2Se_3)_{1-x}$ films studied (Table 2). It was also found that the deposition rate significantly influences the absorption edge, this effect being most pronounced in samples with a large content of As_2S_3. For example, as the deposition rate increases from 5.6×10^{-3} to 9.0×10^{-3} μm/s, the absorption edge of As_2S_3 shifts by 0.14 eV (against 0.05 eV for As_2Se_3). The high-energy shift is indicative of a decrease in length of the "tail" in the density of states.

We believe that the regularities observed in the influence of the deposition rate on the properties of thin $(As_2S_3)_x(As_2Se_3)_{1-x}$ films are related to the interaction of a deposit with residual gases present in the working volume of the technological chamber. Processes of the chemical and physical adsorption of the residual gas molecules on the substrate surface sharply reduce the ability of deposited atoms and molecules of GCS components to migrate over the substrate surface, thus favoring the formation of defects. At a small film deposition rate, the defects predominantly appear as a result of incorporation of the residual gas molecules into the GCS matrix, which is essentially equivalent to self-doping of the thin film. In the films of a given thickness grown at high deposition rates, defects are related pre-

Table 2. The drift mobility of majority charge carries and the energy parameters of $(As_2S_3)_x(As_2Se_3)_{1-x}$ films obtained at various deposition rates on a Lavsan (Dacron) roll base

Composition $(As_2S_3)_x(As_2Se_3)_{1-x}$	Deposition rate, μm/s	Drift mobility, cm^2/(V s)	Mobility activation energy, eV	Optical bandgap width, eV
$x = 1.0$	4.0×10^{-3}	5.3×10^{-8}	0.15	2.35
$x = 0.7$	6.0×10^{-3}	4.0×10^{-11}	0.18	2.17
$x = 0.5$	5.8×10^{-3}	3.7×10^{-10}	0.16	2.05
$x = 0.3$	4.5×10^{-3}	6.4×10^{-9}	0.13	1.93
$x = 0$	5.5×10^{-3}	1.4×10^{-7}	0.10	1.75

dominantly to the formation of various agglomerates containing a large number of broken bonds and micropores. Embedded into the matrix, the micropores form defects in the form of cavities. Cavities formed in the volume of a thin film represent voids [11] with a large number of surface states contributing to the electric conductivity and determining the charge transfer mechanism. A decrease in the density of micropores leads to an increase in resistance of the film. The photosensitivity of such films increases due to a decrease in the dark conductivity.

Based on the results of investigation of the properties of $(As_2S_3)_x(As_2Se_3)_{1-x}$ films deposited in vacuum onto a Lavsan (Dacron) roll base, we established the interval of optimum deposition rates, $(4–7) \times 10^{-3}$ μm/s. Films deposited at a rate in this interval exhibit maximum resistivity and photosensitivity; the drift mobility of the majority carriers is also at maximum. The optical absorption edge position in such films corresponds to a maximum optical bandgap E_g and approaches the value typical of a bulk glassy semiconductor of the same composition.

REFERENCES

1. V. M. Lyubin, *Structure and Properties of Noncrystalline Semiconductors* (Nauka, Leningrad, 1976), pp. 415–425.
2. L. M. Panasyuk, in *Proceedings of the International Congress on Highly Sensitive Photography and Photonics, Moscow, 1980*, p. 318.
3. Great Britain Patent No. 2055154 B, C 23 C 13/10.
4. É. A. Senokosov, V. M. Ishimov, and I. V. Dement'ev, PMR Patent No. 01100229 (2001).
5. S. G. Grenishin, *Electrophotographic Process* (Nauka, Moscow, 1970).
6. A. Rose, *Concepts in Photoconductivity and Allied Problems* (Interscience, New York, 1963; Mir, Moscow, 1966).
7. M. A. Lampert and P. Mark, *Current Injection in Solids* (Academic, New York, 1970; Mir, Moscow, 1973).
8. W. F. Spear, J. Non-Cryst. Solids **1**, 197 (1969).
9. V. I. Arkhipov and A. I. Rudenko, Phys. Lett. A **61A**, 55 (1977).
10. F. Urbach, Phys. Rev. **92** (5), 1324 (1953).
11. L. S. Palatnik, P. G. Cheremskoĭ, and M. Ya. Fuks, *Pores in Films* (Énergoizdat, Moscow, 1982), p. 60.

Translated by P. Pozdeev

Technical Physics Letters, Vol. 28, No. 8, 2002, pp. 702–704. Translated from Pis'ma v Zhurnal Tekhnicheskoĭ Fiziki, Vol. 28, No. 16, 2002, pp. 85–89.
Original Russian Text Copyright © 2002 by Shuaibov, Dashchenko, Shimon, Shevera.

A Pulsed-Periodic Low-Pressure Volume Discharge in a Krypton–Chlorine Gas Mixture

A. K. Shuaibov, A. I. Dashchenko, L. L. Shimon, and I. V. Shevera
Uzhgorod National University, Uzhgorod, Ukraine
e-mail: ishev@univ.uzhgorod.ua

Received March 18, 2002

Abstract—The initiation conditions and characteristics of a volume discharge in a krypton–chlorine mixture at low pressures ($P \leq 1.0$ kPa) were studied. It is shown that a constant voltage of $U_{ch} \leq 1.0$ kV applied to a spherical anode–flat cathode system gives rise to a pulsed-periodic discharge with a pulse repetition rate of 1–50 kHz. The current–voltage characteristics of the discharge, the spectra of emission in a wavelength interval of $\Delta\lambda = 130$–350 nm, and oscillograms of the current and the total output emission intensity were studied as dependent on the partial composition and pressure of the krypton–chlorine mixture. It is shown that the discharge is a selective source of emission in the electronic-vibrational bands with $\lambda = 257$ nm [Cl_2(D'– A')], 222 nm [KrCl(B–X)], and 200 nm [Cl_2^{**}]. The volume discharge in the Kr–Cl_2 mixture can be used for the development of pulsed-periodic low-pressure excimer–halogen lamps. *© 2002 MAIK “Nauka/Interperiodica”.*

Excimer and halogen-filled lamps operating in a pulsed-periodic regime are widely used in microelectronics, high-energy chemistry, medicine, and ecology [1–3]. The operation of such radiators in a pulsed-periodic regime is based on the longitudinal, transverse, or barrier discharge powered by pulsed supply sources and is restricted to the pulse repetition rate in the range from 1 to 10^5 Hz [4–7]. The use of high-current high-voltage commutators significantly complicates the discharge initiation device and reduces the working lifetime of the lamp, which negatively influences the performance characteristics and narrows the possible applications. For this reason, it is of interest to develop simple excimer and halogen lamps in which the pulsed operation regime is provided without using traditional commutators (spark gaps, thyratrons, tacitrons, etc.). Using the development of attachment instability of plasma in electronegative gases, it is possible to employ the plasma proper as the commutator. A pulsed-periodic radiator operating in this regime with self-pumping of the working medium was implemented in a multielectrode crown discharge using He–Ar (Kr, Xe)–F_2 gas mixtures at high-pressures ($P = 150$–350 kPa). The role of an active medium in the lamp was performed by a “hot zone” with a volume of ≤ 15 cm^3 formed in the crown discharge due to the development of an attachment instability in a fluorine-containing plasma. This zone can be considered as a plasma domain (or autosoliton) [10].

Below we present the results of investigation of the characteristics of a low-pressure volume discharge formed, using an electrode system of the spherical anode–flat cathode type, in a krypton–chlorine gas mixture.

The interelectrode distance in the spherical anode–flat cathode system was 3 cm, the anode radius was 3 cm, and the diameter of massive duralumin electrodes was 7 cm. The discharge gap was power supplied from a high-voltage rectifier operating at a voltage of $U_{ch} \leq 30$ kV and an average load current of ≤ 50 mA. The electrodes were mounted in a buffer chamber with a volume of 10 dm^3. The discharge plasma parameters were determined using a registration system analogous to that described previously [6, 8, 9, 11]. We obtained the emission spectra of plasma in a wavelength interval from 130 to 350 nm, measured oscillograms of the current and of the total output emission intensity in the 200–700 nm range, and studied dependence of the intensity of KrCl and Cl_2^{**} emission bands on the pressure and composition of the working gas mixture and on the average discharge current. The pressure was varied in the range from 40 to 1000 Pa, and the discharge current, from 2 to 50 mA. Time variation of the total emission intensity was measured using a pulsed photomultiplier of the Photon type mounted on a discharge chamber window.

When a constant voltage $U_{ch} \leq 1$ kV was applied to the anode, an isolated plasma domain (or autosoliton) appeared in the interelectrode gap. This plasma formation was arranged near the anode surface and separated from the cathode by a 1- to 5-mm-wide dark space. When the pressure of the working gas mixture was decreased from 2–3 to 0.04 kPa, the average diameter of the pear-shaped plasma domain increased from 0.5 to 3.0 cm. The current and the emission intensity varied

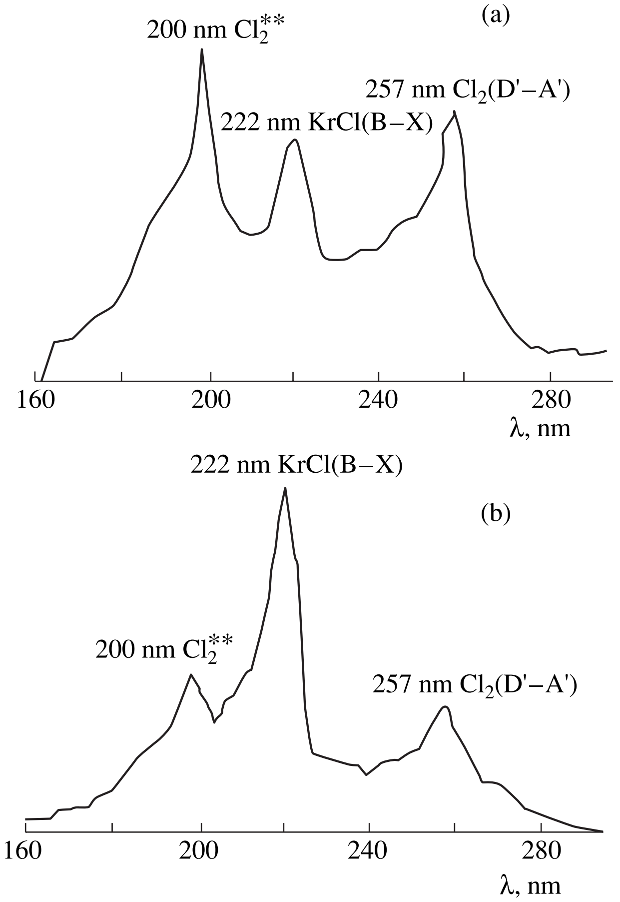

Fig. 1. The emission spectra of a volume discharge plasma formed in krypton–chlorine mixtures with $P(Kr)/P(Cl_2)$ = 80/120 (a) and 640/120 [Pa] (b) at an average discharge current of I_{ch} = 30 mA.

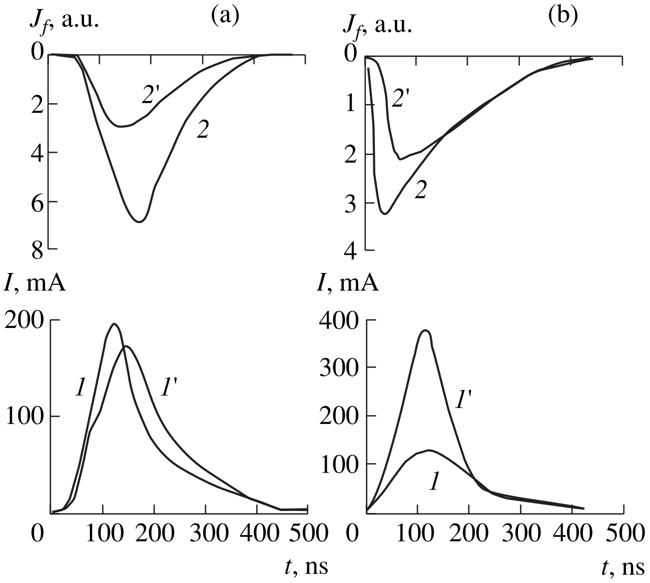

Fig. 2. Typical oscillograms of the (*1*, *1*') discharge current and (*2*, *2*') total emission intensity of a volume discharge plasma formed in krypton–chlorine mixtures with $P(Kr)/P(Cl_2)$ = 80/40 (a) and 640/120 [Pa] (b) at an average discharge current I_{ch} = 10 (*1*, *2*) and 50 mA (*1*', *2*').

in a pulsed-periodic regime: the pulse repetition frequency *f* increased from 1 to 50 kHz in response to a growth in the average discharge current. The pulse repetition rate depended weakly on the gas pressure and composition, but decreased from 50 to 3–5 kHz when the capacitance of the capacitor shunting the discharge gap was increased from 20 to 900 pF.

The discharge plasma is a selective source of emission in the wavelength interval from 180 to 270 nm (Fig. 1). The main peak in this spectrum was due to the 222 nm [KrCl(B–X)] emission band. Because of a low pressure of the working gas mixture, the emission lines of krypton chloride and chlorine molecules exhibited broadening and overlapped to form a broad common band extending from 180 to 280 nm. At a low partial pressure of krypton in the mixture, the intensities of KrCl(B–X) and Cl_2^{**} bands are comparable (Fig. 1a). As the content of krypton in the mixture increases, the 222 nm [KrCl(B–X)] band becomes predominant (Fig. 1b). Optimum gas mixture compositions, ensuring the maximum total intensity of emission from chlorine and krypton chloride molecules, corresponded to the partial pressures of components $P(Kr)/P(Cl_2)$ = (500–650)/(120–200) [Pa].

Figure 2 illustrates typical dynamics of the current and the total emission intensity for the discharge in various krypton–chlorine mixtures. A low-pressure discharge (Fig. 2a) exhibited a maximum volume of the plasma and produced maximum intensity of the total emission at a small average discharge current ($I_{ch} \leq$ 10 mA). In this regime, the emission pulses began to form already on the leading front of the pumping current pulse and reached peak intensity at the maximum or during the nearest afterglow stage of the discharge current. An increase in the partial pressure of krypton in the mixture led to a shift of the emission peak toward the trailing front of the pumping pulse (Fig. 2b). In this case, a difference in shape of the emission pulses observed for the average discharge currents of 10 and 50 mA was not as pronounced.

Thus, the results of our investigation showed that a spherical anode–flat cathode system powered from a dc high-voltage source provides for the obtaining of a pulsed-periodic volume discharge in a $Kr–Cl_2$ gas mixture. The discharge plasma serves as a selective UV–VIS radiator operating on the electron transitions of KrCl and Cl_2^{**} molecules. The main factor determining the pulsed-periodic discharge operation is the attachment instability of the chlorine-containing plasma. This discharge can be used for the development of simple low-pressure excimer and halogen lamps with a radiation pulse duration of $\tau \leq 400$ ns.

REFERENCES

1. H. Sigimura, O. Takai, and N. Nakagiri, J. Electroanal. Chem. **437**, 230 (1999).

2. I. W. Boyd and I. Y. Zhang, Mater. Res. Soc. Symp. Proc. **617**, J. 4.4.1 (2000).
3. G. S. Polunin, V. V. Kourenkov, and E. G. Polunina, J. Refract. Surg. **14** (2), 230 (1998).
4. V. A. Vizir', V. S. Skakun, G. V. Smorudov, and É. A. Sosnin, Kvantovaya Élektron. (Moscow) **22** (5), 519 (1995).
5. V. M. Borisov, V. A. Vodchits, A. V. El'tsov, and O. B. Khristoforov, Kvantovaya Élektron. (Moscow) **25** (4), 308 (1998).
6. A. K. Shuaibov, Pis'ma Zh. Tekh. Fiz. **26** (9), 1 (2000) [Tech. Phys. Lett. **26**, 357 (2000)].
7. A. K. Shuaibov, L. L. Shimon, I. V. Shevera, and A. J. Minya, J. Phys. Stud. **3** (2), 157 (1999).
8. A. K. Shuaibov, L. L. Shimon, A. I. Minya, and A. I. Dashchenko, Prib. Tekh. Éksp., No. 6, 128 (1997).
9. A. K. Shuaibov, L. L. Shimon, and A. I. Minya, J. Phys. Stud. **4** (3), 291 (2000).
10. N. L. Aleksandrov and A. P. Napartovich, Usp. Fiz. Nauk **163** (3), 1 (1993) [Phys. Usp. **36**, 107 (1993)].
11. A. K. Shuaibov, A. I. Dashchenko, and I. V. Shevera, Kvantovaya Élektron. (Moscow) **31** (6), 547 (2001).

Translated by P. Pozdeev

Technical Physics Letters, Vol. 28, No. 8, 2002, pp. 705–706. Translated from Pis'ma v Zhurnal Tekhnicheskoĭ Fiziki, Vol. 28, No. 16, 2002, pp. 90–94.
Original Russian Text Copyright © 2002 by Leksowskij, Borovikov, Bozorov, Abdumanonov, Sinani, Piletski.

The Zone of Damage for High-Modulus Materials in Explosion-Loaded Granite

A. M. Leksowskij, V. A. Borovikov, N. S. Bozorov, A. A. Abdumanonov, A. B. Sinani, and S. A. Piletski
Ioffe Physicotechnical Institute, Russian Academy of Sciences, St. Petersburg, 194021 Russia
e-mail: Albert.Leksowskij@pop.ioffe.rssi.ru

Received March 25, 2002

Abstract—It is established that blast loading of a rock material of granite type leads to the formation, in addition to the well-known cracking zone, of a more extended zone featuring a microdamage of high-modulus crystal inclusions in the rock. A method of determining the size of this damage zone is proposed. It is shown that the radius of the zone of microdamage of high-modulus crystals can be significantly reduced by means of controlled variation of the explosive density and the blast-loading regime. *© 2002 MAIK “Nauka/Interperiodica”.*

The problem of preserving natural precious crystals in the course of a blast disintegration of rocks is still very important [1]. Previously [2], we used luminescent microscopy data for granite to demonstrate the possibility of revealing *post facto* the blast-induced microdamage (microdiscontinuities) in high-modulus minerals. It was found that a blast, while breaking both feld spar and quartz grains over a distance of 20–30R_{03} (where R_{03} is the charge or blasthole range), predominantly breaks quartz grains at large distances ($\geq 40R_{03}$). The crystals of mica in our experiments remained intact. Thus, the experimental data indicated that high-modulus crystals are disintegrated first—a fact to which researchers did not pay attention before. From the standpoint of the physics of strength of composite materials, this is a quite natural result. Indeed, under joint straining conditions, high-modulus crystals are the first to reach a critical stress level under the conditions of equal general straining of components in heterogeneous rock.

It was therefore of interest to use model samples and a model situation in order to check the validity of this concept under dynamic loading conditions. We prepared three groups of model composite samples using poly(methyl methacrylate) (PMMA) disks with a diameter of 50 mm and a height of 10 mm. Each disk had a 1.5-mm through channel at the center, which was filled with a cured epoxy resin. In one group of samples, the channel also contained a high-modulus (E = 400 GPa) high-strength boron fiber with a diameter of 100 μm. In the other group, the channel contained a high-strength glass fiber of the same diameter but with a lower elastic modulus (E = 70–90 GPa). In order to apply a short-time axial tensile strain, all samples were loaded by impact of a duralumin cylinder via a duralumin buffer with the aid of a light-gas gun [3]. The impact velocity was varied from 100 to 220 m/s, the loading pulse duration was 2–3 μs, and the pulse length was 6 mm.

The results of our experiments showed that the dynamic shear strength of the homogeneous PMMA samples and those with an epoxy-filled channel amounts to 160–180 MPa. The high-modulus boron fiber exhibited fracture already at an impact velocity of 109–120 m/s, in which case the dynamic load of the organic glass was on the level of 80–90 MPa and the PMMA body remained intact (exhibiting no traditional cleavage). Examination of the fracture surface of a broken boron fiber in a scanning electron microscope showed that the fracture was initiated from inside, beginning at the boron–tungsten interface. Thus, the fracture proceeded as in a fiber tensile loaded at the ends. Hence, the fiber breakage was not caused by a crack nucleated at the PMMA–epoxy interface. In the samples with glass fibers, the fracture was observed at a significantly higher dynamic load of 120–130 MPa. This corresponds to a higher dynamic straining of the system as compared to the case with the boron fiber, albeit still lower than in the case of a homogeneous PMMA sample.

Thus, direct experiment showed that a heterogeneous material obeys the principle of joint straining not only in a static loading regime, which is a well-known fact, but under dynamic loading conditions as well. For this reason, high-modulus crystals (inclusions) even at a large distance from the center of explosion can be damaged (as a result of microcracking) even at an insignificant level of stresses in the crystal-containing rock.

Now let us consider dimensions of the zone of possible microdamage for high-modulus crystals. We studied samples cut upon explosion [2] from a granite block at various distances from the blasthole center. By weighing the rock fragments on an electronic balance (ER-180A) to within 10^{-4} g in the initial (vacuum dry)

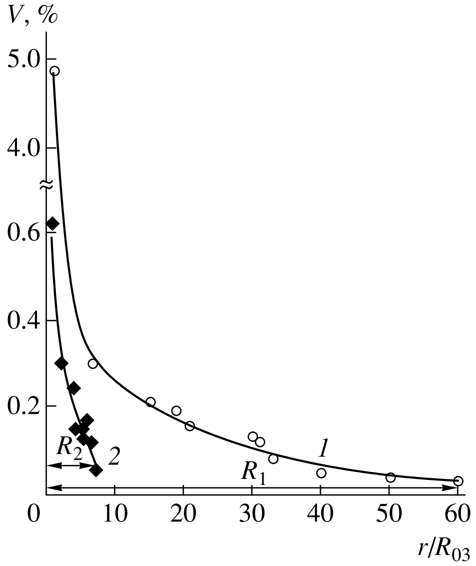

Fig. 1. Plots of the total volume V of microdiscontinuities in high-modulus minerals of granite cut versus distance from the blasthole center for (*1*) high-density (~1.6 g/cm^3) and (*2*) low-density (0.5 g/cm^3) explosives.

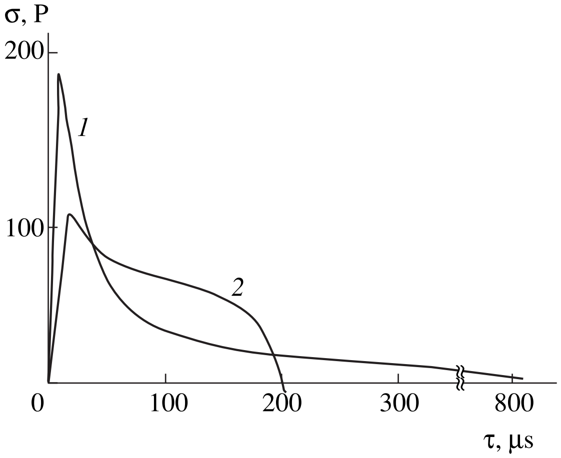

Fig. 2. Schematic profiles of the stress waves produced by (*1*) high-density (~1.6 g/cm^3) and (*2*) low-density (0.5 g/cm^3) explosives.

state and upon impregnation with a “light” wetting solvent, we approximately determined the “true” volume of microcracks and estimated the blast-induced relative total damage V [%] (Fig. 1). As can be seen from these data (curve *1*), the high-modulus components of the granite samples upon explosion of the PETN charge with a density of ~1.6 g/cm^3 exhibit damage even at a distance as large as (40–60)R_{03} from the blasthole center.

At first glance, the level of damage may seem insignificant (at least in comparison to that in the near zone). Assuming the opening of microcracks to be 0.1–1 μm, a sample with a cross-sectional size equal to that of the fragment selected may contain from a few to 100 or more “empty” plates depending on the distance to the blasthole center. The level of damage at a distance of $r \geq 60R_{03}$, which was acquired in the preceding stage of granite recovery in a commercial quarry, was considered as initial. It should be noted that the volume damage profile of a heterogeneous material with a constant composition can be considered as characterizing the distribution of true local strain in a block of the rock upon blasting. The broken high-modulus crystals serve as detectors or indicators of the local strain level.

Using the results of these measurements, we can estimate the radius of a potential damage zone for high-modulus quartz crystals in granite at $r \leq 60R_{03}$ upon explosion of the PETN charge with a density of ~1.6 g/cm^3. This range, which can be considered as a fracture precursor zone, is several times greater than the blast-induced cracking zone. This estimate can be important for the blast recovery of stone blocks.

Upon passage to a charge of lower density (~0.5 g/cm^3), the wave profile is characterized by a smaller amplitude and a more uniform energy distribution in time [1] (Fig. 2, curve *2*). A comparison shows (cf. curves *1* and 2 in Fig. 1) that the radius of the zone of microdamage in the case of a lower charge density is several times smaller as compared to the estimate obtained above for a high charge density.

Thus, using the above approach, we determined an important practical characteristic—the radius of the zone of microdamage (i.e., a zone where the damage in the form of microcracks will most probably appear) in high-modulus crystals of precious minerals, which are usually the main aim of such blast work. A comparison of various blast technologies using traditional high-density (~1.6 g/cm^3) and low-density charges (0.5 g/cm^3) shows that the microdamage zone radius in the latter case is 5–6 times smaller than that in the former.

Based on the above results, we believe that the proposed method of damage zone estimation can offer an effective tool for the development of less damaging blast technologies.

REFERENCES

1. V. A. Borovikov, V. N. Zaostrovtsev, A. N. Shmyrko, *et al.*, in *Proceedings of the VI International Scientific Conference “Ecology and Development of the North-West Region of Russia,” 2001*, p. 73.
2. A. M. Leksowskij, V. A. Borovikov, N. S. Bozorov, *et al.*, Pis’ma Zh. Tekh. Fiz. **22** (3), 6 (1996) [Tech. Phys. Lett. **22**, 93 (1996)].
3. N. A. Zlatin, S. M. Mochalov, G. S. Pugachev, *et al.*, Zh. Tekh. Fiz. **45** (3), 681 (1975) [Sov. Phys. Tech. Phys. **20**, 428 (1975)].

Translated by P. Pozdeev